UNIVERSITY OF RIJEKA

FACULTY OF PHYSICS

Petar Pervan

ELECTRIC FIELD MODIFICATIONS OF METAL-DIELECTRIC MULTILAYER SYSTEMS FOR FABRICATION OF OPTICAL FILTER MICROARRAY

DOCTORAL THESIS

Supervisor: dr. sc. Vesna Janicki

Co-supervisor: doc. dr. sc. Robert Peter

Rijeka, 2023.

Mentor rada: dr. sc. Vesna Janicki, Institut Ruđer Bošković

Komentor rada: doc. dr. sc. Robert Peter, Sveučilište u Rijeci

Doktorski rad obranjen je dana _____ u/na

_____, pred povjerenstvom u sastavu:

1. _____

2. _____

3. _____

4. _____

5. _____

Acknowledgements

A lot of people should be credited for this work besides me.

Firstly, a huge thank you goes to my supervisor, dr. sc. Vesna Janicki. She poured a lot of time and patience in making this thesis come true, guided me through my first steps in science, encouraged me to do the experimental work, and was always available when I needed advice.

I would also like to thank all of my colleagues for transferring their knowledge, and for guidance and comments which helped immensely.

A thank you goes to my parents for all the support they gave unconditionally throughout my life, and to my girlfriend Ines for having the understanding while I studied and/or worked long hours not just on workdays, but often through weekends.

Abstract

Metal-dielectric multilayer systems are used for sensors, filters and absorbers. Fabrication of micro/nanostructures in these systems is complex, demanding and involves many fabrication steps. Glass poling (GP) and electric field assisted dissolution (EFAD) processes have great potential for micro/nano structuring of metal-dielectric systems. GP and EFAD are used to modify the compositional profile of samples by application of voltage inducing drift of metallic species in the direction of the applied field.

The aim of this work was to make micro-structured metal-dielectric multilayer system with desired optical performance demonstrating appropriateness of EFAD for micro-structuring. This aim was achieved by dividing the research into partial goals: i) relating modifications of the substrates refractive index with the changes in its composition upon GP. Different types of glasses were studied in quest for the most appropriate and simple system. ii) study of simultaneous EFAD of bimetal systems as the main process for obtaining micro array filter. Different combinations of metals were tested to choose the one best controlled by the treatment. iii) depositing, micro-structuring and analysis of the micro-structured filter.

Significant scientific contributions were made: a) understanding how the poled glass refractive index profile correlates with the redistribution of alkali ions and other structural changes in glass, b) quantitative determination of the specific contribution of different alkali ion species to the refractive index of poled glass, determination and understanding of the dynamics of c) GP with multiple ion species and d) simultaneous EFAD of two metals embedded in dielectric multilayers systems.

Extended abstract in Croatian language

Metalo-dielektrični višeslojni sustavi važni su zbog mogućnosti ovih struktura da se koriste kao senzori, filteri i apsorberi. Izrada mikro/nanostruktura je složena, zahtjevna i uključuje više koraka u procesu izrade. Procesi električnog polariziranja stakla (eng. *glass poling*, GP) i razlaganje uz pomoć električnog polja (eng. *electric field assisted dissolution*, EFAD) imaju potencijal za korištenje u mikro/nano strukturiranju metalo-dielektričnih sustava. Da bi se to postiglo potrebno je kontrolirati dinamiku GP-a i EFAD-a i svojstva materijala u višeslojnim sustavima tijekom GP-a i EFAD-a. Cilj ovog rada je postići spomenutu kontrolu GP-a i EFAD-a i izraditi mikrostrukturirani metalo-dielektrični višeslojni sustav sa željenim optičkim performansama kao demonstrator prikladnosti EFAD-a kao metode za mikrostrukturiranje ovih sustava.

Cilj ovog rada je bio izraditi mikrostrukturirani metalo-dielektrični višeslojni sustav sa željenim optičkim svojstvima i tako pokazati prikladnost EFAD-a za mikrostrukturiranje. Ovaj je cilj bio postignut podjelom istraživanja na djelomične ciljeve: i) povezivanje promjena u indeksu loma podloge s promjenama njegova sastava nakon GP-a. Budući da će se kao podloga za filter koristiti staklo, proučene su promjene u različitim vrstama stakla kako bi se izabrao najučinkovitiji i najjednostavniji sustav. ii) upoznati simultani EFAD-a sustava koji sadrži dva različita metala, budući da je upravo taj proces ključan za izradu mikrofiltera. Testirane su različite kombinacije metala kako bi se izabrala ona koju je najlakše kontrolirati u procesu. iii) depozicija, mikrostrukturiranje i analiza mikrostrukturiranog filtera.

Tanki slojevi višeslojnih sustava su izrađeni metodom naparavanja pomoću elektronskog snopa. Uzorci su tretirani GP-om u vakuumu i na zraku, EFAD-om i zagrijavanjem. Profili indeksa loma tretiranih uzoraka su dobiveni optičkom karakterizacijom na osnovu elipsometrijskih mjerenja. Masena spektroskopija sekundarnih iona je korištena za određivanje dubinskog profila koncentracije alkala i metala. Dubinski profil koncentracije iona stakla je modelirana numeričkim simulacijama koristeći diferencijalne jednadžbe koje opisuju drift i difuziju struja i njihov razvoj tokom vremena. Površinski profil dobivene mikrostrukture je analiziran profilometrom.

Ostvaren je znatan znanstveni doprinos području kao rezultat istraživanja. Razumjelo se kako je profil indeksa loma stakla koreliran s preraspodjelom iona alkala i drugim strukturnim promjenama u staklu. Kvantitativno je određen specifični doprinos različitih vrsta alkala indeksu loma stakla. Shvaćena je dinamika GP-a s više vrsta iona i simultanog

EFAD-a dva metala uronjenih u dielektrični višeslojni sustav. Shvaćeni su uzroci razlika u optičkom odzivu izrađenog i dizajniranog mikrostrukturiranog filtera.

Keywords: glass poling, thermal poling, refractive index profile, ionic mobility in glass, ellipsometry, secondary ion mass spectroscopy, numerical simulation, metal island films, electric field assisted dissolution, multilayers, ion exchange, localized surface plasmon resonance, thin films, metal-dielectric multilayer systems, optical filters, optical filter microarrays, microstructuring

Ključne riječi: električno polariziranje stakla, termičko električno polariziranje stakla, profil indeksa loma, mobilnost iona u staklu, elipsometrija, masena spektroskopija sekundarnih iona, numeričke simulacije, filmovi metalnih otočića, razlaganje pomoću električnog polja, ionska izmjena, rezonancija lokaliziranih površinskih plazmona, tanki filmovi, metalno-dielektrični višeslojni sistemi, optički filtri, mikropolja optičkih filtara, mikrostrukturiranje

Table of Contents

1.   INTRODUCTION

The presented research concerns the modification of linear optical properties of metal nanocomposite systems (MNCS) in a wide range by changing its composition in a versatile and simple way, with the final goal to apply it for fabrication of microarray filter. This includes tailoring reflection, transmission and absorption. For this purpose, interference on thin dielectric films was combined with absorption in systems metal island films. The applied approach enables production of systems with optical properties required for application in optical and optoelectronic devices. Optical properties of the obtained micro arrays containing optical micro filters is also included in the research, keeping in mind the applicability of the used method for fabrication of micro sized devices that are demanded by ever-developing industry.

Metal-dielectric multilayer systems (MD MLS) are of great importance in producing metal island film (MIF) sensors [1, 2], coloured optical filters [3] and absorbers [4]. Some other interesting applications of MD MLS are super-absorbers and colour filters [5], broadband black perfect absorbers [6] broadband absorption to reconfigurable reflection coatings [7], angle independent structural colour [8] or Salisbury screens [9].

MIFs are very important in optics because they do not behave optically similar to the corresponding bulk material. In this case, metal electrons are confined to the nanoparticles forming the film and show a strong resonant behaviour in the optical range, i.e., the localized surface plasmon resonance (LSPR) [10]. They are used in present-day optics and optoelectronics in many industrial applications that make use of their optical, electronic, and mechanical properties. Classic examples of optical systems with functionality based on the LSPR are the red and yellow colours of medieval church windows.

Due to the great interest in scaling optical devices to micro and nano dimensions, there is a quest for methods allowing fabrication of different devices placed together in micro and nano arrays. In this way, sensors for different species or multispectral filters, to mention just some possibilities are densely packed on small surface. Thus micro and nano arrays may provide high spatial resolution colour filtering and spectral imaging with extremely compact device architectures [11].

Photolithography [12] and electron/ion beam lithography [11] are micro and nano structuring techniques applicable to MD MLS, to name just a few. These techniques involve several fabrication steps and may be time demanding, resulting in high production cost of the

final micro and nano structures. Equipment for electron/ion beam lithography is expensive itself.

Future development will be focused on the improvement of MD MLS optical properties for chemical and biological sensors and micro and nano structuring for information and telecommunication industry (screens, nanoantennas, optical chips). In addition, it will involve a simplification of the production process and lowering the products price in order to bring nanotechnology closer to the everyday use. In this framework, a promising research line focuses on the formation of nanocomposite glasses and structures via glass poling (GP) and electric filed assisted dissolution (EFAD), but also on obtaining a deeper understanding of the connection between GP/EFAD process parameters and structural and optical properties of the material. The dependence of the obtained optical properties on the structural properties is still understood only at the phenomenological level and requires further research.

GP and EFAD are techniques used to modify the compositional profile of samples by application of a d.c. voltage that induces the drift of different metallic species in the direction of the applied field [13]. Sample modification can be restricted to selected regions of the sample by using structured electrodes for localized application of electric field. In this way, micro and nano-structures can be obtained if patterned electrodes are used.

GP and EFAD advantages, compared to the standard techniques ways of MD MLS and nanocomposite layers fabrication, may include simple and inexpensive equipment, relatively short process time, no environmental issues and the fact that they enable 2D and 3D micro and nano structuring simultaneously with the composition change. Micro and nano structuring of MD MLS with GP and EFAD could have a great impact on the industry by simplifying the production process and lowering the price of optical and optoelectronic devices. Therefore, it is necessary to investigate GP and EFAD induced changes of optical properties in such systems in order to be able to take them into account and readily compensate in the design of MD MLS. Optical filters allowing broader range of optical performance may also require the use of two metals and two dielectric materials in design.

Apart from structuring of glass surfaces with GP and EFAD where lot of work was already done, these techniques are demonstrated as versatile techniques for fabrication of micro/nano structures consisting of MIF or even compact metal layers on different substrates. GP enables obtaining MIF consisting micro/nano structures on glass surface by application of patterned electrode to the glass followed by annealing in hydrogen in the case of metal nanocomposite glass [14] or followed by coating it with metal salt solution and annealing in

the case of soda-lime glass [15]. Microstructures consisting of compact metal areas can be obtained employing GP followed by EFAD, either on glass [16] or silicon substrate [17]. However, none of these methods is demonstrated to be applicable for MD MLS.

EFAD application for fabrication of simple micro-structured MD MLS containing several MIFs, resulting in 3D optical grating, was demonstrated a decade ago [18]. Since then some advance was made to understand dynamics of MIF dissolution in MD MLS [19] and the influence of different dielectric materials layers to the metal ion distribution in the system [20]. These issues have great importance for optical performance of such systems upon EFAD and therefore for obtaining micro/nano structured MD MLS. Namely, both GP and EFAD doping with metal ions change films thickness and refractive index profile of the system. These changes may influence the optical performance, i. e. spoil the expected optical properties of MD MLS.

Significant progress has been made over the recent years in numerical modelling of GP and EFAD [21]. However, more complex cases involving EFAD of two metals, or metals embedded in dielectric multilayer systems, as well as the effects of EFAD and GP dynamics on refractive index profile $n(d)$ of glass are still not well understood. Structural and optical characterization of MD MLS systems upon GP and EFAD with detailed numerical simulations might enable new insights into properties of such systems in order to demonstrate successful application of these processes for fabrication of micro and nano structured MD MLS.

In this sense, research hypothesis of this study was that dynamics of GP and EFAD as well as materials properties changed by these processes can be controlled well enough to enable successful fabrication of micro-structured MD MLS consisting of optical micro filters of clearly distinguishable colours in reflection or transmission, defined by the design of the system (desired optical performance). It would be verified in this way that EFAD is applicable as a one-step technique for fabrication of elaborate micro or nano structured MD MLS.

To accomplish this, the research was divided into smaller steps. As GP and EFAD change refractive index of glass used as filter substrate, the first step was to relate modifications of the substrates refractive index with the changes in its composition upon GP. Also, different types of glasses were studied in quest for the most appropriate and simple system. GP serial of samples was prepared and studied in this step. The second step was related to the study of simultaneous EFAD of bimetal dielectric systems as it was the main process for obtaining micro array filter and published literature related to this complex

process is poor (one paper only). In the same step different combinations of metals were tested in simultaneous EFAD serial to choose the one that is the best controlled by the treatment. Finally, based on results of the previous steps and choice of the suitable design, the filter was deposited, micro-structured by EFAD and analyzed.

Thin films were prepared by electron beam physical vapour deposition. Samples were treated by GP in air and vacuum, EFAD and annealing. Variable angle spectroscopic ellipsometry provided refractive index profiles of the treated samples. Secondary ion mass spectrometry provided the information about depth profile of alkali and ion concentrations. Ion concentration depth profile of glass was modelled by numerical resolution of the differential equations describing the drift and diffusion currents and their time evolution. Broader theoretical knowledge of the poling process was acquired by optimizing the properties of mobile ions contained in glass iteratively while running simulations. Surface profile of the obtained micro-structure was examined by profilometry.

As result of the research, significant scientific contributions this area were made: a) it was understood how the refractive index profile of poled glass correlates with the redistribution of alkali ions and other structural changes in glass, b) it was quantitatively determined the specific contribution of different alkali ion species to the refractive index of poled glass, it was determined and understood the dynamics of c) GP with multiple ion species and of d) simultaneous EFAD of two materials MIFs embedded in dielectric multilayers systems. These results are published in peer review journals. (* In the time of submitting the thesis for evaluation the second paper is not yet published, it is under review only.)

The design of the filter and simulations of influence of compositional modifications to its performance were made by V. Janicki (Ruđer Bošković Institute, Zagreb). SIMS measurements were done by R. Peter (University in Rijeka, Rijeka).

The dissertation is structured as follows: in the next chapter will be briefly explained modes of thin films growth, optical properties of materials, how optical parameters of thin film system are determined from ellipsometric measurements. Here are also given characteristics of the used materials, explained GP and EFAD an additional characterization techniques shortly presented. The third chapter describes preparation of the samples, presents filter design, how measurements were done and how data were analysed and numerical simulations performed. The fourth chapter gives results and discussion separately for each serial of the samples. The conclusions can be found in the last chapter.

2.   THEORY, MATERIALS AND METHODS

In this chapter theoretical background of thin film growth and optical properties of materials and multilayer systems will be presented. Measurements of optical properties using ellipsometry will be explained, followed by optical characterization section, i.e. how samples optical parameters (such as layers thickness and refractive index) is obtained from the measured data. Basics of thin film systems design will be given as well. Materials used in the experimental segment of the research will be introduced. GP and EFAD techniques and how they modify optical systems will be explained. Finally, additional techniques used in characterization will be presented.

2.1. Growth of materials in thin films and deposition techniques

Thin and ultrathin films are formed on a substrate surface by condensation of atoms, molecules or ionic fragments through physical process or chemical reaction. Thin films are several nm to several μm thick, while ultrathin films are one atomic layer to one hundred atomic layers (several nm) thick. Investigations how process parameters (temperature, pressure and gas flows), affect obtained thin film structures and their properties have been in progress since 1938 [22]. There is a significant difference between performance of models based on ideal and real structure of the films [23]. Focus will be on growth of dielectric and metal coatings.

There is a number of deposition techniques for thin film fabrication. Those techniques that are using vacuum can be divided into three main categories: evaporation methods, discharge methods, and chemical deposition processes from gas phase. Electron beam deposition will be discussed in more detail, as it was used in this work.

Growth of materials with crystal lattice significantly different from the substrates can be categorized in three basic types, depending on the binding energy among adatoms and the binding energy among adatoms and substrate [24] (Figure 2. *1*):

· Frank-van der Merwe growth (layer-by-layer)
· Stranski-Krastanow growth (joint islands or layer-plus-island)
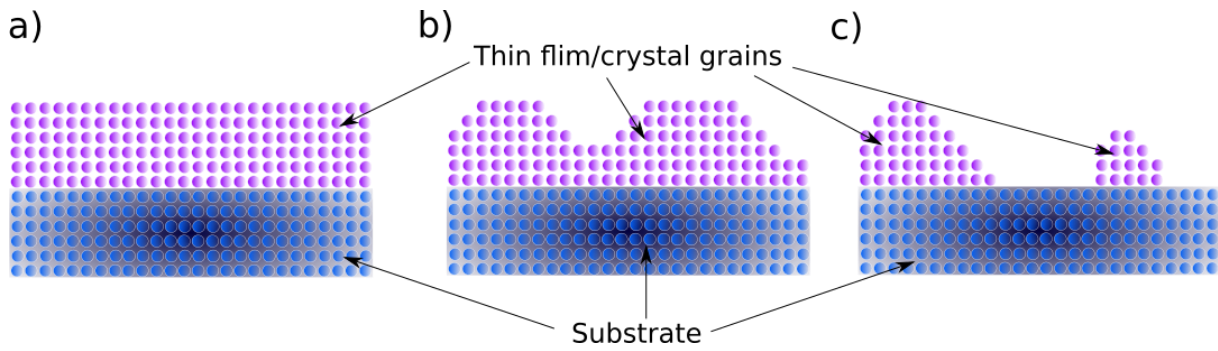· Volmer-Weber growth (isolated islands)

Figure 2. 1. Types of thin films growth. a) Frank-van dMerwe b) Stranski–Krastanov and c) Volmer–Weber growth.

2.1.1.   Dielectrics

Structure zone models (Figure 2. *2*) show the real structure of dielectric thin films that may be columnar, polycrystalline or contain defects and pores [25]. Optical properties and real structure containing impurities are related by effective medium approximations (EMA) [26]. Refractive index may change with film thickness as the films structure changes.
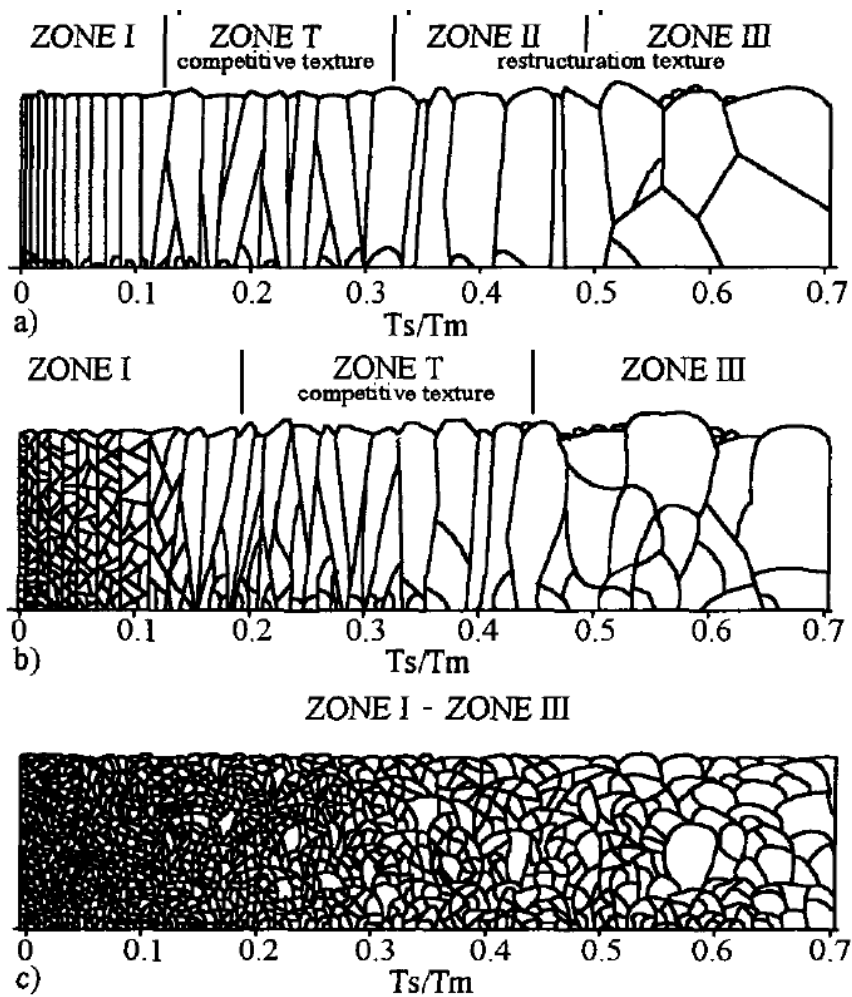

Figure 2. 2. The real structure zone models at low a), medium b) and high c) impurity content

Thin films contain up to 5 orders of magnitude higher number of defects than bulk materials. Absorption in thin film is to a large degree caused by defects in the film (water, oxygen, hydrocarbons,...) [23].

Real structures also cause scattering losses originating from grains, pores, defects and interface roughness [27].

2.1.2.   Metals

Growth of metal films on dielectric substrates starts with Volmer–Weber (isolated islands) growth (Figure 2. *3*). The size of island is increasing as more material is deposited. At percolation threshold, when critical quantity of material is deposited, islands join and the film becomes continuous. Further material deposition leads to formation of compact film.
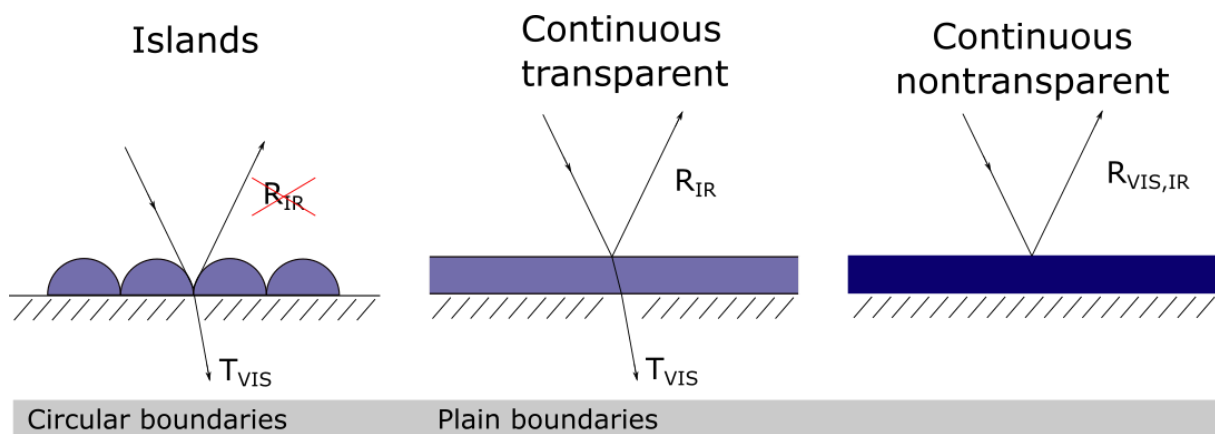

Figure 2. 3 Growth of a metal film, starting from islands to continuous transparent to nontransparent films.

Incident light can excite surface plasmons excitation in metal islands and very different optical response than in the case of compact films, as it will be discussed later.

2.1.3.   Thin film deposition techniques

Thin film properties depend on the materials used and film thickness, but also on deposition technique and conditions. There are a number of deposition techniques using vacuum. In evaporation deposition methods material is condensed on substrate from vapour, in discharge methods clusters of material are impinging to substrate and in chemical deposition processes from gas phase. Electron beam evaporation method (EBE) is widely used in both, research and industry, due to high deposition rates and broad range of applicable materials, although other techniques may provide more dense layers with very precisely controlled film thickness. Typical physical vapour deposition rates are 10–100˚A (1–10 nanometers) per second [28].

Evaporation deposition methods transfer kinetic energy to atoms in solid phase that is sufficient for atoms to break the bond and sublimate into gas phase that condenses on a substrate and creates a thin film.

Quartz crystal microbalances (QCMs) are the most commonly used devices for monitoring deposition rate. Piezo-electric quartz crystal is connected to a pair of electrodes, a monitor for rate and thickness measurement and a controller [29]. As AC voltage is applied, the quartz crystal starts to oscillate due to the piezo-electric effect. The oscillation frequency changes with deposition of the material, and this correlates to the amount of added mass.

In EBE material is placed in a water-cooled crucible where it melts in its own environment and there is practically no chance of unwanted reaction with the crucible wall (Figure 2. *4*) [30]. A high voltage in the range between 10 - 20 kV accelerates the electrons to the anode - crucible.
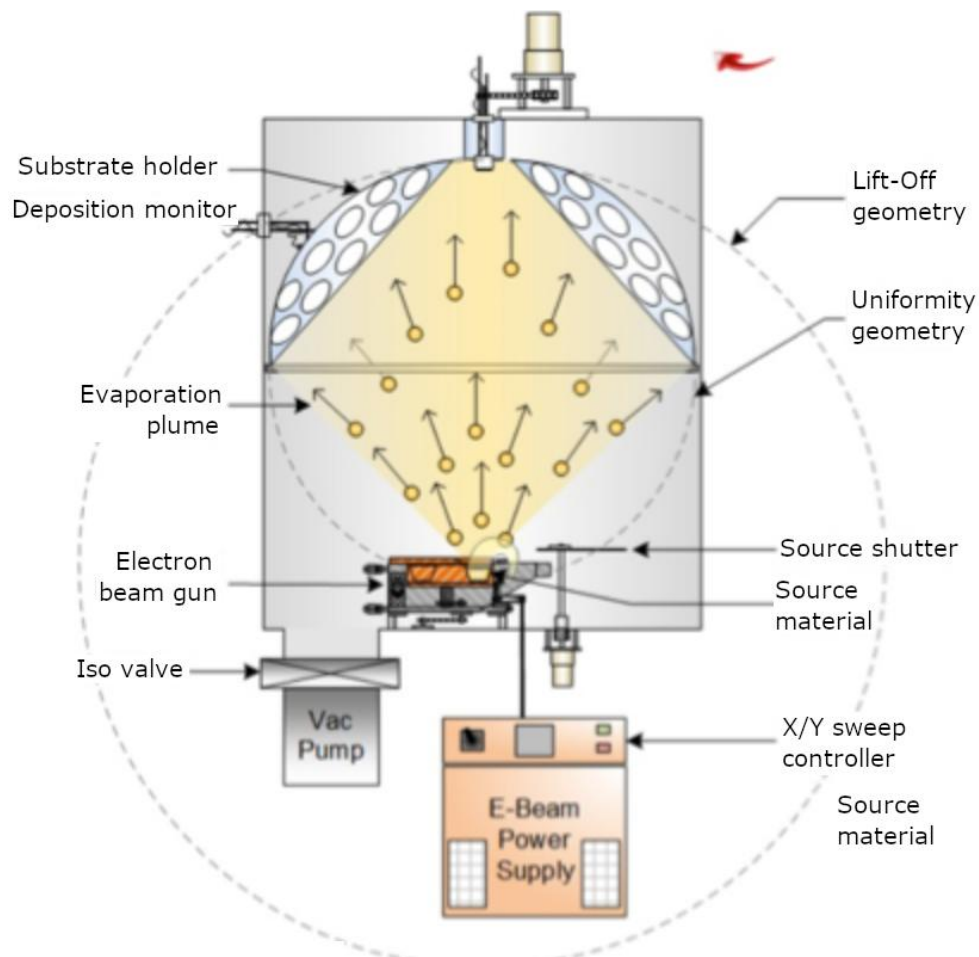

Figure 2. 4. Schematic presentation of electron beam evaporation.

2.2. Materials optical properties

2.2.1.   Optical constants and dispersion models

Light can be described as an electromagnetic plane wave, with an equation [31]:

Eq. 2. 1 $$\vec{E}(\vec{r},t) = \vec{E}_0 exp\ (i\frac{\omega\tilde{n}}{c}\vec{r})exp\ (-i\omega t + \phi)$$

which is a solution of the electric field wave equation where ω is the angular frequency of the wave, $\vec{r}$ is the position vector, t is time, i is the imaginary unit, $\tilde{n}$ is the complex refractive index of propagation medium, ϕ is constant phase angle, $\vec{E}_0$ is a complex vector constant specifying the amplitude and polarization state of the wave, and c is the speed of light (*Figure 2.5*) [32].
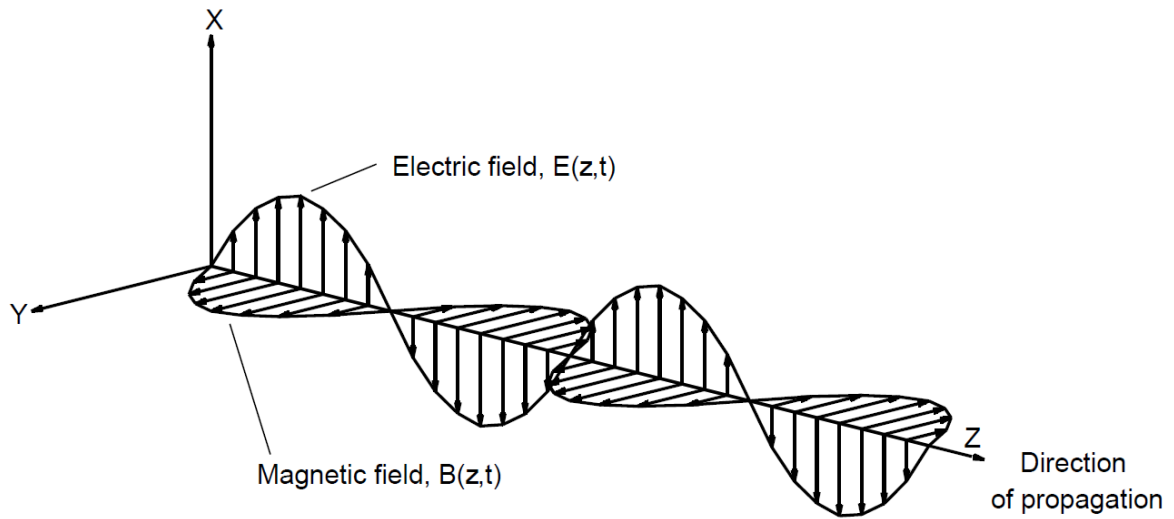

Figure 2.5. Schematic of electromagnetic plane wave propagating in a medium with no absorption.

The complex refractive index, $\tilde{n}$, appears in the expression for the plane wave. $\tilde{n} = n + ik$, where n is the real part of complex refractive index (or simply refractive index), and k is the extinction coefficient. If the imaginary part of the complex refractive index (extinction coefficient), is non-zero, the amplitude of the wave will decay exponentially as it propagates, according to the following expression:

Eq. 2. 2 $$|E(z)| \propto exp\ (-\frac{2\pi kz}{\lambda})$$

where z is the length of propagation in length units and $\lambda = \frac{2\pi c}{\omega}$ is wavelength. The wave will decay to $1/e$ of the original amplitude after propagating a distance D_p. D_p is penetration depth, given by:

Eq. 2. 3
$$D_p = \frac{\lambda}{2\pi k}$$

Magnetic component of electromagnetic wave $\vec{B}(\vec{r}, t)$ can be defined by an equation analogous to the Eq. 2. *1*, with the electric and magnetic field perpendicular to each other and to the direction of propagation. Due to this relationship between the fields, only the electric field and the direction of propagation are required to completely define a plane wave.

Optical constants / dispersion models

Optical constants are material parameters that describe the interaction of light and matter at a certain frequency of incidence wave [33]. Description of this interaction can be obtained by relating properties of propagation of light to some property of material. The polarization field $\vec{P}$ is induced in the material by external electric field $\vec{E}$ at some point. $\vec{P}$ is proportional to the external field:

Eq. 2. 4
$$\vec{P} = \tilde{\chi}_e \epsilon_0 \vec{E}$$

where $\tilde{\chi}_e$ is the electric susceptibility of the material and ϵ_0 is free space permitivitty. The displacement field $\vec{D}$, equals the external electric field plus the polarization field:

Eq. 2. 5
$$\vec{D} = (1 + \tilde{\chi}_e)\epsilon_0 \vec{E}$$

The displacement and electric fields are correlated by:

Eq. 2. 6
$$\vec{D} = \tilde{\varepsilon}\vec{E}$$

Eq. 2. 7
$$\tilde{\varepsilon} \equiv (1 + \tilde{\chi}_e)\epsilon_0 = \tilde{\varepsilon}_r \epsilon_0$$

where the constant of proportionality $\tilde{\varepsilon} = \varepsilon_1 + i\varepsilon_2$ is the complex dielectric function of the material, and $\tilde{\varepsilon}_r$ is permittivity of the material. Dielectric function is a complex quantity that quantifies the degree to which the material may be polarized by an applied electric field. Imaginary part of the dielectric function, ε_2, is proportional to the power of the applied external field absorbed per unit time and unit volume at a point in the material.

If the response of the material to the applied field is not isotropic (which occurs in many crystals of non-cubic symmetry), then the complex scalar dielectric function in equation 2.7 is replaced with a 3×3 tensor dielectric function. Another representation of the optical

properties of the material is based on the effect the material has on an electromagnetic wave propagating through the material. The right side of Eq. 2. *1* contains complex index of refraction:

Eq. 2. 8 $\qquad \tilde{n} = n + ik$

It governs the change in amplitude and phase of the propagating wave. The complex index of refraction and the complex dielectric function of a material are related by:

Eq. 2. 9 $\qquad \tilde{n} = \sqrt{\tilde{\varepsilon}}$

with $\varepsilon_1 = n^2 - k^2$ and $\varepsilon_2 = 2nk$.

The light beams incident on the sample and reflected define a plane of incidence. *p* polarized (parallel) beam has electric field parallel and *s* polarized beam (German for senkrecht) perpendicular to the plane of incidence. *p* and *s* polarization and direction of propagation of light (in that order) define a right-handed Cartesian coordinate system. This convention is used to describe the polarization of light beam.

Polarization state of a light beam refers to the path its electric field traces as it propagates through space and time. There are three classifications of polarization used to describe a plane wave: linear, circular and elliptical.

Jones calculus

Polarized light can be described using the Jones calculus. A totally polarized beam can be expressed by specifying the components of the electric field of beam along the *p* and *s* polarization directions. If we recall the solution of electric field wave equation given with:

Eq. 2. 10 $\qquad \vec{E}(\vec{r}, t) = \vec{E}_0 exp\, (i\frac{\omega \tilde{n}}{c} \vec{r}) exp\, (-i\omega t + \phi)$

The Jones vector represents can be expressed as:

Eq. 2. 11 $\qquad \vec{E}_0 = \begin{bmatrix} \tilde{E}_p \\ \tilde{E}_s \end{bmatrix}$

where $\tilde{E}_p$ and $\tilde{E}_s$ correspond to *p* and *s* polarization, respectively. The overall effect of any optical component, including the sample, on polarization state of the propagating beam can now be expressed by a 2×2 transfer matrix, known as the Jones matrix. The diagonal elements of the Jones matrix represent the change of amplitude and phase of the *p* and *s* components of the beam, while the off-diagonal elements describe the transfer of energy from

the p-component to the s-component, and vice versa. The Jones matrix provides a means of describing optical systems.

Electric field vector of linearly polarized light in a plane perpendicular to the direction of propagation ($x - y$ plane) maintains the same direction. The tip of the electric field vector traces out a line segment as a function of time (*Figure 2. 6*) [34]. The Jones vector representation of linearly polarized light is $\begin{bmatrix} |\tilde{E}_p|e^{i\phi} \\ |\tilde{E}_s|e^{i\phi} \end{bmatrix}$, where ϕ is a phase angle, which must be identical for both components.
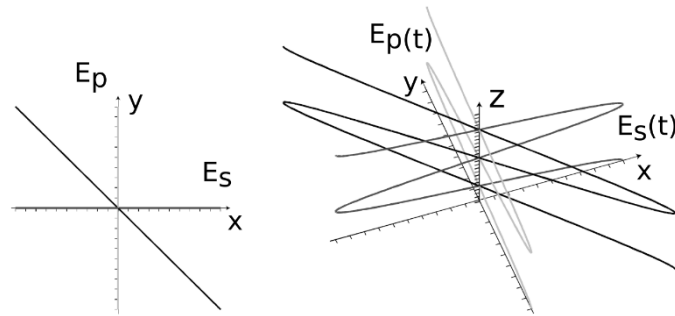
Figure 2. 6. Linearly polarized light in the *x-y* plane (left) and 3D depiction (right).

If the $\tilde{E}_s$ and $\tilde{E}_p$ are equal in magnitude, but 90° out of phase, the polarization state is circular because the tip of the total electric field vector traces out a circle as a function of time (*Figure 2. 7*) [34]. If faced toward the propagating beam, the electric field vector is precessing counterclockwise, the beam is left-circularly polarized, and if the vector is precessing clockwise, the beam is right-circularly polarized.
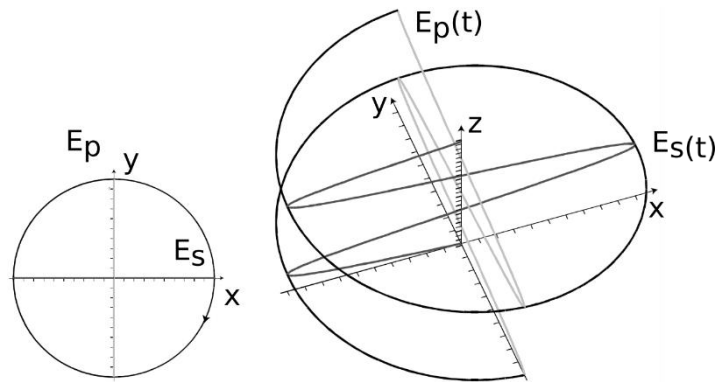

Figure 2. 7. Circularly polarized light in the *x-y* plane (left) and 3D depiction (right).

In general, the $\tilde{E}_s$ and $\tilde{E}_p$ fields do not have to be equal in magnitude, and they could have any phase relationship. For a general polarization state, the tip of the total electric field

vector traces out an ellipse as a function of time (*Figure 2. 8*). Linear and circular polarizations are special cases of elliptically polarized light.

The beam is randomly polarized (unpolarized) if it does not exhibit a well defined polarization state. Unpolarized light cannot be represented in the Jones vector formalism, but with four-component Stokes vector [35].

A light beam does not have to exhibit a well defined polarization state. This is the case when a polarized beam is reflected from a non-ideal film (surface roughness, thickness non-uniformity, refractive index non-homogeneity), or a transparent substrate exhibiting back surface reflection effects. This is referred to as partially polarized light. Partially polarized beams cannot be represented with a single Jones vector, but may be represented with a sum of Jones vectors or a single four-component Stokes vector, similar to unpolarized light. Interaction of unpolarized or partially polarized light with optical systems is described by Mueller calculus [36].
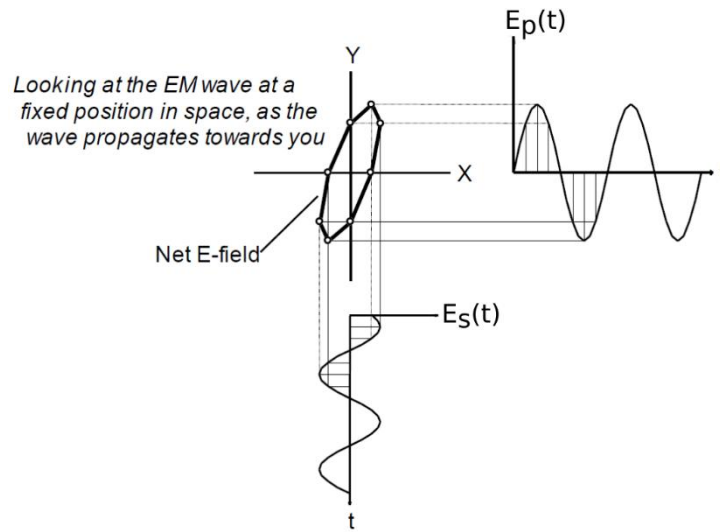

Figure 2. 8. General elliptically polarized light; looking into the propagating beam [32].

Dispersion models used in ellipsometry

Optical constants (complex dielectric functions and complex index of refraction) are functions of wavelength. Kramers-Kronig relation is a consequence of the fact that the materials response to an applied electric field occurs after the application of the field. It relates the real and imaginary parts of the complex dielectric function:

Eq. 2. 12 $$\varepsilon_1(E) - 1 = \frac{2}{\pi} P \int_0^\infty \frac{E' \varepsilon_2(E')}{E'^2 - E^2} dDE',$$

Eq. 2. 13
$$\varepsilon_2(E) = -\frac{2E}{\pi} P \int_0^\infty \frac{\varepsilon_1(E') - 1}{E'^2 - E^2} dDE'.$$

The equations show that the real part of the dielectric function, $\varepsilon_1(E)$, can be obtained from the imaginary part ε_2, and the imaginary part can be obtained from the real part of the function. Kramers-Kronig consistent $\tilde{\varepsilon}$, and $\tilde{n}$ graphs are presented in *Figure 2. 9*.

Dispersion models describe the optical constants dependence on radiation wavelength. The model depends on the specific light-matter interaction processes that take place in the spectral range of interest.

Lorentz oscillator model is the most general dispersion model describing the variation of optical constants around resonance. It is given by:

Eq. 2. 14
$$\tilde{\varepsilon}(\omega) = \varepsilon_\infty + \frac{\aleph}{m_0 \epsilon_0} \frac{1}{\omega_0^2 - \omega^2 - i\gamma\omega}$$

with plasma frequency, ω_p^2, defined as:

Eq. 2. 15
$$\omega_p^2 = \frac{\aleph e^2}{m_0 \epsilon_0}$$

where $\aleph$ is number density of electrons, e is electron charge, m_0 is electron mass, ϵ_0 is the air permittivity, ω_0 is characteristic resonance of the material, ω is the frequency of the electromagnetic wave, γ a dampening term and ε_∞ s an additional offset term. Lorentz oscillator has long absorption tails, and can cause unwanted absorption in transparent regions [37].

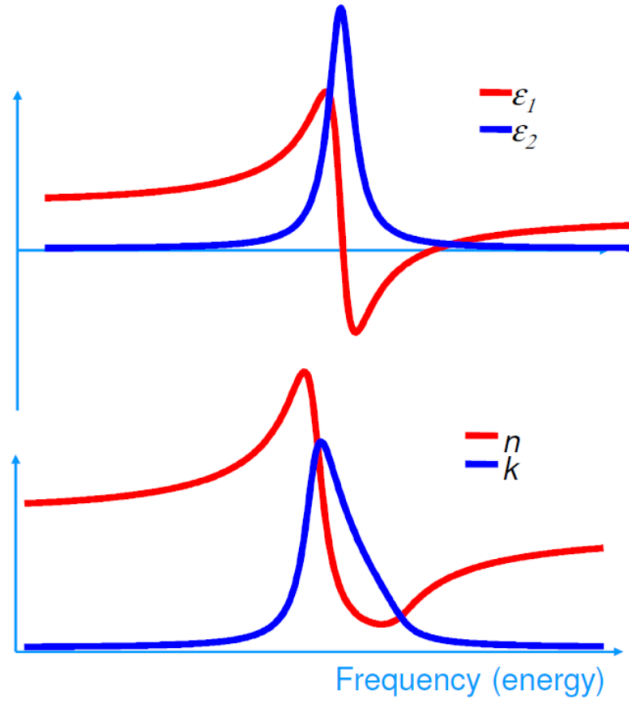Figure 2. 9. ε_1 and n are increasing except at frequencies for which the material is absorbing.

Gauss model is assuming Gaussian distribution of Lorentz oscillators and given by:

Eq. 2. 16
$$\tilde{\varepsilon}(\omega) = \varepsilon_\infty + \frac{1}{\sqrt{2\pi}\sigma_0} \int_{-\infty}^{+\infty} exp - \left(\frac{(x-\omega_0)}{2\sigma_0^2}\right) \frac{\omega_p^2}{x^2-\omega^2-i\gamma\omega} dx$$

where σ_0 is Gaussian broadening and x is the variable of integration. Imaginary dielectric function, ε_2, of Gauss model approaches zero beyond the full width at half maximum (FWHM) positions more rapidly than ε_2 of Lorentz oscillator model. Comparison of Gauss and Lorentz oscillator model is given in *Figure 2. 10*. Gauss model is used for amorphous materials and for systems showing a distribution of resonances rather than a single resonance.
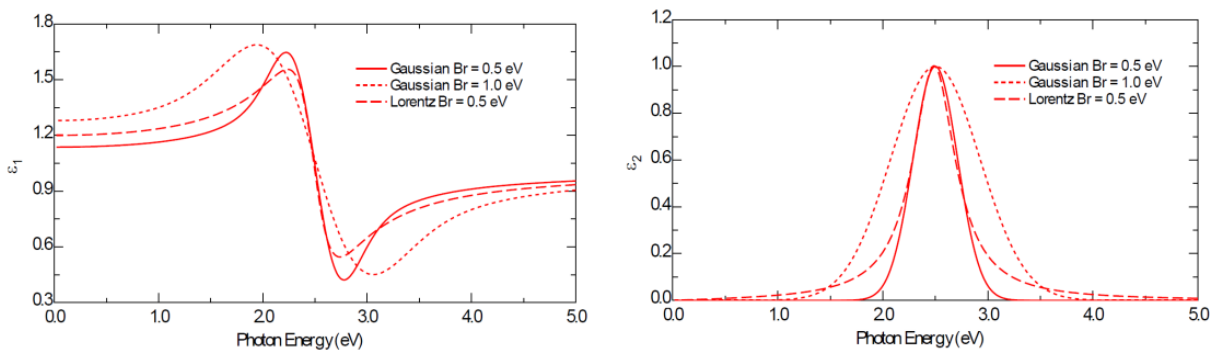

Figure 2. 10. Comparison of a) real and b) imaginary dielectric function of two Gaussian and one Lorentz oscillator [32].

Drude model describes free carrier effects on the dielectric response. The model makes use of a Lorentz oscillator with $\omega_o = 0$ (e.g. there is no restoring force). The Drude model is given by the equation:

Eq. 2. 17 $$\tilde{\varepsilon}(\omega) = \varepsilon_\infty - \frac{\omega_p^2}{\omega(\omega + i\gamma)}$$

The quantity ε_∞ describes residual dielectric constant absorptions at frequencies much greater than plasma frequency, ω_p. Drude model is most often used to model metals. Doped semiconductors and conductive dielectrics can also be modelled.

Cauchy model describes the refractive index, n, of materials with extinction coefficient $k(\lambda) = 0$. n of dielectrics and semiconductors can be represented by a slowly varying function of wavelength, λ:

Eq. 2. 18 $$n(\lambda) = A + \frac{B}{\lambda^2} + \frac{C}{\lambda^4}$$

where A sets the refractive index range, and B and C give dispersion shape. It can be obtained by Taylor expansion of the Lorentz oscillator at large ω. Refractive index of SK11 glass obtained by Cauchy model is presented in *Figure 2. 11*.

The Cauchy model can be applied to many transparent materials. It is not applicable to metals or semiconductors above the fundamental bandgap.
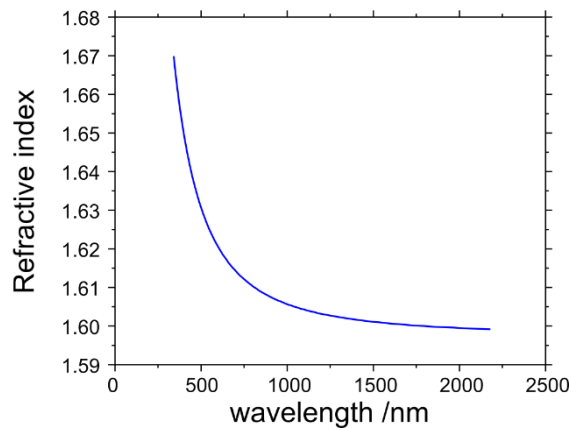

Figure 2. 11. *n* of SK11 glass obtained by Cauchy model.

Sellmeier model uses Lorentz oscillators with zero broadening ($\gamma = 0$) and for a sum of oscillators is given by equation:

Eq. 2. 19 $$n^2(\lambda) = \varepsilon_\infty + \sum_i \frac{A_i \lambda^2}{\lambda^2 - \lambda_i^2}$$

16

where $i-$th oscillator has an amplitude A and resonant wavelength λ_i.
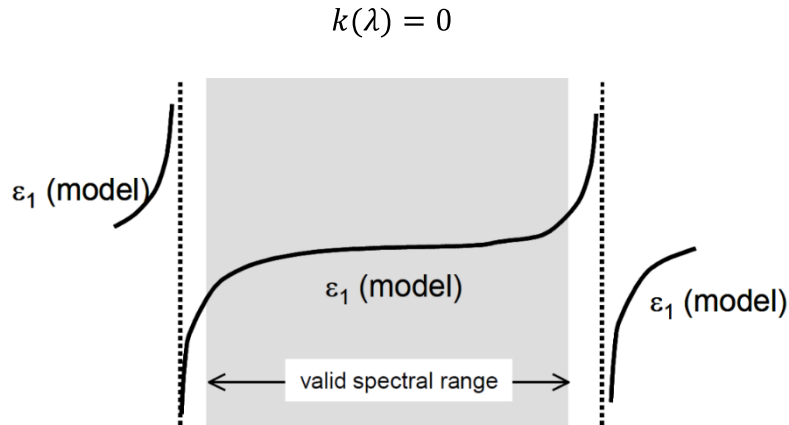
$$k(\lambda) = 0$$

Figure 2. 12. ε_1 plot showing the dispersion obtained from Sellmeier model. The energies at the centre of oscillator peaks are outside the models valid spectral range.

Sellmeier dispersion models a material as a collection of oscillating dipoles with a resonant frequency, but no absorption. The Sellmeier model is employed to simulate dispersion in ε_1 induced by absorption occurring outside the measured spectral range (*Figure 2. 12*) [38].

Dielectrics

There exist many other dispersion models, but those presented here describe the properties of materials investigated in this work. Glass substrates and dielectric materials such as SiO2 are typically modeled with the Sellmeier dispersion model. Other dielectric materials such as TiO2 are better described with the Cauchy model which provides more flexibility in describing the refractive index dispersion.

Metals

Regarding metals, the free electron (conduction electrons) response is well described with the Drude model. In the case of metal films consisting of isolated particles, the free electrons can resonantly oscillate in the visible range as they are confined by the particle. This localized surface plasmon resonance (LSPR) turns out to be best described with Gaussian oscillators. In the case of percolated yet not compact films, usually both contributions (Drude and Gaussian oscillators) have to be taken into account to represent both the metal percolated network and not-connected islands. In addition to the free electron response, the contribution of bound electrons through interband transitions (in UV for Ag and partially in visible for Cu and Au [39] has to be considered as well. These interband transitions can be also well-modelled with Gaussian oscillators.

Inhomogeneous refractive index

In some cases, thin film materials or glass substrates present an in-depth variation of the refractive index ($n(d)$) due to varying spatial composition or density. This inhomogeneous refractive index can be usually well approximated as a set of thin sublayers of constant n.

Material mixtures: effective medium approximations

In some cases, films are formed by a mixture of two or more materials. If the microstructures composing the mixture are large enough so they can be characterized by their own optical constants and, at the same time, much smaller than the wavelength of the incoming radiation, the medium can be treated as microscopically heterogeneous and macroscopically homogeneous and represented with effective optical constants. There are several EMA that establish a mathematical relation between the effective optical constants and the optical constants of the mixing materials and some geometrical parameters, usually the volume fraction of the constituents [40]. The most widely used models for two-materials mixtures are: i) the Maxwell-Garnett theory, applied to unsymmetric mixtures in which one constituent can be treated as host and the other as inclusions and ii) the Bruggeman theory, in which both materials are treated in a symmetric way and assumed to be embedded in the effective medium itself. The Bruggeman EMA is used in this work to represent surface roughness or porous layers as mixtures of material and voids.

Localized surface plasmon resonance in nanoparticle films

As mentioned before, the optical properties of metal nanoparticles are characterized by the LSPR which is a non-propagating (i.e., localized at the particle) resonant excitation of the conduction (i.e., free) electrons of the metal coupled to the incident electromagnetic field. In order to understand under what conditions this electron excitation can be driven to resonance, one can look at polarizability α of a spherical particle of radius r and dielectric function ε_m embedded in a host medium with dielectric function ε_h [41]:

$$\alpha = 4\pi r^3 \frac{\varepsilon_m - \varepsilon_h}{\varepsilon_m + 2\varepsilon_h},$$

Eq. 2. 20

and therefore, the particle polarizability, and hence, the optical response, will present a resonant behavior when

Eq. 2. 21
$$\left| \varepsilon_{1m} + 2\varepsilon_h \right| \to 0.$$

This condition (the LSPR condition) is achieved in good approximation in the visible and near-infrared ranges when combining most dielectric materials (that have $\varepsilon_h.{>}0)$ with noble metals ($\varepsilon_h.{<}0$). It should be noted that metals have non-zero imaginary part of the dielectric function and the polarizability can not diverge. In the visible range, Ag displays the smallest imaginary part and hence Ag nanostructures typically display the strongest LSPR [10].

Increasing the dielectric function of the matrix requires more negative values of the dielectric function of the metal to excite the LSPR what, according to the Drude model, is obtained at a lower frequency (or longer wavelength) and thus the LSPR red-shifts. If the particles are elongated or if there is electromagnetic coupling among them, the LSPR also red-shifts [10].

Films containing metal nanoparticles, such as metal island films, could be in principle described through EMAs. Usually, the Maxwell-Garnett expression or some extension based on it is used for "particles-in-matrix" geometry that reflects the appearance of the LSPR. However, these models provide only qualitative agreement with experimental data due to the complex shape and size distribution of nanoparticles in island films. Hence, it turns out that more flexible models, such as Gaussian oscillators, are necessary to accurately describe the optical properties of MIFs [40].

2.2.2. Optics of multilayers

Fresnel coefficients

Figure 2. 13. depicts a light beam propagating in material of refractive index $\tilde{n}_1$ and interacting with the medium of refractive index $\tilde{n}_2$. Electric field incident on the interface of the two materials is denoted by E_i. The reflected and transmitted (refracted) beam are denoted E_r and E_t, respectively. Magnetic field B_i, B_r and B_t is defined in a similar manner for incident, reflected and transmitted beam, respectively. θ_i, θ_r, and θ_t are angles that the incident, reflected and transmitted beam makes with normal to the sample surface, respectively. The law of reflection states that angle of reflection, θ_r, equals the angle of incidence, θ_i [42]. The law of refraction, Snell's law is given by:

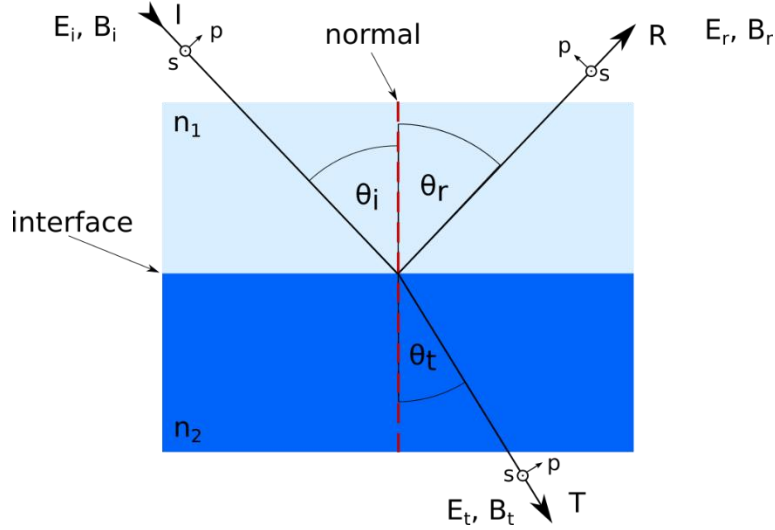Eq. 2. 22 $\qquad \tilde{n}_1 \sin \theta_i = \tilde{n}_2 \sin \theta_t$

Figure 2. 13. Variables used in Fresnel equations. The incoming beam is reflected and refracted at the interface between two mediums.

Electromagnetic wave can be represented with two perpendicular components of polarization, s and p, for electric field, $\vec{E}$, and in a similar way for magnetic field, $\vec{B}$. *Figure 2. 13*. shows an incident beam partially reflected and transmitted at the interface of the materials with refractive indices $\tilde{n}_1$ and $\tilde{n}_2$. Separating electromagnetic wave into two components results with E_s (or $E_\perp$, lying in a plane perpendicular to incident plane) and E_s(or $E_\parallel$, lying in incident plane). For E_s the horizontal component of the corresponding magnetic field equals $B \cos \theta_i$, while vertical component is $B \sin \theta_i$. Boundary conditions are given with the condition that components of $\vec{E}$ and $\vec{B}$ of the incident wave parallel to the interface are transmitted through the interface of materials 1 and 2:

Eq. 2. 23
$$E_{1horizontal} = E_{2horizontal}$$

Eq. 2. 24
$$B_{1horizontal} = B_{2horizontal}$$

These conditions are used to develop two equations:

Eq. 2. 25
$$E_i + E_r = E_t$$

Eq. 2. 26
$$B_i \cos \theta_i + B_r \cos \theta_r = B_t \cos \theta_t$$

substituting $\theta_r$for θ_i, and B for $(\tilde{n}E)/c$, where $c$is the speed of light in vacuum, results in Fresnel reflection and transmission coefficients for s polarized light:

Eq. 2. 27
$$\tilde{r}_s = \frac{E_{r\perp}}{E_{i\perp}} = \frac{E_{rs}}{E_{is}} = |\tilde{r}_s|e^{(i\delta_{rs})} = \frac{\tilde{n}_1 \cos \theta_i - \tilde{n}_2 \cos \theta_t}{\tilde{n}_1 \cos \theta_i + \tilde{n}_2 \cos \theta_t}$$

Eq. 2. 28
$$\tilde{t}_s = \frac{E_{t\perp}}{E_{i\perp}} = \frac{E_{ts}}{E_{is}} = |\tilde{t}_s|e^{(i\delta_{ts})} = \frac{2\tilde{n}_1 \cos \theta_i}{\tilde{n}_1 \cos \theta_i + \tilde{n}_2 \cos \theta_t}$$

Fresnel coefficients for $p-$polarization are found in a similar way with the two equations stemming from the boundary conditions equal to:

Eq. 2. 29 $\qquad B_i + B_r = B_t$

Eq. 2. 30 $\qquad E_i \cos\theta_i + E_r \cos\theta_r = E_t \cos\theta_t$

Solving the equations gives:

Eq. 2. 31 $\qquad \tilde{r}_p = \dfrac{E_{r\parallel}}{E_{i\parallel}} = \dfrac{E_{rp}}{E_{ip}} = |\tilde{r}_p| e^{(i\delta_{rp})} = \dfrac{\tilde{n}_2 \cos\theta_i - \tilde{n}_1 \cos\theta_t}{\tilde{n}_2 \cos\theta_i + \tilde{n}_1 \cos\theta_t}$

Eq. 2. 32 $\qquad \tilde{t}_p = \dfrac{E_{t\parallel}}{E_{i\parallel}} = \dfrac{E_{tp}}{E_{ip}} = |\tilde{t}_p| e^{(i\delta_{tp})} = \dfrac{2\tilde{n}_1 \cos\theta_i}{\tilde{n}_2 \cos\theta_i + \tilde{n}_1 \cos\theta_t}$

Reflectance, R is the ratio of reflected intensity to the incident intensity of the beam:

Eq. 2. 33 $\qquad R_p = |\tilde{r}_p|^2 \qquad R_s = |\tilde{r}_s|^2$

Fresnel coefficients in multilayer system of thin films

A typical thin film on a substrate is presented on *Figure 2. 14*. Summing the partial waves reflected at interface 1-2 and interface 2-3 results in a geometric series that after evaluation gives total reflection coefficients [43]. The partial reflected waves are expressed with Fresnel coefficients r_{12}, r_{23},... The geometric series of multiply reflected beam is given with:

Eq. 2. 34 $\qquad \tilde{R}_p = \dfrac{E_{rp}}{E_{ip}} = |\tilde{R}_p| e^{(i\delta_{rp})} = \dfrac{\tilde{r}_{12,p} + \tilde{r}_{23,p} e^{-2i\gamma}}{1 + \tilde{r}_{12,p}\tilde{r}_{23,p} e^{-2i\gamma}}$

Eq. 2. 35 $\qquad \tilde{R}_s = \dfrac{E_{rs}}{E_{is}} = |\tilde{R}_s| e^{(i\delta_{rs})} = \dfrac{\tilde{r}_{12,s} + \tilde{r}_{23,s} e^{-2i\gamma}}{1 + \tilde{r}_{12,s}\tilde{r}_{23,s} e^{-2i\gamma}}$

where $\tilde{R}_p$ and $\tilde{R}_s$ are total Fresnel reflection coefficients. Reflection coefficients $\tilde{r}_{12,p}$ and $\tilde{r}_{12,s}$ as well as $\tilde{r}_{23,p}$ and $\tilde{r}_{23,s}$ describe reflection of p and s polarized light at interfaces between air and thin film, and thin film and substrate, respectively. Total Fresnel transmission coefficients can be obtained in a similar manner.
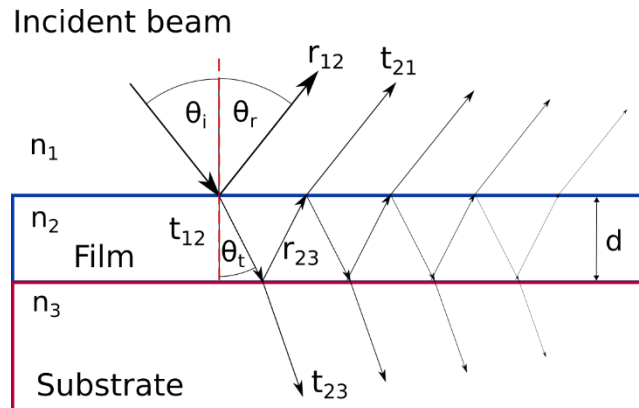

21

Figure 2. 14. Schematic of multiple light beam reflections and transmissions on a thin film.

Employing Snell's law (Eq. 2. *22*) and rearranging gives:

Eq. 2. 36 $$\cos \theta_t = \sqrt{1 - (\frac{n_1}{n_2} \sin \theta_i)^2}$$

The thickness of thin film and the phase difference of the reflected p and s polarized beams are contained in the phase term of Eq. 2. *34* and Eq. 2. *35*:

Eq. 2. 37 $$\gamma = \frac{2\pi d}{\lambda} \sqrt{n_2^2 - n_1^2 \sin^2 \theta_i}$$

where γ is complex for absorbing media, i.e. $\gamma = \gamma_1 + i\gamma_2$ and d is the thickness of thin film.

When multiple interfaces are present the reflectance **R** is given by:

Eq. 2. 38 $$Rp = |\tilde{R}_p|^2 \qquad Rs = |\tilde{R}_s|^2$$

rather than by Eq. 2. *33*.

Calculation of multilayer properties

There are multiple approaches to calculating optical constants and thickness of layers in a multilayer film. Transfer matrix method [44] is one of them.

Optical system consists of m layers and is placed between semi-infinite materials with refractive indices $\tilde{n}_0$ and $\tilde{n}_{m+1}$. The incident, reflected and transmitted light beam are represented with E^i, E^r and E^t, respectively. The angle that incident/reflected light beam makes with normal to the sample surface is θ^o and the angle the transmitted light beam makes with normal is θ_{m+1} (*Figure 2. 15*) [45].
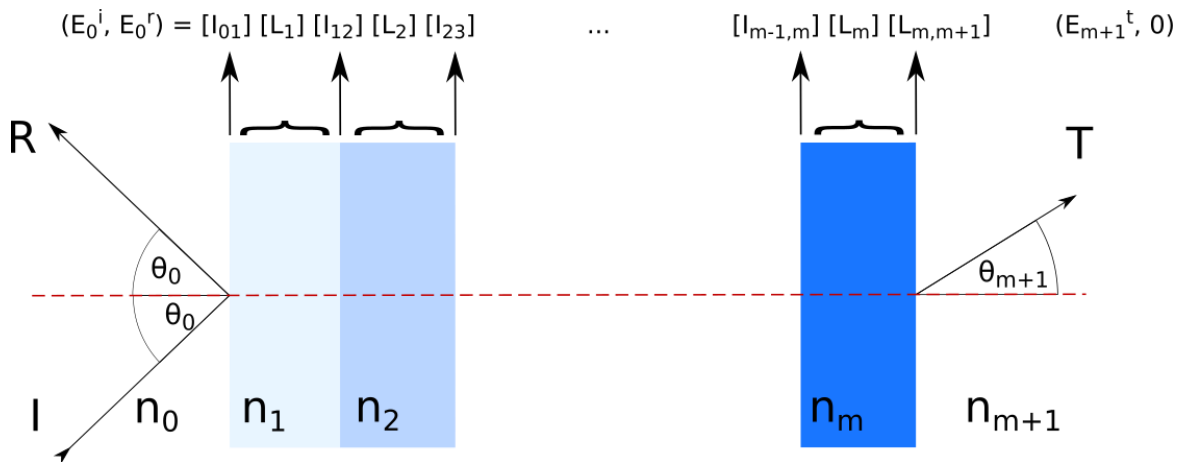
Figure 2. 15. Schematic of multilayer system with m layers. Calculation algorithm is shown schematically at the top.

Due to the linear character that governs the equations of propagation of light in a material and the continuity of the tangential components of the field on the surfaces separating the media, we can write the relationship between the electric field at the output (E_{m+1}) and the input (E_0) of the multilayer structure in a matrix form [45]:

Eq. 2. 39
$$\begin{bmatrix} E_0^i \\ E_0^r \end{bmatrix} = \begin{bmatrix} S_{11} & S_{12} \\ S_{21} & S_{22} \end{bmatrix} \begin{bmatrix} E_{m+1}^t \\ 0 \end{bmatrix} = S \begin{bmatrix} E_{m+1}^t \\ 0 \end{bmatrix}$$

The scattering matrix S determines the optical properties of the system. It enables calculation of total reflection and transmission coefficients of multilayer structure. S can be expressed as a product of interface matrices, (I), which describe properties between incoming, transmitted and reflected fields at interfaces, and the layer matrices (L), that relate the fields at each side of a layer:

Eq. 2. 40
$$S = I_{01} L_1 L_{12} L_2 \dots I_{j-1,j} L_j I_{j,j+1} \dots L_m I_{m,(m+1)}$$

The interface matrices are determined by Fresnel coefficients $(\tilde{r}_{j,j+1}, \tilde{t}_{j,j+1})$ for each interface and are different for each type of polarization [46], while the layer matrices express the propagation of the wave in a medium of refractive index n_j and thickness d_j:

Eq. 2. 41
$$I_{j,j+1} = \frac{1}{\tilde{t}_{j,j+1}} \begin{bmatrix} 1 & \tilde{r}_{j,j+1} \\ \tilde{r}_{j,j+1} & 1 \end{bmatrix}$$

Eq. 2. 42
$$L_j = \begin{bmatrix} exp\,(i\gamma_j) & 0 \\ 0 & exp\,(-i\gamma_j) \end{bmatrix}$$

where i is the imaginary unit, and the phase factor γ_j is given by:

Eq. 2. 43
$$\gamma_j = \frac{2\pi d_j \tilde{n}_j}{\lambda} cos\,\theta_j$$

where θ_j is the angle that the direction of propagation of the incoming wave forms with the z axis at the j-th interface.

The main advantage of this method is that different physical phenomena involved (propagation in homogeneous media, reflection and refraction at each interface) are represented independently by corresponding matrix [47, 48].

Ellipsometric Ψ and Δ functions

23

Ellipsometry is a technique for measurements of materials optical properties based on the change in polarization state of light upon reflection from (or transmission through) the surface of the sample. It will be described in more details in the next chapter. Here will be explained how ellipsometric Ψ and Δ functions are defined.

The ratio of total Fresnel reflection coefficients, $\tilde{R}_p$ and $\tilde{R}_s$ in standard ellipsometry, or total Fresnel transmission coefficients, $\tilde{T}_p$ and $\tilde{T}_s$, in transmission ellipsometry, contains the amplitude ratio information, as well as phase difference of p and s polarized light. The ratio of total Fresnel coefficients, ellipsometric ratio $\tilde{\rho}$, is equal to:

Eq. 2. 44
$$\tilde{\rho} = \frac{\tilde{R}_p}{\tilde{R}_s} = \frac{E_{rp}/E_{ip}}{E_{rs}/E_{is}} = \frac{|\tilde{R}_p|}{|\tilde{R}_s|} e^{i(\delta_{rp}-\delta_{rs})} = tan\,\Psi e^{i\Delta}$$

Eq. 2. 45
$$\tilde{\rho} = \frac{\tilde{T}_p}{\tilde{T}_s} = \frac{E_{tp}/E_{ip}}{E_{ts}/E_{is}} = \frac{|\tilde{T}_p|}{|\tilde{T}_s|} e^{i(\delta_{tp}-\delta_{ts})} = tan\,\Psi e^{i\Delta}$$

for standard and transmission ellipsometry, respectively.

Ψ and Δ are angles describing the total reflected and transmitted light. *Tan Ψ* is defined as the absolute value of p and s polarized Fresnel reflection and transmission coefficient ratio, respectively [32]:

Eq. 2. 46
$$tan\,\Psi = \frac{|\tilde{R}_p|}{|\tilde{R}_s|} \qquad\qquad tan\,\Psi = \frac{|\tilde{T}_p|}{|\tilde{T}_s|}$$

Δ represents the relative phase change of the p and s polarised light:

Eq. 2. 47
$$\Delta = \delta_p - \delta_s$$

In a special case of single reflection from the surface, or transmission through the interface, given with Eq. 2. *27*, Eq. 2. *28*, Eq. 2. *31* and Eq. 2. *32*, the ellipsometric ratio $\tilde{\rho}$ is given with:

Eq. 2. 48
$$\tilde{\rho} = \frac{\tilde{r}_p}{\tilde{r}_s} = \frac{E_{rp}/E_{ip}}{E_{rs}/E_{is}} = \frac{|\tilde{r}_p|}{|\tilde{r}_s|} e^{i(\delta_{rp}-\delta_{rs})} = tan\,\Psi e^{i\Delta}$$

Eq. 2. 49
$$\tilde{\rho} = \frac{\tilde{t}_p}{\tilde{t}_s} = \frac{E_{tp}/E_{ip}}{E_{ts}/E_{is}} = \frac{|\tilde{t}_p|}{|\tilde{t}_s|} e^{i(\delta_{tp}-\delta_{ts})} = tan\,\Psi e^{i\Delta}$$

Similar to equations (2.38) and (2.39) tan Ψ and Δ are [32]:

Eq. 2. 50
$$tan\,\Psi = \frac{|\tilde{r}_p|}{|\tilde{r}_s|} \qquad\qquad tan\,\Psi = \frac{|\tilde{t}_p|}{|\tilde{t}_s|}$$

Ellipsometric functions Ψ and Δ are obtained by measuring the intensity of the probe beam after interaction with the sample. Light is detected at the detector and converted to current. The intensity of the signal depends on the polarization of the detected light.

Ellipsometer configurations differ in the way Ψ and Δ are derived, but for a better sense of underlying mathematics, the ellipsometric Ψ and Δ of the rotating analyzer ellipsometer (used in this work) will be discussed in detail. *Figure 2. 16* [32] represents graphs of the light intensity obtained at the detector for linearly, circularly and elliptically polarized beam on a rotating analyzer ellipsometer.
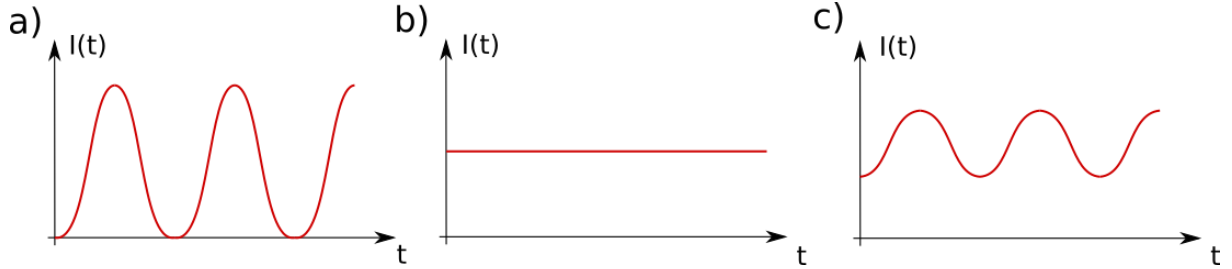

Figure 2. 16. Detector signal of a) linearly, b) circularly, and c) elliptically polarized beam at the detector.

Jones calculus is used to relate Ψ and Δ in terms of the optical properties of the sample and the polarizer and analyzer azimuthal angles. Time dependent beam intensity I(t) at the detector, the actual quantity measured, needs to be calculated for this purpose.

The detector intensity is proportional to the magnitude of the electric field of the beam squared: $I_D \propto |E_D|^2$. The expression for electric field of the beam at the detector, E_D, is expressed by multiplying, in the order of interaction, the electric field of the input beam by the Jones matrices of optical elements in the system. The expression for the beam at the detector is given with:

Eq. 2. 51

$$E_D = [Analyzer\ matrix] \cdot [Sample\ matrix] \cdot [Polarizer\ matrix] \cdot [Input\ beam]$$

Expressions of the optical elements are given with Jones matrices of polarizer, sample and analyzer.

If the polarizer is positioned so that that the axis of the input polarizer is in the plane of incidence, the beam leaving the polarizer is *p* polarized.

P is the input polarizer azimuth with respect to the plane of incidence. Polarizer azimuth is 0° in this case. Jones vector of a *p* polarized beam propagating through the polarizer with polarizer azimuth 0° is given with:

Eq. 2. 52

$$[Polarizer\ matrix] \cdot [p - polarized\ Input\ beam] = \begin{bmatrix} cos\ P & -sin\ P \\ sin\ P & cos\ P \end{bmatrix} \cdot \begin{bmatrix} 1 \\ 0 \end{bmatrix}$$

If the sample is isotropic and has a smooth surface, no off-diagonal elements will be present in the sample Jones matrix:

Eq. 2. 53
$$[Sample\ Jones\ matrix] = \begin{bmatrix} \tilde{R}_p & 0 \\ 0 & \tilde{R}_s \end{bmatrix}$$

The analyzer Jones matrix is evaluated by rotating the coordinate system so that the new p polarization lies along the analyzer axis and then multiplying with the p oriented Jones matrix. There is no need to go back to ellipsometer frame of reference, as the final rotation matrix will drop out in the evaluation of the square of the electric field. The total Jones matrix for the analyzer is given with:

Eq. 2. 54
$$[Analyzer\ Jones\ matrix] = \begin{bmatrix} 1 & 0 \\ 0 & 0 \end{bmatrix} \cdot \begin{bmatrix} cos\ A & sin\ A \\ -sin\ A & cos\ A \end{bmatrix}$$

where A is the angle between the analyzer axis and p plane.

The expression of the electric field at the detector is than given with:

Eq. 2. 55
$$E_D = \begin{bmatrix} 1 & 0 \\ 0 & 0 \end{bmatrix} \cdot \begin{bmatrix} cos\ A & sin\ A \\ -sin\ A & cos\ A \end{bmatrix} \cdot \begin{bmatrix} \tilde{R}_p & 0 \\ 0 & \tilde{R}_s \end{bmatrix} \cdot \begin{bmatrix} cos\ P & -sin\ P \\ sin\ P & cos\ P \end{bmatrix} \cdot \begin{bmatrix} 1 \\ 0 \end{bmatrix}$$

This equation after evaluation gives the following Jones vector as a result:

Eq. 2. 56
$$E_D = \begin{bmatrix} \tilde{R}_p\ cos\ P\ cos\ A + \tilde{R}_s\ sin\ P\ sin\ A \\ 0 \end{bmatrix}$$

The intensity of the beam can be calculated by multiplying the non-zero element in the Jones vector by its complex conjugate. After multiplication and including a few trigonometric identities the following result is obtained:

Eq. 2. 57
$$I_D \propto \left| \tilde{R}_p \right|^2 cos^2\ P + \left| \tilde{R}_s \right|^2 sin^2\ P +$$

$$+ \left[\left| \tilde{R}_p \right|^2 cos^2\ P - \left| \tilde{R}_s \right|^2 sin^2\ P \right] cos(2A) +$$

$$+ 2\Re e(\tilde{R}_p \tilde{R}_s^*) sin\ P\ cos\ P\ sin(2A)$$

Normalizing this equation so that the constant term is unity by dividing by the term independent of the azimuthal angle A yields:

Eq. 2. 58
$$I_D \propto 1 + \frac{\left|\frac{\tilde{R}_p}{\tilde{R}_s}\right| - tan^2 P}{\left|\frac{\tilde{R}_p}{\tilde{R}_s}\right| + tan^2 P} cos(2A) + \frac{2\Re e\left|\frac{\tilde{R}_p}{\tilde{R}_s}\right| tan P}{\left|\frac{\tilde{R}_p}{\tilde{R}_s}\right| + tan^2 P} sin(2A)$$

Tan Ψ and *tan Δ* are defined to substitute the ratios of total Fresnel coefficients of reflection to arrive to:

Eq. 2. 59
$$I_D \propto 1 + \frac{tan^2 \Psi - tan^2 P}{tan^2 \Psi + tan^2 P} cos(2A) + \frac{2 \, tan \Psi \, cos \Delta \, tan P}{tan^2 \Psi + tan^2 P} sin(2A)$$

This expression has the form of Fourier series in twice the analyzer azimuthal angle:

Eq. 2. 60
$$I_D \propto 1 + \alpha \, cos(2A) + \beta \, sin(2A)$$

The $A(t)$ is the instantaneous azimuth of the analyzer transmission axis given with:

Eq. 2. 61
$$A = \omega t + \theta$$

α and β are normalized Fourier coefficients of the signal. They can be represented in terms of Ψ and Δ:

Eq. 2. 62
$$\alpha = \frac{tan^2 \Psi - tan^2 P}{tan^2 \Psi + tan^2 P}$$

Eq. 2. 63
$$\beta = \frac{2 \, tan \Psi \, cos \Delta \, tan P}{tan^2 \Psi + tan^2 P}$$

These equations are inverted to obtain Ψ and Δ from the measured α, β and known P:

Eq. 2. 64
$$tan \Psi = \sqrt{\frac{1+\alpha}{1-\alpha}} |tan P|$$

Eq. 2. 65
$$cos \Delta = \frac{\beta}{\sqrt{1-\alpha^2}} \frac{tan P}{|tan P|}$$

It is important to note that deriving Ψ and Δ depends on the ellipsometer configuration used due to:

· usage of different optical components

· ability of some of the components to change azimuthal angles

· arrangement of optical components in the system.

2.3. Measurement, characterization and design of thin films optical properties

The most common technique for measurements of thin film optical properties is spectrophotometry that is measuring intensity of the light beam reflected or transmitted by the sample. It acquires one data point (reflectance or transmittance) per wavelength of the

incident light beam spectrum. Ellipsometry is coming more into the use as measured data contain more information (not only intensity, beam polarization state as well) making this technique more sensitive to samples optical properties.

Samples optical parameters (such as film thickness, complex refractive index, surface roughness, etc.) are obtained by optical characterization based on measurements. in the course of characterization the sample is presented by a model which parameters are varied until satisfactory accordance of models optical properties with experimental data (i.e. fit) is obtained.

Design of multilayers optical properties is basically similar to optical characterization: it starts from the model with known optical parameters and optimizes them until desired optical properties, defined here as target properties, are achieved.

2.3.1. Ellipsometry

As mentioned before, ellipsometry measures the change in polarization state of light upon reflection from (or transmission through) the surface of the sample [49] (*Figure 2. 17*).
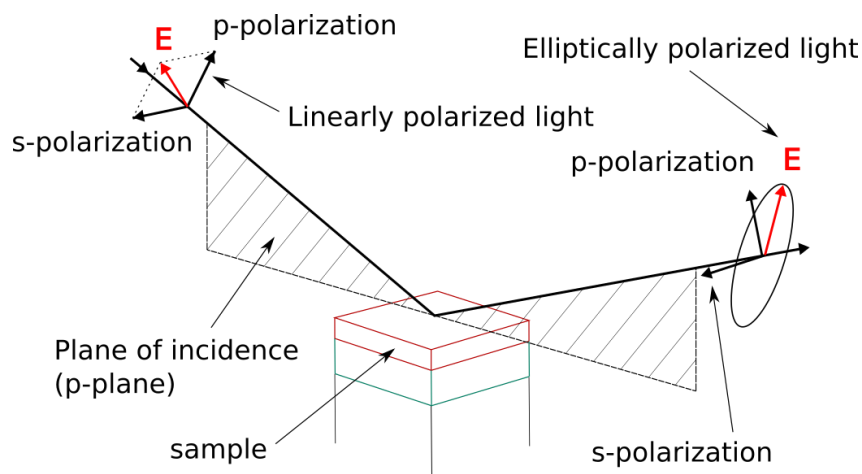
Figure 2. 17. Geometry of ellipsometric measurements.

Variable angle ellipsometry uses multiple angles of incident light to acquire data from the sample [50]. Combining the spectroscopic and variable angle ellipsometry in a single device allows for characterization of complex materials and structures.

Ellipsometer setup has the following components: light source, modulator, polarizer/analyzer, compensator, retarder and detector (Figure 2. *18*). Polarizer is the most

important optical element in ellipsometer. It is an optical filter used to transmit a specific polarization state of unpolarized or partially polarized light [51]. Ideally, it transmits light polarized in one direction. A polarizer is placed in the path of the incident beam. The polarization state of transmitted light is determined from the intensity of light measured by the detector. If a polarizer is placed in the path of a reflected beam, it is called analyzer. A polarizer (or analyzer) is generally made from a $CaCO_3$ (calcite) crystal [52].

Compensator introduces a phase delay between perpendicular linear polarizations, leaving the amplitudes unaltered. It is constructed from thin plates of birefringent material or polished crystal rhombus. It is placed in front of a polarizer or analyzer to separate the horizontal and vertical component of a 45° oriented linearly polarized light. An ideal compensator has a retardation of exactly $90°(1/4$ wave). A rotating compensator combined with rotating polarizer can convert unpolarized light into any elliptical polarization [32].

Beam modulator is a stress-operated compensator which works on the principle of photoelasticity [51, 42]. It is a cemented structure of quartz crystal and fused quartz that transfers the resonant electric field-induced periodic stress from quartz crystal to fused quartz and thus, 45° oriented linearly polarized light is separated into the horizontally and vertically polarized light with a variable phase difference depending upon amplitude and frequency of applied voltages and wavelength of incident light [52].

Detector measures the intensity of light reflected from, or transmitted through the sample. Three types of detectors are commonly found in ellipsometry devices: photodiodes, photomultiplier, and diode-arrays tubes. Charge-coupled devices are also used.
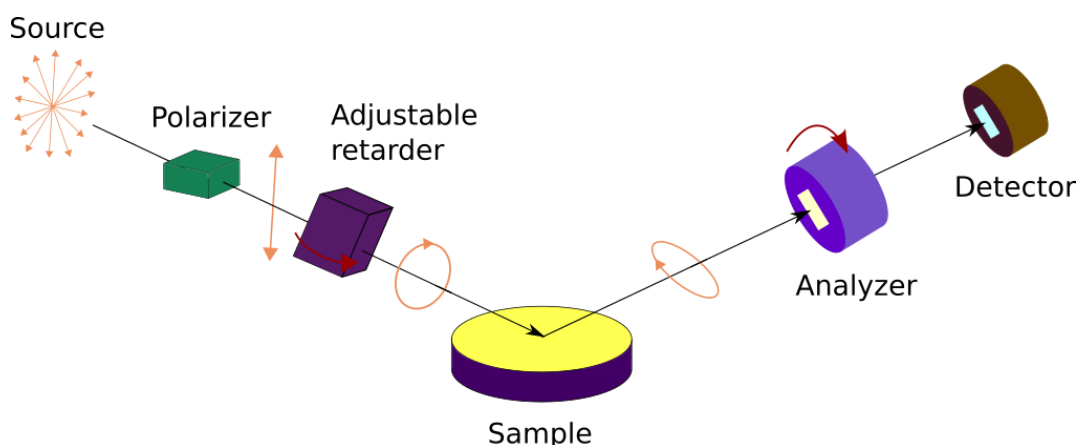
Figure 2. 18. Schematic of rotating analyzer ellipsometer with adjustable retarder.

The measured quantities are ellipsometric functions Ψ and Δ, defined in the previous chapter. Ψ carries information about the change in amplitude and Δ in phase of the reflected

light. It has been shown that the ellipsometric angle Ψ is very sensitive to the bulk refractive index inhomogeneity [53, 54, 55]. At the other hand, Δ may be quite sensitive to the surface inhomogeneity, i.e. surface micro roughness [56]. For these reasons ellipsometry is a valuable technique for determination of refractive index profiles of inhomogeneous layers.

2.3.2.   Optical characterization

Optical characterization starts by creation of samples model where are built in what is known about the substrate, multilayer structure and materials. Substrates refractive index is normally obtained by optical characterisation based on measurements of bare substrate and once determined, they are not changed in the course of optimization. Materials refractive indices and films thicknesses, at the other hand, depend on deposition conditions and post-treatments. For this reason their refractive indices are presented in the model by appropriate dispersion model with parameters that are to be optimized. In this way the sample is represented through a limited set of parameters. The software enables fixing parameters to a given value or to optimise them within some limits. Furthermore, it is possible to establish links between different parameters, allowing for instance imposing the continuity of the volume fraction at the interface of adjacent layers i.e. in corner points.

If necessary, the model is gradually growing in complexity by adding possible surface roughness, mixed materials interlayers or inhomogeneities, for example. Surface roughness is usually treated as a single layer with effective refractive index modelled by EMA, as mixture of air and the last coatings material, where typically volume fractions of constituents are set to 50%, so only thickness is varied. Mixed materials interlayer is presented in a similar way, as mixture of adjacent layers materials. The other possibility is to define it as a layer with its own dispersion model parameters. Inhomogeneity in a layer (i.e. layer with gradient of refractive index) is typically modelled by division into a number of sublayers with the same thickness and constant refractive indices. Their refractive index parameters are related by polynomial or exponent function, whether they are defined by dispersion models parameters or by volume fractions of constituting materials. Finally, gradient index can be modelled as a set of independent layers as well, but there are more free parameters in this way.

In this sense one has to keep in mind that the new parameters in the course of optical characterization should be introduced gradually and only in the case they significantly improve the fit quality. Only then is reasonable to expect that the obtained refractive index profiles and other obtained parameters are reliable.

2.3.3. Design of multilayer systems

Same as optical characterization, design starts with a modelling: defining substrate, thin film materials and their sequence in multilayer, together with the corresponding initial thicknesses. Optical properties of the substrate and materials should be known in advance, so they are either taken from materials databases or determined by optical characterization.

The initial model depends on the type of the desired optical device, i.e. if it is mirror, antireflective coating, beam splitter or something else. There are simple rules (quarte-rwave stack for mirrors, decrease of refractive index towards surface for antireflective purposes) or recipe giving initial design [57, 58, 59]. Finally, target is defined according to the requirements regarding values of R or T, colour coordinates, electric field distribution for specific wavelengths, angles or interfaces. Variable parameters in design are typically layers thicknesses and in some cases number of layers if introduction of new layers is enabled. One has to keep in mind that higher number of layers increases the possibility for deposition errors and multilayer failure due to the accumulated stress in coatings and therefore is important to keep the design as simple as possible.

2.4. Materials

In this research were used different materials for substrates, for dielectric thin films and for metal thin films. In this chapter will be explained what are the main characteristics of glass and its types and thin film properties of the applied dielectrics and metals.

2.4.1. Glass

Glass is a non-crystalline material obtained by rapid cooling from a melt. In the scope of this work, silica oxide glasses were used.

The ideal case of silica matrix (therefore silica is called glass former) is crystalline quartz where silica molecules are bonded to each other by bridging oxygen bonds (BO), forming tetrahedra. Fused silica has non-crystalline silica matrix containing significant concentration of non-bridging oxygen bonds (NBO). These bonds are negative and in conventional glasses they are neutralized by alkali or alkali earth ions that are nesting in NBO vicinity (Figure 2. *19*) [60]. The content of alkali and alkali earths may be as high as 30%. Different kinds of alkali and alkali earths, called glass modifiers, are added to the glass melt to modify its properties, such as viscosity, brittleness, refractive index, etc.
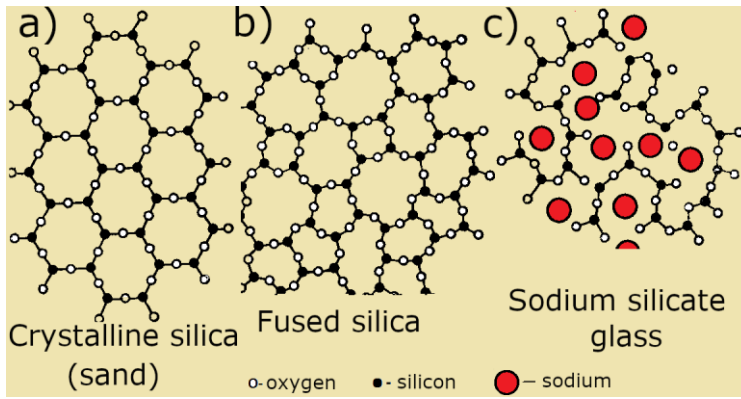
Figure 2. 19. Structure of quartz, fused silica and glass [60]

Cooling may be made by simple cooling of melt in bulk, after which glass is cut and polished from the cold piece, or by pouring the melt onto liquid Sn, after which glass sheets are obtained. The later one is called float glass. Optical glasses are made from bulk of controlled composition, cooled with controlled conditions and cut and polished to satisfy standards for optical applications.

Softening temperature at which glass surface starts getting waviness is around 500 ^{o}C. For this reason is advisable to limit temperature treatments of the glass samples intended for optical measurements to 500 ^{o}C.

The most common is soda-lime glass (SL) that is used for windows, containers, microscope slides glasses and other objects used in everyday's life. This glass is also the most commonly used for GP. It can be recognized by bluish colour in transmittance. Its typical composition is 73% SiO_2, 13% Na_2O, 4% MgO, 1% K_2O, 7% CaO and 1% Al_2O_3 (all in w%). The rest are impurities.

Borosilicate glasses characteristic is the presence of substantial amount of silica and boric oxide ($B_2O_3 > 8\%$) that is also glass former. One of such glasses is BK7 [61, 62, 63].

KF9 glass is specific because it is free of alkali earths and instead contains high quantity of sodium [64].

Refractive indices at 550 nm of these glasses are close to 1.52. Absorption appears around 400-390 nm and increases towards UV. Also, these glasses are opaque in infra red (IR) region above 2700 nm. [63, 65].

These three kinds of glass were chosen thanks to the difference in their alkali and earth alkali composition. SL glass has the most complex composition as it involves the highest

number of cation species. Besides Na and K, there are Ca and Mg that contribute to refractive index profile upon poling. BK7 is in this sense simpler system since it is free from alkali earths, except low content of Ba. Due to the lower content of Na and K, compared with the other two glasses, it is expected weaker modification of poled BK7 refractive index and lower EFAD effectiveness (lower capacity to accommodate metal ions). KF9 has only two cation species: Na and K, but in significant amount. Therefore, it is expected that this glass should have simple refractive index profile upon poling and that metal dissolution should be the most effective.

2.4.2. Thin film materials

The most typically used dielectric materials for optical multilayer systems deposited by EBE are SiO_2 and TiO_2. They are also well known in our Laboratory and therefore were the first choice for the samples studied in this research.

MIFs have interesting optical properties due to their LSPR and therefore allow more possibilities in design than compact metal films. Ag and Au were chosen as their NPs present plasmonic properties in visible part of spectrum, their MIFs have high percolation threshold enabling obtaining of intense LSPR and both of these metals are environmentally stable. It is also important that combination of these two metals is interesting because Au requires significantly stronger conditions to dissolve than Ag. Although Al and Cu MIFs do not have such good properties as Ag and Au, they were chosen as alternative since EFAD of Au requires strong conditions (in other words, EFAD is difficult, or less efficient).

Dielectrics

SiO_2 is common low index material (n(500 nm) = 1.45-1.5). It has good adhesion and makes hard, mechanically resistant layers. It is used for the applications in ultra violet (UV) and visible range, i.e. 250-1100 nm. Films are amorphous, having compressive stress and may contain pores that depend on deposition technique and conditions. SiO_2 films crystallize after treatment above 1100 ^{o}C. When deposited by EBE, the amount deposited onto monitor quartz crystal does not have the expected reproducible ratio to that received at other positions in the chamber. This is explained by erratic sublimation of the material in both, granular and disc shape [58]. This is in the same time the reason why it is difficult to obtain stable rate of deposition.

TiO$_2$ has high refractive index (n(500 nm) = 1.9-2.6). Refractive index varies a lot depending on deposition conditions, specifically on pressure and deposition rate. TiO$_2$ has to be deposited in reactive oxygen atmosphere to prevent reduction and formation of sub-oxides that contribute to the undesirable absorption in the optical range. If such films are obtained, annealing in air above 200 ^{o}C will improve layers stoichiometry and absorption reduction. Sub-oxide free films start to absorb below 400 nm that makes TiO$_2$ inappropriate for UV range. Films have good mechanical properties and tensile stress that makes it perfect in combination with SiO$_2$, compensating stress to each other. This allows obtaining multilayers of high number of layers yet with excellent durability and stability. The films are typically crystalline with rutile or anatase phase, or their mixture [58].

Metals

Ag continuous film has characteristic neutral reflection in visible range and it is favourable metal for mirrors. If compact layer is deposited onto heated substrate, crystallites will form on the film and reflectance will be deteriorated. LSPR position of Ag MIF embedded in SiO$_2$ matrix is roughly between 550 and 450 nm, depending on the substrate temperature and material quantity [66]. Percolation threshold is around 100 Å for films deposited at room temperature and compact films are obtained for more than 200 Å [67].

Compact Au films are yellowish in reflectance witnessing their high efficiency as mirrors for IR region. Position of Au MIF embedded in SiO$_2$ matrix is shifted towards red, comparing with Ag MIF: roughly between 580 and 800 nm, again depending on the substrate temperature and material quantity [68]. Percolation threshold is 70-120 Å for deposition on room temperature (RT) substrates and 330-500 Å for deposition on substrates pre-heated to 230°C [69].

Al is second favourable material for mirrors since it has similar optical properties of compact film in visible part of spectrum as Ag. Compared to other metals, Al has been only recently considered as a plasmonic material [70]. Al nanoparticles display a LSPR in the ultraviolet part of the spectra, however by modifying the shape and size the resonance can be shifted to the visible range [71]. Al wets dielectric surfaces much better than other metals and therefore the percolation threshold is very small and the fabrication of nanoparticle films usually requires pre-deposition surface modification procedures [72]. Overall, the optical properties of Al MIFs display a broad LSPR due to the strong interparticle coupling and to the presence of interband transitions in the infrared part of the spectra [73].

Cu compact film has reddish reflectance. According to its measured dielectric function, copper is potentially a good plasmonic material, but it easily oxides in normal atmospheric conditions [74]. LSPR in oxide-free nanoparticles shows performance comparable to that of Au [75]. Coating of Cu with thin dielectric layers has been shown to significantly enlarge the chemical stability and hence the plasmonic response of Cu nanoparticles [76]. Optical properties of Cu MIFs can be broadly modified by changing the deposition conditions, but unprotected films display a progressive deterioration of LSPR properties [77]. Cu has better wetting properties than Ag or Au [78] and therefore the formation of MIF requires higher substrate temperature.

2.5. Glass poling and EFAD

GP and EFAD are solid state ion exchange processes during which ions contained in the glass matrix and/or thin metal film are drifted towards the cathode under the influence of electric field and moderately elevated temperature. Temperatures are in most cases in the 200-500 ℃ range, and voltages in most cases range from 300 to 1200 V. The two processes share a lot of similarities. The major difference stems from the type of sample. Glass poling takes place in glass slide and EFAD on sample containing metal films or particles.

2.5.1. Glass poling

GP is performed on a glass slide at moderately elevated temperatures and under the influence of electric field [79]. Positive alkali and earth alkali ions drift toward the cathode during the process thus changing the concentration of alkalis in subanodic region of soda-lime glasses, which results in formation of permanently depleted region typically at the depth of several hundred nanometers [80] (*Figure 2. 20*). Depletion of positive ions at anodic side and their accumulation at some depth within the surface induce the formation of an internal electric field [81]. Penetration of hydronium ions (H_3O^+) from atmosphere into the subanodic region of the glass during poling, to compensate the lack of positive charge, influences spatial distribution of ions in the poled glass region [82].
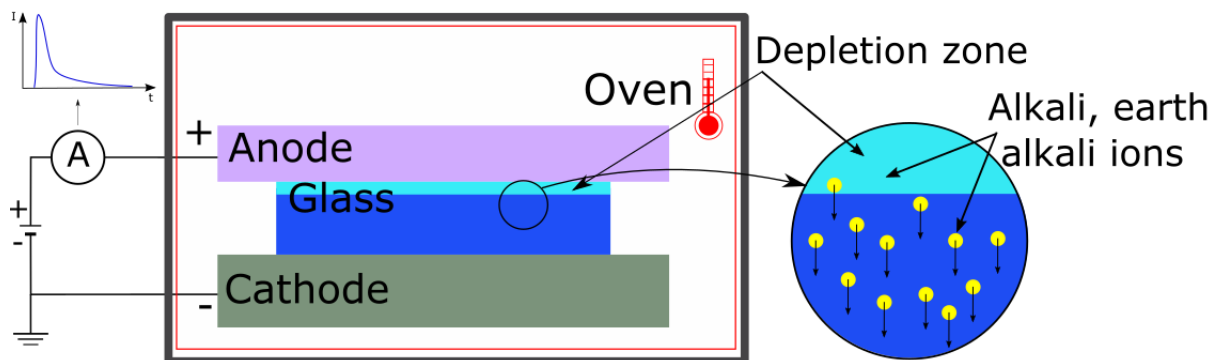
Figure 2. 20. Schematic presentation of GP setup and process.

There are three GP setups: i) blocking, or closed anode, in which external charge carriers cannot penetrate the anode-sample interface, ii) non-blocking, or opened anode, in which charge carriers from atmosphere can freely penetrate into the system and compensate excessive negative charge [79, 83] and iii) semi-blocking, or semi-opened anode that enables $H^+/H3O^+$ diffusion into glass, but not in quantity high enough to compensate the excessive negative charge. In this case alkalis with mobility lower than Na^+, such as Ca^{2+} and Mg^{2+}, are still forced to leave subanodic region. This is contrary to non-blocking corona [84] or non-contact GP [85] when they remain close to the surface.

In case there is a lack of cations, switching of non-bridging oxygen (NBO) bonds to bridging oxygen (BO) bonds [86, 87], and bonding of oxygen ions in interstitial spots takes place to form molecular oxygen. Formation of BO from NBO also leads to restructuring of the silicate network to a "silica-like" structure with higher density and refractive index than the starting NBO containing matrix [88]. It also changes chemical durability of poled glasses [89].

Refractive index profile of poled BK7 [90] and soda-lime glass [80, 91] were studied in literature. It was found that for both glass types refractive index in depleted region has constant value that is lower than the bulk one. This is justified with absence of alkalis in this region.

Peak in refractive index profile next to the bulk region of SL was reported [80], possibly originating from accumulation of Ca and Mg. The peak was confirmed in another study [91] where it was stated that Ca ions accumulation is the reason for the increase of refractive index. In another study, however, it was introduced a dip of refractive index between surface and bulk of poled SL glass [92].

Finally, GP is applied to induce second-order nonlinear optical properties [93, 94], Pockels electro-optic effects [95,96], for fabrication of waveguides [97], for imprinting diffractive gratings on glass surface [98, 99, 100, 101], and preparation of surface for lithography and etching [102, 103, 89].

2.5.2. Electric field assisted dissolution

The experimental set up for EFAD is the same as for GP. EFAD is applicable to the system involving metal on/within glass or embedded in dielectric layers on glass [104, 13, 16].

EFAD occurs simultaneously with GP: electric field tears positive metal ions from bulk metal, and metal ions replace positive charge in alkali depleted subanodic region, depending on the relative mobility of metal to alkali ions (Figure 2. *21*). EFAD is a more complex case as it involves metal on the glass surface or within glass and is therefore less studied. EFAD changes composition of soda-lime glasses in subanodic region by doping it with metal ions [105, 104]. EFAD results in complete dissolution of MIFs [106, 107] or compact metal layers [108] if the process lasts long enough thus strongly changing systems optical properties. The same applies to metal nanoparticles embedded in dielectric multilayer system [109, 19]. EFAD followed by annealing results in formation of metal nanoparticles in glass matrix by reduction and clustering of metal ions [14].
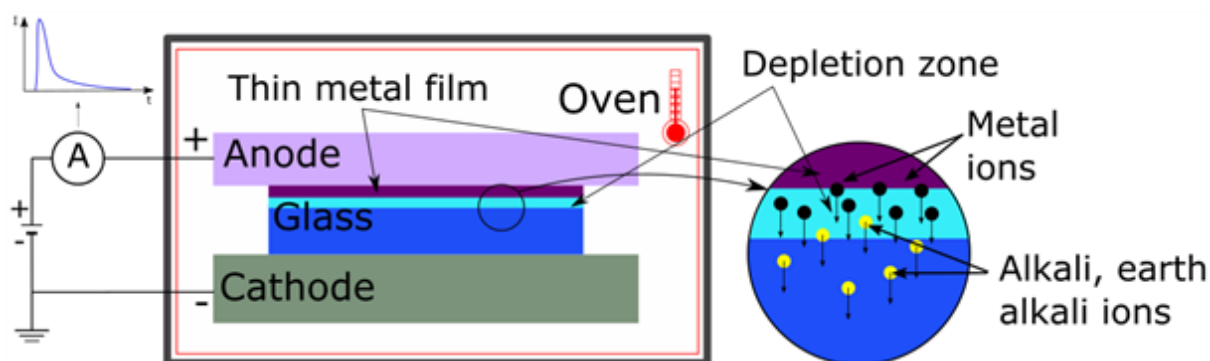
Figure 2. 21. Schematic presentation of EFAD setup and process.

The most often is studied EFAD of Ag [110, 105, 111, 108]. Also EFAD of Au [112], Co [113], Cr [104, 114https://doi.org/10.1016/j.jnoncrysol.2010.12.050], Er [115] and Cu [116, 117, 118, 119, 120] was made. Thus is demonstrated that multivalent metals can be dissolved as well, although no so easily as monovalent.

Simultaneous EFAD of Ag and Co has been realized resulting in of co-doping of glass with both metals [113, 121].

Micro-structuring of MD MLS was demonstrated in a system consisting of multiple Ag MIF embedded in SiO_2 and 3D array was obtained [18]. No results on patterning bimetal system have been reported so far.

2.5.3. Dynamics of glass poling and electric field assisted dissolution

Theoretical background of glass poling process was explored first by von Hippel in alkali-halide crystals [122] and by several groups in silicate glasses [123, 83, 124, 125, 126, 127]. Modelling was done with up to two intrinsic species.

Analytical model applicable for simulation of non-blocking anode was developed [128] for EFAD with constant voltage. Limitation of the model is assumption that glass has only one native mobile ion specie. This caused that lower mobility ions (K^+, Ca^{2+}, Mg^{2+} and others) pile-up regions could not have been modelled even though they were experimentally observed.

Study of drift and diffusion of a single ion specie drift-diffusing into glass containing only one mobile ion specie was based on the solution of the drift-diffusion equation with assumed constant ion injection rate, j, rather than a defined voltage boundary condition but did include space charge effects [124].

Modelling of GP with a non-blocking anode and a single alkali specie has been performed numerically with the use of ion drift-diffusion equations combined with Poisson's equation [125]. The ionic mobilities of SL glass obtained in experiments [82] were used in simulations in another study, where modelling was extended to two ion species [83], were $\mathbf{\mu(Na)} = 7 \cdot 10^{-16} m^2(Vs)^{-1}$, $\mathbf{\mu(H)} = 2 \cdot 10^{-20} m^2(Vs)^{-1}$ and $\mathbf{\mu(Ca)} = 1 \cdot 10^{-21} m^2(Vs)^{-1}$ at 150 °C. Duration of experiment and simulation was 540 s, and voltage applied was 1.7 kV.

Mobility values of $\mathbf{\mu(Na)} = 1.3 \cdot 10^{-15} m^2(Vs)^{-1}$, $\mathbf{\mu(H)} = 1.3 \cdot 10^{-19} m^2(Vs)^{-1}$ and $\mathbf{\mu(K)} = 1.625 \cdot 10^{-17} m^2(Vs)^{-1}$ at 300 °C were used in numerical and analytical simulations of poling of SL and borosilicate glasses [126]. Numerical solutions of the ion drift-diffusion equations and Poisson's equations obtained from [83] were compared to analytical solutions in order to confirm accuracy of the ionic concentration profiles [126].

Numerical analysis of GP in another study [86] considered oxygen ion drift motion in a developed depletion region.

Numerical model of sequential EFAD of two ion species into glass was performed [129]. Two coupled nonlinear drift-diffusion equations were derived for the ion concentration distributions. The two external ion species each have a lower mobility than the indigenous sodium ions in the glass.

Numerical simulations of EFAD in a SiO_2/Ag systems were performed. Glass contained only one native specie: Na. The simulations were performed using drift-diffusion equations in combination with Poisson's equation to investigate Ag^+ ion implantation in SiO_2 layer [19]. The model was later extended to simulations of electric current of glasses coated with Ag and one dielectric layer (SiO_2, TiO_2 or Al_2O_3) during EFAD [20].

2.6. Additional characterization techniques

Optical properties of the samples studied in this research are the most important for their performance and they can be precisely determined from ellipsometric measurements. However, their optical properties are closely related with composition of the multilayer and substrate. Therefore it was important to make depth composition analysis, compare with refractive index profile and establish relations among the two. Secondary ion mass spectrometry was used for this purpose.

As mentioned before, using patterned anode for GP or EFAD, selective composition changes are obtained in the sample, resulting in copy of anode pattern. One has to keep in mind that the obtained pattern is not only in surface plane since GP induces restructurization of glass matrix followed by appearance of surface relief. For this reason, the surface of the micro-structured filter inevitably has depth relief as well. The relief does not have to be disadvantage for the application, but merely should be taken into account. For characterization of the surface profile of the micro-structured filter was used profilometry.

2.6.1. Secondary ion mass spectrometry

Secondary ion mass spectrometry (SIMS) is used to analyze compositional profile of bulk samples. SIMS is based on detection of charged particles (secondary ions) ejected from a sample surface bombarded by a primary beam of heavy particles (primary ions).

The ejection is based on sputtering, a process in which energetic ions, atoms or molecules (with energies ≥ 0.1 keV), impinge on target. Particles of the sample are ejected from less than 1 nm depth, providing information about the target surface (Figure 2. *22*) [130https://doi.org/10.1016/0042-207X(94)90113-9]. As the sputtering continues,

increasingly deeper crater develops, revealing information about target bulk. In the secondary ion column the secondary ions are collected, filtered, and focused onto the detector. The column contains a) lenses and deflectors used to collect and transport secondary ions, b) energy filter used to limit the energy spread c) mass filter used to limit the mass to charge ratio of secondary ions and d) mass spectrometry detector measuring mass to charge ratio of charged particles and, in some configurations, spatial resolution. It is possible to retrieve mass spectrum, spatial image or depth profile from the measurements (*Figure 2. 23*) [131].
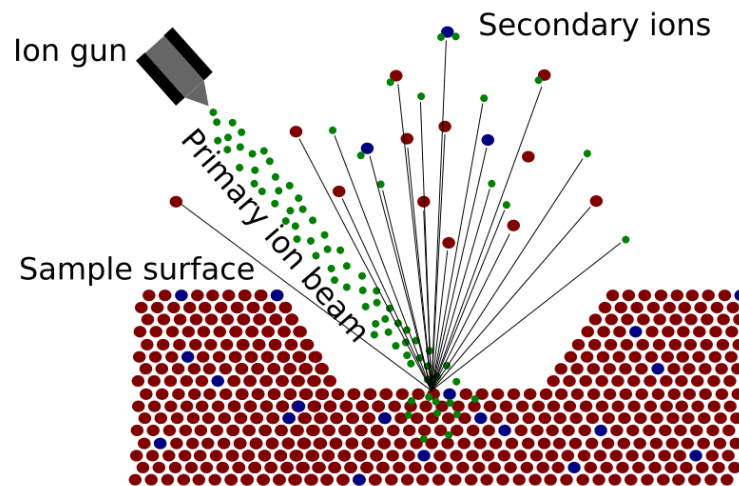
Figure 2. 22. Sputtering of secondary ions by primary ion beam impinging at sample surface.
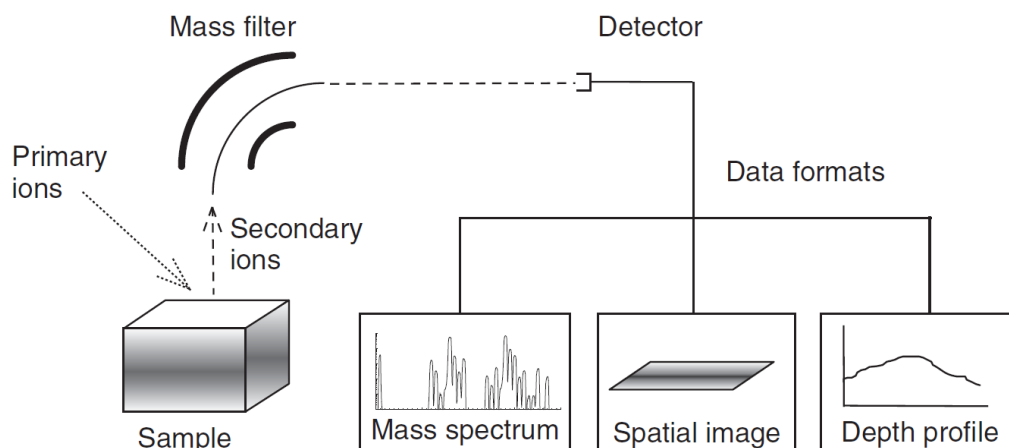
Figure 2. 23. Schematic presentation of SIMS.

Issues regarding the application of SIMS to GP samples

Si concentration profile of poled glass obtained by SIMS typically shows higher Si intensity in depleted region next to the surface. Assuming that Si concentration is constant in poled

glass due to the fact that Si is not expected to move during poling as it is glass former, deviations from constant Si composition value were attributed to the changes of sputtering rate by some authors, proposing also how to make corrections of the data[132]. Their conclusion has been subject discussion since the change of Si signal in poled glass may be a consequence of matrix reorganization (and thus densification) within depletion region to accommodate charge disbalance [133]. Composition measurements using glow discharge – optical emission spectroscopy technique (GD-OES), in which the measured intensity of compound is directly correlated to its concentration, confirmed that increase of Si signal at the beginning of depleted region reflects real increase of its concentration [85]. Although the etching rate of the beam may slightly vary in different regions of poled glass, it is not justified to make corrections of its concentration profile, neither to the concentration nor to the depth, without a deeper research on this issue.

2.6.2. Profilometry

A profilometer is used to measure the surface profile. Optical profilometers use optical beam to probe the surface and hence are making non-contact measurements that are preferable for soft materials. Mechanical profilometers utilize stylus that makes physical contact with the tested surface. The profilometer consists of a stylus with a small tip, a gauge or transducer and a processor. As the stylus moves up and down along the surface, it records the heights and valleys encountered along the scan path. The transducer converts this movement into a signal that is fed to a processor, which converts the data into a graphical presentation of the profile with height values.

The tip can be as small as 20 nm in diameter enabling high resolution. Vertical resolution can also be in nm range. It is a direct measurement technique with no modelling required. Method is not sensitive to the surface reflectance or colour, which can influence the measurements with optical profilometers.

Mechanical profilometers have the disadvantage that the tip of the stylus traverses along the surface and hence is appropriate only ford hard surfaces [134]. The samples studied in this research have surfaces hard enough to be subjected to mechanical profilometer measurements.

3. EXPERIMENTAL

In this chapter will be described steps of samples preparation, how the filter was designed and its performance theoretically tested to the changes upon GP/EFAD, which samples were prepared and studied, measurements of their properties, how was performed data analysis and how numerical simulations were done.

3.1. Sample preparation

Sample preparation was made in different steps. Prior to any treatment, substrates for samples were cut to the appropriate size if necessary (soda-lime microscope slide glasses) and all substrates were cleaned. After this, some substrates were subject to glass poling. Thin films were deposited by electron beam evaporation to the other substrates. Deposition was followed by annealing or electric field assisted dissolution, using plain, macro-structured or micro-structured electrode. The samples back side was cleaned before transmittance measurements to remove sodium contamination upon GP/EFAD.

3.1.1. Substrates

Three different types of glass were used as substrates for GP and EFAD samples: BK7, KF9 and soda lime. BK7 and KF9 are Schott glasses. Soda-lime glass that was used is Menzel Glass microscope slides (Thermo Scientific). This kind of glass will also be referred to as Menzel.

The composition of KF9 and BK7 glass was determined by particle induced X-ray emission (PIXE) and time-of-flight elastic recoil detection analysis (TOF-ERDA) performed at Ruđer Bošković Institute. SL glass composition in weight percent (wt%) is available from the supplier [135]. KF9, BK7 and SL glass composition data are given in Table 3. 1. and in at% in Table 3. 2.

Table 3. 1. Glass composition given in molecular weight percent.

	wt% SiO_2	wt% Na_2O	wt% CaO	wt% MgO	wt% Al_2O_3	wt% K_2O	wt% TiO_2	wt% B_2O_3	wt% BaO
KF9	70.6 ±2.9	22.3 ±1.4	-	-	-	1.3 ±0.1	6.4 ±0.5	-	-
BK7	71.7	7.9	-	-	-	10.8	-	10.9	1.14

	±3.0	±0.5				±0.7		±0.7	±0.08
SL	72.2	14.3	6.4	4.3	1.2	1.2	-	-	-

Table 3. 2. Glass composition given in at%.

	at% Si	at% O	at% Na	at% Ca	at% Mg	at% Al	at% K	at% Ti	at% B	at% Ba
KF9	24 ±1	57 ±3	14.7 ±0.9	-	-	-	0.57 ±0.06	1.2 ±0.1	-	-
BK7	24 ±1	59 ±3	5.1 ±0.3	-	-		4.6 ±0.3	-	6.3 ±0.4	0.15±0 .01
SL	24.7	60	9.5	2.4	2.2	0.6	0.5	-	-	-

BK7 was cut and both side polished to plates 25 mm in diameter and 1 mm thickness (Praezisions Glas & Optik GmbH). KF9 was cut and both sides polished to square slides 15 x 15 mm², also 1 mm thick (Standa). Substrates of both glasses have surface flatness better than λ/4 at 633 nm and surface parallelism equal or better than 3 arc min. SL microscope slides (thickness 1mm) were cut with diamond knife to the size of approximately 25 mmx15 mm.

Si wafer chunks (Si-Mat, type P/boron, orientation <100>, resistivity 10-20 ohmcm, thickness 381 +/- 25 μm, flats 2 SEMI, single side polished, native SiO_2 thickness 2 nm) were used as control substrates for deposition of the filter.

3.1.2. Cleaning

Both sides of all the glass substrates and polished surfaces of Si wafer chunks were cleaned by cotton wool soaked with ethanol and wiped with cotton cloth. Prior to this, SL glass was additionally cleaned by cotton wool soaked with acetone and wiped with cotton cloth. This step was necessary in order to remove the wax that is typically coated over microscope slides to reduce possible scratching of the surface by dust particles between the slides. Upon cleaning with cloth, cotton dust was blown from the substrates by dry nitrogen using a pressure nozzle. The sodium compounds accumulated at the back side of the substrates after GP and EFAD were cleaned in the same way (ethanol and cotton) not to affect transmittance measurements.

3.1.3. Electrodes for glass poling and electric field assisted dissolution

The substrates were placed between electrodes in GP and EFAD set-up. The cathode was "below" the substrate, facing the back side of the sample. It was a smooth, flat aluminium plate, to enable homogeneous electrical contact across the substrate, with thickness of 5 mm to prevent deformation of the electrode.

One side Cr coated BK7 glass plates 4 mm thick were used as anode. Cr coating thickness was approximately 500 nm. Three types of anodes were used: plain one, macro-structured and micro-structured. The plain electrode has compact Cr coating over the whole surface. One part of the macro-structured electrode substrate was masked prior to Cr deposition, so after coating a bare glass window was obtained in the conductive Cr layer. In this way it was possible to carry out locally selective GP: no electrical contact beneath the window means no poling and the properties in this part of the sample remain unchanged (Figure 3. 1). Micro-structured anode consists of three parts: macroscopic compact Cr layer, macroscopic bare glass area and the arc shaped pattern consisting of 17 µm wide Cr ribs separated by 18 µm wide grooves with bare glass bottoms. The length of lines is 4 mm. The pattern was home-made by photolithography. The contact to the anode Cr layer was realized by placing the anode in power supply connected metal ring that was touching the coating.
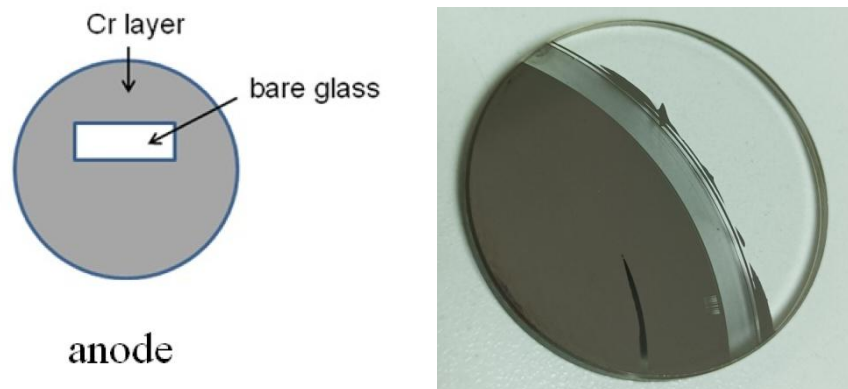
Figure 3. 1. Scheme of macro-structured (left) and photo of micro-structured anode (right).

3.1.4. Glass poling

Glass poling was made in semi blocking conditions. The substrate was sandwiched between the electrodes and fastened by screw in the holder. Both, anode and cathode, were bigger than the substrates. The free space between the electrodes surfaces was filled with mica sheets in order to prevent possible short-cuts or sparks due to the applied high voltage (Figure 3. 2).
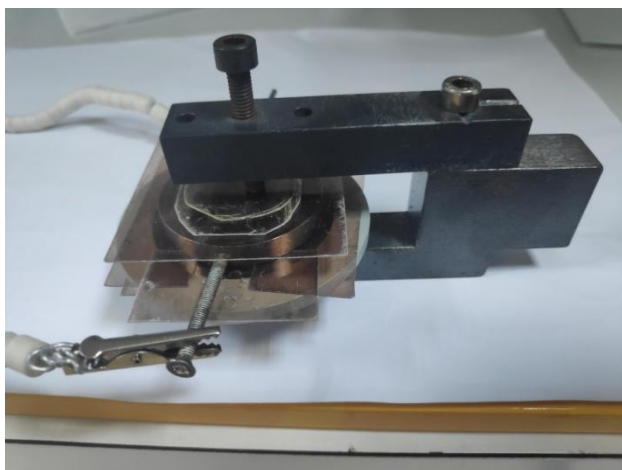
Figure 3. 2 Photo of the sample holder set-up.

The holder with sample was placed in the Lindberg Blue M Thermo Scientific furnace. The electrodes were connected in the circuit consisting of Keithley Instruments 2290-5 voltage source, Agilent Technologies 34410A multimeter and computer. Additionally, KF9 sample was poled in Elektrosanitarij LPT60-500 oven in vacuum ($4 \cdot 10^{-4}$ hPa).

The applied GP conditions were 300 °C, 500 V, 2 h (in the following text the conditions will be abbreviated to $x/y/z$, where x will be temperature in °C, y voltage in V and z time in hours, if not differently specified, for example 300/500/2). The time taken was so long for the sake of better repeatability.

Each sample passed preheating period of 40 min in order to reach a stable final temperature of 300 °C before poling started. When the preheating period was completed, the power supply was turned on and voltage was increased by 50 V increments to obtain the final voltage of 500 V. Time for voltage increasing was typically taking between 4 and 6 minutes. Time measurements started once the final voltage was achieved. When the time for GP was completed, the power supply and oven were turned off and the oven lid immediately opened. Thus the samples were naturally cooled down to the room temperature.

3.1.5. Thin film deposition

The coatings were deposited by electron beam evaporation using modified Varian 3117 deposition plant. The films mass thicknesses were controlled by Sloan quartz crystal monitor, measuring the change in frequency of a quartz crystal due to the change of material mass deposited on it. Mass thickness of the layers (the value that is read out at the monitor) will be

given in Å in this work and the real thickness (obtained from optical characterization) will be given in nm.

Base pressure during deposition was $9 \cdot 10^{-6}$ Torr. The plant is equipped with quartz heaters and planetarium of rotating calotte that enables better thickness uniformity of the layers across the substrates surface (Figure 3. 3.).

Figure 3. 3. Photo of the evaporation plant.

SiO_2 films were prepared from evaporation of SiO_2 granulate (Balzers, 99.9% SiO_2, grains 1.6-5 mm). TiO_2 films were prepared from evaporation of Ti_2O_3 tablets (Balzers, 99.5 % Ti_2O_3). Deposition rate for both dielectrics was approximately 10 Å/s (the rate was manually controlled). These materials were deposited onto substrates pre-heated to 230 ^{o}C in order to increase adhesion and decrease stress in the coatings. For deposition of TiO_2 it was added oxygen into the chamber to avoid formation of a sub-oxide, TiO_x, $x<2$, and thus unwanted absorptance in blue and violet part of spectrum. The oxygen partial pressure was $9 \cdot 10^{-5}$ Torr. Crystallinity of thick SiO_2 and TiO_2 films (thickness couple of hundreds nanometers) prepared in this evaporator under the same conditions was under detection limit of X-ray diffraction.

Chromium coatings for anodes were prepared from Cr granulate (Balzers, 99.9% Cr, grains 0.7-1.5 mm). Coatings thickness was approximately 500 nm, as mentioned before. The material was deposited onto the pre-heated substrates as well with rate of deposition

approximately 100 Å/s. Such high deposition rate is preferred for this metal as it is very easily gathering remaining oxygen from the chamber.

Gold and silver for MIFs were prepared from Au shot (< 4mm pieces) and Ag pellets (1/8" diameter x 1.8" long) (both Balzers, 99.99% pure). Rate of deposition for these two metals was 1 Å/s. They were deposited onto pre-heated substrates in order to enhance formation of metal nanoparticles.

3.1.6. Filter design

As mentioned in Introduction, the goal is to apply EFAD to a multilayer system containing coatings with two metals that have different dynamics of dissolution. One metal would be dissolved in the first EFAD step (EFAD1) and another in the second (EFAD2). Application of micro-structured electrode would enable selective dissolution in each step, which would result in microarray filter with three areas of distinctive optical properties: i) intact area where there was no electric contact with electrode in any step and both metal layers would be present (no EFAD), ii) area where contact was realized only in the first step (EFAD1) so only the metal layer more resistant to EFAD would be present and iii) area where the contact was realized only in the second (EFAD2) step containing no metal and area treated in both steps (EFAD12) that also contains no metal.
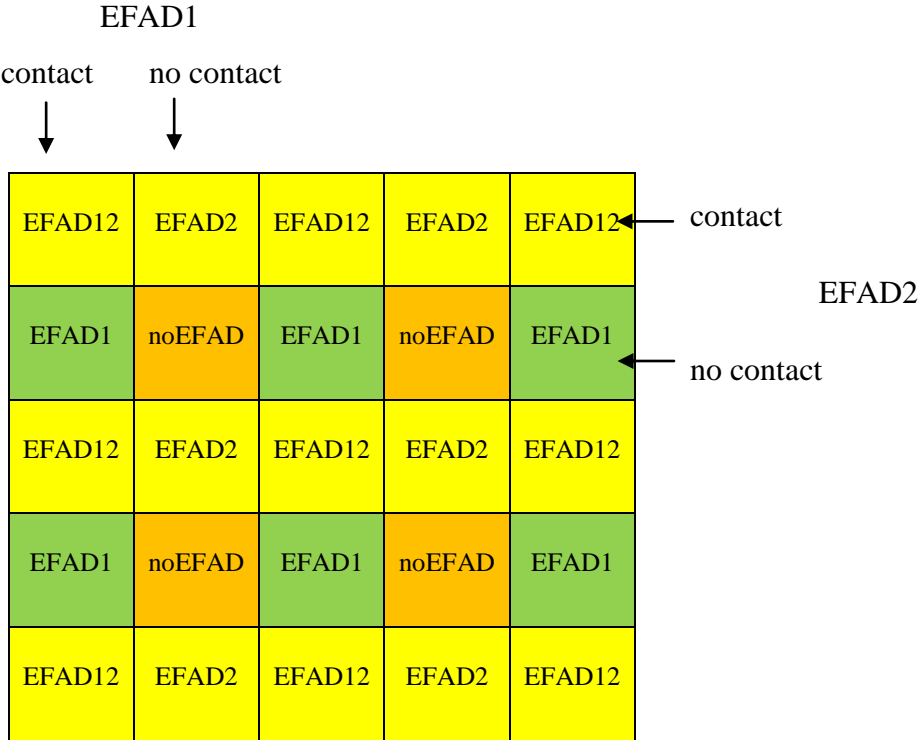
Figure 3. 4. Schematic presentation of the expected microarray (microfilter).

47

A system with high R or T in relatively narrow spectral region for all the mentioned cases (presence of both, one or none metal) is the most desirable as demonstrator. The changes of glass optical properties due to GP or doping with metal ions during EFAD may significantly modify optical properties of the multilayer. It was decided to design the filter operating in reflection in order to reduce contribution of light intensity reaching the substrate and consequently minimize the effect of the substrates modified refractive index.

The filter was assembled in TFCalc software, specialized for design of thin film multilayer systems. Simulations of design R, T and colours are made in the same software. The filter has two parts: a pure dielectric quarter wave reflector centred in green (the highest sensitivity of human eye) and MIF/dielectric containing part above it. The reflector is based on constructive interference. The MIF part is combining plasmonic LSPR absorption with interference that is enhancing its contribution.

In order to achieve high reflectance with low number of layers, the used dielectric layers should have as high difference of refractive indices as possible. Therefore, for dielectric part are chosen TiO_2 as material with high refractive index (n(5500 nm) = 2.23) and SiO_2 as material with low refractive index (n(5500 nm) = 1.46). Silver and gold are chosen as metals for MIF part. TFCalc software simulates optical performance of the designed multilayer system (filter) from thicknesses and optical properties of the chosen materials, i.e. their complex refractive indices. There were used standard complex refractive indices of SiO_2 and TiO_2 layers obtained by EBE in our Laboratory.

Since optical properties (i.e. dielectric constants) of nanoparticle films depend on the shape and density of samples of Ag and Au MIF (70 Å and 40Å, respectively) embedded in SiO_2 were deposited at heated substrate (230°C), annealed after deposition at 200°C for 2 h and characterized. The obtained thicknesses and dielectric functions were used for the design.

The filter design is given in Table 3. 3. There are no critically thin dielectric layers and the total number of materials is 4 in 11 layers that is not demanding for deposition. However, Au layer is very thin and it could be difficult to deposit this quantity of material precisely. Besides this, the total thickness of SiO_2 in the system is nearly 700 nm that is relatively high. It can be expected that a hole will be formed at the surface of the material in the crucible, which could change the shape of evaporated material cloud and thus induce errors in thicknesses of last layers.

Table 3. 3. Filter design. The first layer is next to the substrate.

material	thickness/ nm
SIO2	150.00
TIO2	54.09
SIO2	91.63
TIO2	60.00
SIO2	91.63
TIO2	65.00
SIO2	60.00
Ag	13.43
SIO2	260.00
Au	4.00
SIO2	30.00

The performance of the HL part and MIF part are given in Figure 3. 5. The filters optical performance depending on MIF content, at 0° angle of incidence and included back side contribution, is given in Figure 3. 6. Complete filter, with both MIFs, does not have a pronounced peak in reflectance, resulting in pale orange colour. In this system the light that could be reflected in green part is absorbed in MIFs as the beam is passing through them twice. Upon EFAD1 (Ag MIF dissolved), appears relatively narrow peak in green. Finally, after EFAD2 (Au MIF dissolved as well) this peak broadens to the yellow part of spectrum resulting in dominantly yellow colour.
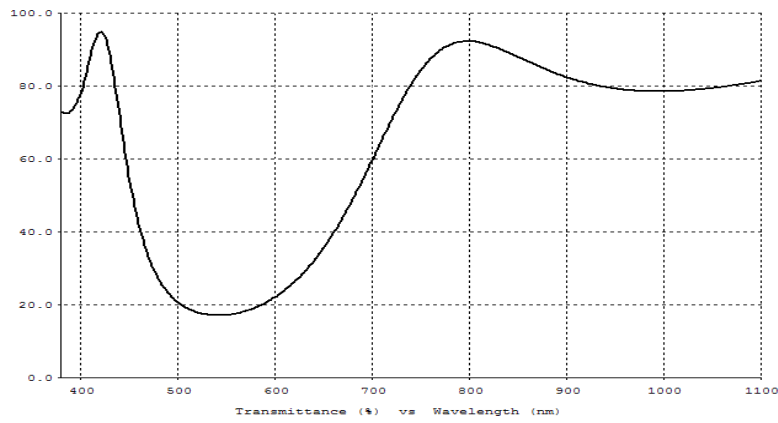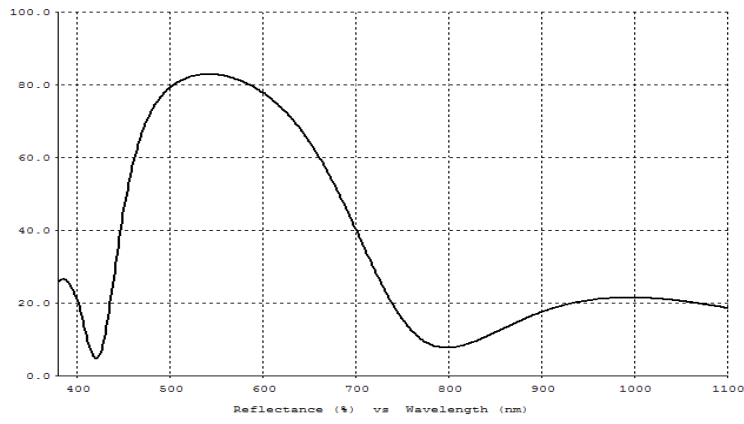
Performance of HL part

	Refl	Trans
Color Standard:	1931 CIE	
Field of View:	2°	
Polarization:	Average	
Reference White:	CIE-C	
Illuminant:	WHITE	
Incident angle (deg): 0.0		

	Refl	Trans
x Coordinate:	0.362	0.280
y Coordinate:	0.408	0.197
Luminosity (%):	79.14	20.86
Dominant (nm):	570	N/A
Complementary (nm):	459	562
Excitation Purity:	0.387	0.427
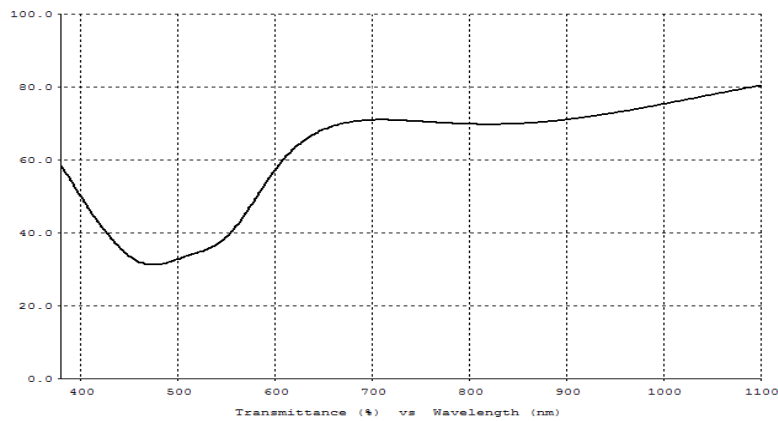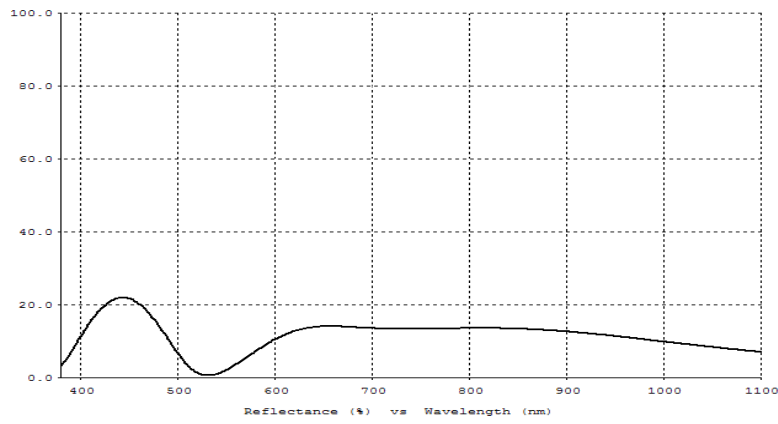
Performance of MIF part

	Refl	Trans
Color Standard:	1931 CIE	
Field of View:	2°	
Polarization:	Average	
Reference White:	CIE-C	
Illuminant:	WHITE	
Incident angle (deg): 0.0		

	Refl	Trans
x Coordinate:	0.307	0.392
y Coordinate:	0.174	0.342
Luminosity (%):	6.20	44.85
Dominant (nm):	N/A	593
Complementary (nm):	552	487
Excitation Purity:	0.570	0.289

Figure 3. 5. Performance of two parts of the filter. Top: HL part, bottom: MIF part.

Reflectance (%) vs Wavelength (nm)

Transmittance (%) vs Wavelength (nm)
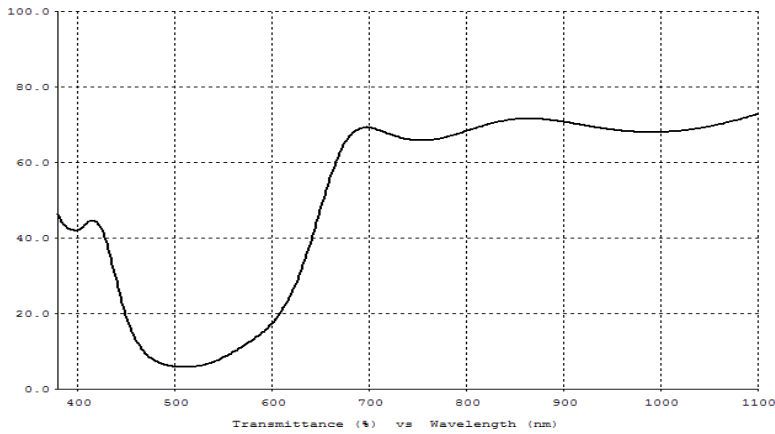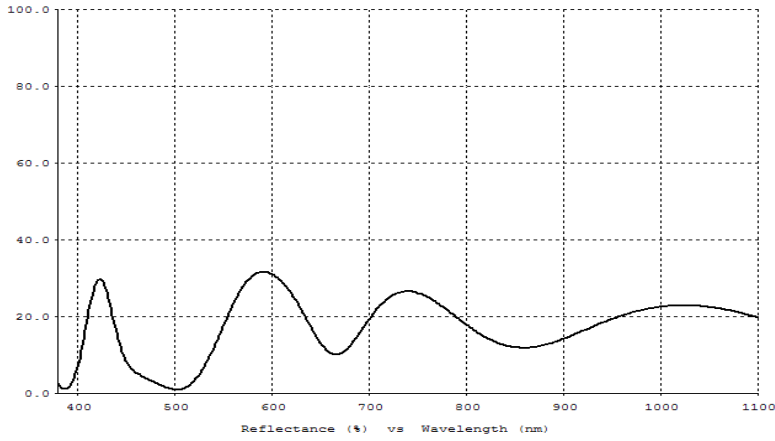
Complete filter

(no EFAD)

```
Color Standard:        1931 CIE
Field of View:         2°
Polarization:          Average
Reference White:       CIE-C
Illuminant:            WHITE
Incident angle (deg): 0.0


                          Refl    Trans
x Coordinate:          0.435   0.381
y Coordinate:          0.348   0.234
Luminosity (%):        18.39   12.94
Dominant (nm):           596     N/A
Complementary (nm):      488     506
Excitation Purity: 0.419   0.464
```


Reflectance (%) vs Wavelength (nm)

Transmittance (%) vs Wavelength (nm)
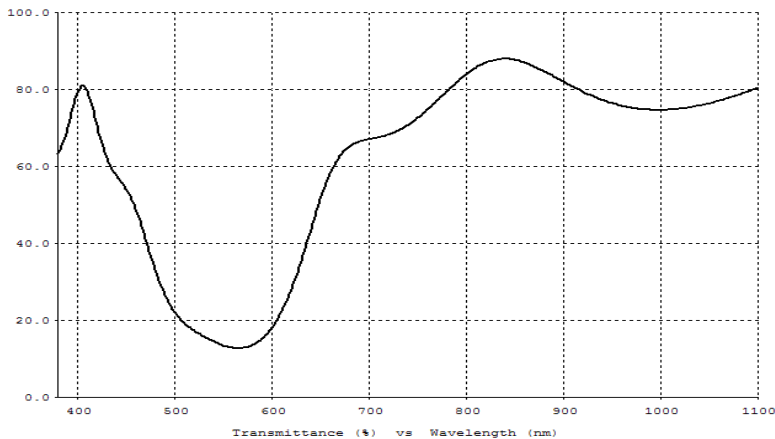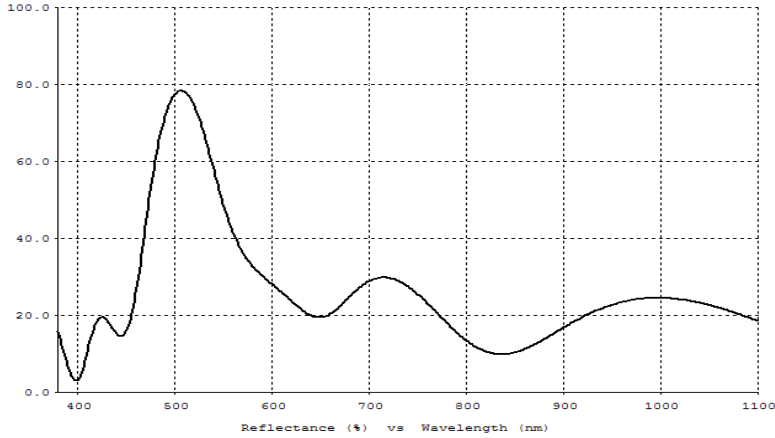
Filter without Ag MIF

(upon EFAD1)

```
Color Standard:        1931 CIE
Field of View:         2°
Polarization:          Average
Reference White:       CIE-C
Illuminant:            WHITE
Incident angle (deg): 0.0


                          Refl    Trans
x Coordinate:          0.285   0.288
y Coordinate:          0.432   0.195
Luminosity (%):        45.95   19.02
Dominant (nm):           538     N/A
Complementary (nm):      N/A     559
Excitation Purity: 0.258   0.448
```

51
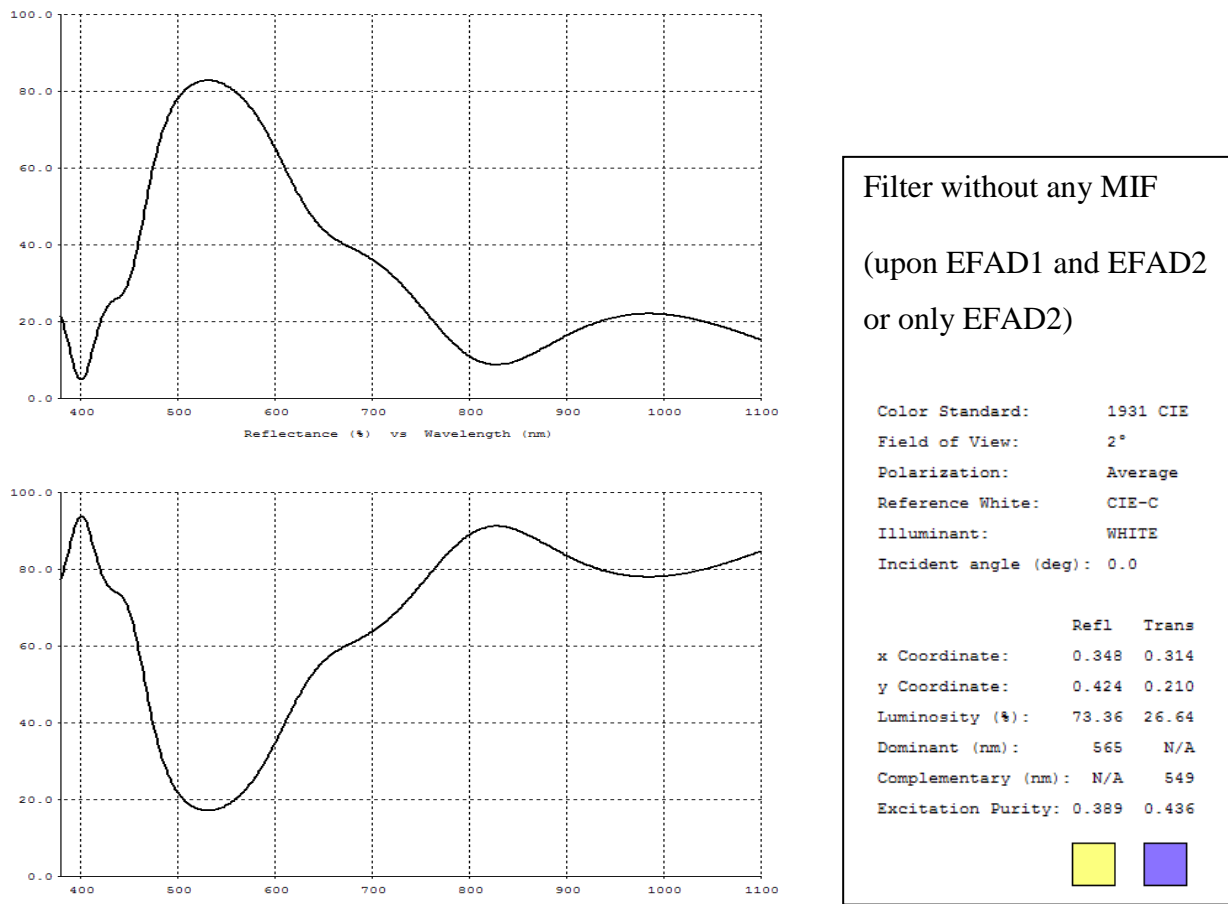
Figure 3. 6. Performance of the filter depending on MIF content: R, T and color.

It was necessary to check in what extent the expected changes in refractive index of the glass and dielectric layers influence the optical properties of the design, i.e. if the design should be refined to compensate them or they can be neglected. Namley, as explained before, the application of EFAD to the filter should result in the absence of one or both MIFs. However, EFAD will also result in modification of the refractive index of the glass substrate and of the dielectric layers due to the drift and diffusion of ions. Moreover, it is assumed that upon EFAD, MIFs collapse and therefore are absent, yet previous works show that it can remain a dielectric layer with pores instead of NPs. The influence of these effects was also studied using the TFCalc software.

3.1.7. Annealing

The samples prepared for experiments studying simultaneous Ag/Au EFAD were annealed at 200 °C for 90 minutes in air atmosphere in the same furnace and pre-heating process that was used for GP and EFAD. This temperature was taken as a bit lower than the one at which MIF

52

were deposited. Annealing at higher temperature would lead to reshaping of metal NPs that could change MIFs optical properties. The annealing time roughly corresponds to the EFAD time for the same serial of experiments, simulating annealing during pre-heating and EFAD process itself. The samples prepared for optical characterization of Ag and Au MIFs, necessary for filter design, were annealed at 200 °C as well, but for 2 hours, that was supposed time for two EFAD steps, including pre-heating.

3.1.8. Electric field assisted dissolution

EFAD set-up and procedures were the same as for GP, only conditions were different and, of course, the substrates that were used were coated with metal-containing films. The conditions were 200/500/2.5-15 min in the case of experiments studying simultaneous EFAD of Ag with Au. Simultaneous EFAD of Ag with Al was done also at 400 V and Ag with Cu also at 700 V, both in order to control the process. These conditions are taken as proper for effective EFAD based the results from a previous study [109]. In the case of macro and micro-structuring EFAD conditions in the first step were 200/500/15 min (EFAD1) and 300/700/1 in the second step (EFAD2). EFAD1 and EFAD2 conditions were experimentally determined as sufficient for complete dissolution of 70 Å of Ag embedded in SiO_2 and 40 Å of Au also embedded in SiO_2, respectively. EFAD of Au at temperatures lower than 200 °C did not result in complete dissolution of the Au MIF.

3.1.9. Macro and micro structuring

Macro and micro-structuring were performed using appropriate electrodes in EFAD1 and EFAD2 processes. Between the two steps the sample was cooled to room temperature, anode removed from the holder and mounted back rotated 90° in the substrates surface plain, so the structure crosses the one obtained upon the first step.

3.2. Samples

As mentioned before, three serials of samples were prepared: GP serial, simultaneous EFAD of two metals serial and filter serial. GP serial was made to help in choosing the most appropriate substrate for the filter regarding the substrates composition and complexity of optical characterization upon treatment. In simultaneous EFAD serial was studied dynamics of dissolution in systems with two metals, as the filter was planned to contain layers of two

53

metals. Filter serial was made for final proof of concept and analysis of filters optical properties.

3.2.1.   GP serial

Since microscopic glass slides are made as float glass by pouring glass melt onto liquid Sn (not from bulk glass by cutting and polishing as BK7 and KF9 substrates), one surface might contain Sn in quantity high enough to modify glass refractive index. For this reason both sides of a virgin SL substrate were checked by ellipsometry [136].

In this serial four different samples were poled. SL, BK7 and KF9 glass substrates were poled under same conditions in air (SL, BK7 and KF9 sample).

The same poling treatment was repeated to a KF9 substrate in vacuum (vacuum KF9 sample). This was done to verify if the results are repeatable also in blocking conditions. The list of samples is given in Table 3. 4.

Table 3. 4. GP serial samples

sample name	GP conditions (^{o}C/V/h)
SL (Menzel)	300/500/2
BK7	300/500/2
KF9	300/500/2
vacuum KF9	300/500/2, in vacuum

3.2.2.   Simultaneous EFAD serial

SL glass was used for substrates in this serial. Ag with Au combination was studied in more details since these metals seemed the most favorable for filter design due to the plasmonic properties, environmental stability and difference in EFAD conditions necessary for effective dissolution of MIF of these metals. However, also combinations of Ag with Al and Ag with Cu were treated.

Single MIFs were deposited in the sequence SiO_2/M/SiO_2 (the first layer of the sequence is next to the glass and the last to the air). The thickness of the first SiO_2 layer is 1958 Å, the second 1305 Å and MIF 90 Å.

Bimetal combinations were deposited in multilayer systems in the sequence $SiO_2/M1/SiO_2/M2/SiO_2$ and $SiO_2/M1/SiO_2/M2/SiO_2$ (M1 stands for one metal and M2 for another metal in the combination). The samples will be referred as M1/M2 or M2/M1, depending which metal is closer to the substrate. The thickness of the metal layers was chosen from previous studies in order to obtain films made of isolated nanoparticles with effective optical response dominated by LSPR. The thickness of Ag was 500 Å, and the thickness of Au, Al and Cu layer was 300 Å. Ag/Au systems were deposited also with thinner metal layers: Ag 240 Å and Au 90 Å. Therefore, the Ag/Au samples will be referred as thinner and thicker, depending if they contain thinner or thicker metal layers, respectively. The thickness of each SiO_2 layer was 1200 Å, except for thinner Ag/Au sample where the last layer is 2200 Å. The samples are presented in Table 3. 5.

The first SiO_2 layer makes no significant optical difference as its refractive index is similar to the one of glass. This layer is deposited in order to eliminate influence of substrates surface imperfections (impurities, dust, scratches) to the MIF growth. In other words, it insures uniform surface for formation of nanoparticles.

Table 3. 5 Simultaneous EFAD serial samples

sample name	layers and thicknesses/Å	annealing/EFAD conditions (^{o}C/V/min)
Ag MIF (SEF1) A	$SiO_2/Ag/SiO_2$ 1958/90/1305	200/90
Au MIF (SEF3) A	$SiO_2/Au/SiO_2$ 1958/90/1305	200/90
thinner Ag/Au (SEF18) A	$SiO_2/Ag/SiO_2/Au/SiO_2$ 1200/240/1200/90/1200	200/90
thicker Au/Ag (SEF30) A E11 E15	$SiO_2/Au/SiO_2/Ag/SiO_2$ 1200/300/1200/500/1200	200/90 200/500/12 200/500/2.5

thicker Ag/Au (SEF31)	SiO₂/Ag/SiO₂/Au/SiO₂ 1200/500/1200/300/1200	
A		200/90
E6		200/500/5
E14		200/500/2.5
Al/Ag (SEF26)	SiO₂/Al/SiO₂/Ag/SiO₂ 1200/300/1200/500/1200	
A		200/90
E1		200/500/5
E7		200/500/12
F1		200/400/12
Ag/Al (SEF27)	SiO₂/Ag/SiO₂/Al/SiO₂ 1200/500/1200/300/1200	
A		200/90
E2		200/500/5
E8		200/500/12
F2		200/400/12
E20		200/500/2.5
Cu/Ag (SEF28)	SiO₂/Cu/SiO₂/Ag/SiO₂ 1200/300/1200/500/1200	
A		200/90
E3		200/500/5
E13		200/500/20
E18		200/500/30
G6		200/700/5
Ag/Cu (SEF29)	SiO₂/Ag/SiO₂/Cu/SiO₂ 1200/500/1200/300/1200	
A		200/90
E4		200/500/5
E10		200/500/12
E17		200/500/2.5
F3		200/400/12
G7		200/700/2.5

3.2.3. Filter serial

SL glass was used as substrate for the filter (m samples), but also Si wafers (w samples) were coated. Deposition was made in two runs: upon deposition of HL part, one soda-lime and Si wafer were taken out from the chamber (samples B) and clean substrates put for deposition of MIF part (samples C). Substrates were pre-heated for both depositions. HL part of the filter and MIF part with underlying SiO_2 were made separately in order to have simpler multilayer systems for optical characterization instead of the complete filter (A samples). In this way is reduced number of thin films parameters and obtained more reliable models of the samples. Si wafers were used as substrates for two reasons. First, there is no IE among substrate and MIF, so samples on Si can be used for comparison of the influence of IE between glass substrate and layers to multilayer optical properties. Second, Si substrates were used for easier optical characterization of the first SiO_2 layer of HL and MIF part. Namely, soda-lime glass and SiO_2 layers have similar refractive indices resulting in spectra with low number of weak fringes if the layer is thinner that couple of hundreds nm (as it is the case in the design). Using this kind of spectra makes challenging to determine both, SiO_2 layer thickness and refractive index from just one set of data. For this reason is better to use high refractive index substrate that will result in stronger fringes, such as Si (n(550nm) = 4.07).

The thicknesses of layers on Bm, Bw, Cm, Cw, Am, Aw, H20, H21 and H22 samples (treated ones are designated with H) are presented in the Table 3. 6. These thicknesses are obtained from filter design corrected with the corresponding tooling factor, i.e. layers mass thicknesses. EFAD1 stands for treatment with 200/500/15 min conditions and EFAD2 for 300/700/1 conditions.

Table 3. 6. Filter serial samples

sample name	substrate	layers and thickness/Å	treatment	electrode
H10 (NC449)	SL	SiO_2/Au/SiO_2 1958/40/1305	EFAD2	plain
Bm	SL	SiO_2/TiO_2/SiO_2/TiO_2/SiO_2/ TiO_2 1875/626/1150/696/1150/754	-	-
Bw	Si wafer	SiO_2/TiO_2/SiO_2/TiO_2/SiO_2/ TiO_2 1875/626/1150/696/1150/754	-	-
Cm	SL	SiO_2/Ag/SiO_2/Au/SiO_2	-	-

57

		750/70/3588/40/375		
Cw	Si wafer	SiO$_2$/Ag/SiO$_2$/Au/SiO$_2$ 750/70/3588/40/375	-	-
Am	SL	SiO$_2$/TiO$_2$/SiO$_2$/TiO$_2$/SiO$_2$/ TiO$_2$/ SiO$_2$/Ag/SiO$_2$/Au/SiO$_2$ 1875/626/1150/696/1150/754/ 750/70/3588/40/375	-	-
Aw	Si wafer	SiO$_2$/TiO$_2$/SiO$_2$/TiO$_2$/SiO$_2$/ TiO$_2$/ SiO$_2$/Ag/SiO$_2$/Au/SiO$_2$ 1875/626/1150/696/1150/754/ 750/70/3588/40/375	-	-
H20 (Am)	SL	SiO$_2$/TiO$_2$/SiO$_2$/TiO$_2$/SiO$_2$/ TiO$_2$/ SiO$_2$/Ag/SiO$_2$/Au/SiO$_2$ 1875/626/1150/696/1150/754/ 750/70/3588/40/375	EFAD1, EFAD2	macro-structured
H21 (Am)	SL	SiO$_2$/TiO$_2$/SiO$_2$/TiO$_2$/SiO$_2$/ TiO$_2$/ SiO$_2$/Ag/SiO$_2$/Au/SiO$_2$ 1875/626/1150/696/1150/754/ 750/70/3588/40/375	EFAD1, EFAD2	micro-structured
H22 (Am)	SL	SiO$_2$/TiO$_2$/SiO$_2$/TiO$_2$/SiO$_2$/ TiO$_2$/ SiO$_2$/Ag/SiO$_2$/Au/SiO$_2$ 1875/626/1150/696/1150/754/ 750/70/3588/40/375	EFAD1, EFAD2	macro-structured

3.3. Measurements

Current passing through the sample, *I(t)*, was measured and recorded during GP and EFAD as control of the process dynamics (Agilent technologies 34410A multimeter connected to PC). One has to keep in mind that intensity of *I(t)* in presented measurements cannot be compared among the samples because the quantity of charge passing in electric circle depends not only on the sample itself, but also on quality of electric contact with electrodes and samples surface. Optical properties of the samples were measured by ellipsometry and their composition analysed by SIMS. Surface profile of micro-structured sample was obtained from profilometry. Micro-structure was examined optically by microscope. The optical properties

of different areas of the obtained micro-structure were recorded by microspectrophotometry. Except SIMS, all the measurements were done at Ruđer Bošković Institute.

3.3.1. Ellipsometric measurements

Measurements of ellipsometric functions Ψ and Δ were performed by J. A. Woolam V-VASE ellipsometer (Figure 3. 7) in the 0.57-4.47 eV range (corresponding to 2175-277 nm) in 0.02 eV steps. The spectra were taken at 45°, 55° and 65° angle of incidence. Reflectance (R) and transmittance (T) measurements were performed by ellipsometer as well. Reflectance is measured for p polarization at 17.5^o that is the minimal possible angle of incidence at this instrument. Transmittance was taken at normal incidence.

Ellipsometer beam size has 1 mm diameter that enables measurements of small and non-uniform samples, that was the case in this study. Also, it enables that all the measurements (Ψ, Δ, R, T) are taken in the same position on the samples surface. This is also important for non-uniform samples.

All the measurements were done at least three days upon deposition of the coatings to allow for the refractive index changes induced by adsorption of water from atmosphere into the porous layers.

Measurements of ellipsometric functions Ψ and Δ, same as T for more demanding metal containing samples, were used for optical characterization. Reflectance measurements were used for comparison with reflectance of the filter design.

Figure 3. 7. J. A. Woolam V-VASE ellipsometer

3.3.2. SIMS analysis

The samples composition upon GP or EFAD was analyzed by SIMS, using The Hiden Analytical SIMS Workstation, Department of Physics, University in Rijeka. Primary ions were O^{2+}. The final depth of the etched crater was measured with Bruker Dektak XT™ stylus profilometer. SIMS data were used for comparison with refractive index profiles obtained from optical characterization. They were also used for calculation of at% of the compounds.

3.3.3. Profilometry measurements

Surface profile of the micro-structured filter was obtained by 2D measurements of step heights with an Alpha-Step D-600 stylus profilometer (KLA) using a tip with 2.5 micrometers radius and applying a force of 15.0 mg.

3.3.4. Microscopy and microphotospectrometry

Optical microscopy characterization of the micro-structured filter was made by a home-made configuration based on the Cerna modular microscopy platform (Thorlabs) with epi-illumination and trans-illumination for operation in reflection and transmission respectively, usinf a 20X objective (Nikon). Microscopic pictures were recorded by a CMOS Scientific 1.6MP Color Zelux Camera connected to a PC. Microspectrophotometry measurements in reflectance were obtained by coupling a fiber to a C-mount port of the microscope and

sending the collected light to a Ocean Optics HR4000 spectrometer. A one-side polished Si wafer was used as reference for reflectance measurements.

3.4. Data analysis and numerical simulations

3.4.1.   Optical characterization

Optical characterization of the samples was performed using J. A. Woolam WVASE software package. The layers were modelled with either constant refractive index (homogeneous layer) or with refractive index changing as a power law function of the thickness (inhomogeneous layer). However, the latter case is defined as a number of thinner homogeneous sublayers in the characterization software. The optical constants of glasses and SiO_2 were represented by Sellmeier model. For TiO_2 was used Cauchy model and MIFs multiple oscillator model using Gauss oscillators. The number of models layers was kept reasonably low to avoid too much optimization parameters that could lead to the unreliable or unrealistic solutions. For this reason no effort was made to obtain smooth or more detailed refractive index profiles. It was preferred to limit the models to rather rough and simple multilayer systems giving step-wise refractive index profiles but having optical properties that fit well the measured data. It should be noted that the modelling of ellipsometric data for each sample was starting from the simplest model (single layer in the case of poled glass) and the new parameters were introduced gradually. If the new parameter would significantly decrease discrepancy between experimental data and the fit, it would be kept.

3.4.2.   SIMS data

SIMS intensity profile of particular specie in poled glass was normalized as the intensity in bulk corresponds to the known at% in virgin glass. This allowed correlating individual atomic species contribution to polarizability and n. The Lorentz-Lorenz model was used in numerical simulations for comparing polarizability calculated from SIMS and ellipsometry. Lorentz-Lorenz equation is given by:

Eq. 3. 1 $$\frac{n^2-1}{n^2+2} = \sum_i \frac{N_i \alpha_i}{3\varepsilon_0},$$

as a sum over all the species i that contribute to material polarizability, where N_i is the number of molecules per unit volume and α_i is the molecular polarizability. In order to take into account contribution of silica matrix densification suggested by SIMS data, Si concentration is taken constant only in bulk region, while in depletion region is defined as linear function.

No other corrections regarding different etching rates or assuming constant concentration of any specie throughout the whole sample were applied.

3.4.3. Numerical simulations of glass poling and simultaneous EFAD

Modelling of glass poling processes has been usually performed assuming that the process can be entirely represented by the drift and diffusion of alkali and earth alkali species, neglecting, among others, possible chemical processes (NBO to BO changes), or dependences of diffusion and mobility coefficients on the ion concentration. In this framework, the existing models [83] were generalized to include an arbitrary number of mobile species.

During GP and EFAD process the movement of n_s different ionic species with initial concentration profiles C_{i0} is described by the following differential equations [83]:

Eq. 3. 2
$$\frac{\partial C_i}{\partial t} = \mu_i \frac{\partial (EC_i)}{\partial x} + D_i \frac{\partial^2 C_i}{\partial x^2}$$

Eq. 3. 3
$$\frac{\partial E}{\partial x} = \frac{e}{\varepsilon_0 \varepsilon} \sum_{i=1}^{n_s} q_i \left(C_i - C_{i0} \right), \qquad\qquad i = 1, 2, \dots, n_s$$

where C_i is the concentration of ions of the i-th element, E is the electric field amplitude, x is the position in the glass, with $x = 0$ being the sample surface next to the anode, and t is the time. The parameters μ_i, D_i, and q_i are the mobility, diffusion coefficient and charge of the i-th species, while e is the elementary electric charge, ε_0 the vacuum permittivity and $\varepsilon=7$ the static dielectric function of glass. The first equation states that the time evolution of ion concentration is given by the drift and diffusion currents (first and second right-hand term, respectively). The second equation is the one-dimensional Poisson equation and describes the spatial variation of the electric field upon redistribution of charges with respect to their initial concentration (C_{i0}).

These equations can be written in a more compact form in order to solve them numerically. First, the ion mobility and diffusion coefficients are related by the modified Nernst-Einstein equation [137, 138]:

Eq. 3. 4
$$\mu_i = \frac{D_i e}{H k_B T}$$

where H is the Haven ratio around 0.3 first observed by Fitzgerald [139] and confirmed by others [140], k_B is the Boltzmann constant and T the temperature. In addition, one can introduce the following parameters:

i) $d_0 = \sqrt{2\varepsilon_0\varepsilon U/eC_0}$ with C_0 the initial total ion charge concentration ($C_0 = \sum_{i=1}^{n_s} q_i C_{i0}$) and U is the external applied potential

ii) $E_0 = U/d_0$

iii) $t_0 = d_0/(\mu_1 E_0)$.

These parameters correspond to the maximum thickness of ion-depleted layer in blocking configuration (d_0), the resulting electric field if all the potential is applied in d_0 (E_0) and the time that the carriers of the first species ($i = 1$) need to cross the region d_0 when E_0 is applied (t_0). Using these parameters, one can define dimensionless time ($\tau = t/t_0$) and position ($s = x/d_0$) coordinates and functions ($p_i = C_i/C_0$ and $f = E/E_0$). Then Eq. 3. *2* and Eq. 3. *3* can be reformulated as:

Eq. 3. 5 $\dfrac{\partial p_i}{\partial \tau} = \gamma_i \dfrac{\partial(f p_i)}{\partial s} + v_i \dfrac{\partial^2 p_i}{\partial s^2}$

Eq. 3. 6 $\dfrac{\partial f}{\partial s} = \sum_{i=1}^{n_s}(q_i p_i) - p_0,$ $i = 1,2,\dots,n_s$

with $\gamma_i = \mu_i/\mu_1$, $v_i = \gamma_i H k_B T/(q_i e U)$ and $p_0 = \sum_{i=1}^{n_s} q_i C_{i0}/C_0$.

Solving these differential equations requires initial and boundary conditions that will depend on the specific problem (ion types, blocking/non blocking conditions, presence of dielectric layers, etc.). In glass poling experiments under application of a constant voltage, the following boundary condition can be imposed:

Eq. 3. 7 $\int_0^L f\, ds = 1$

where $L = W/d_0$ is the normalized sample thickness and W is its physical thickness. Numerical solution of these equations is studied for several cases using the ODE15s algorithm implemented in MATLAB.

The model described above was applied to analyze the glass poling process to glasses containing different number of alkali species (two for KF9, three in BK7 and 4 in SL), going beyond the literature works that were limited to two intrinsic ion species [83, 127]. Furthermore, since the model is solved numerically, the initial concentration profiles can be arbitrary. In this way, the model can be easily generalized to include the presence of metal ions initially restricted to a dielectric region with no alkali ions in order to simulate the

electric assisted dissolution of MIF layers embedded in dielectric multilayers, as done in the analysis of simultaneous EFAD serial.

4. Results and discussion

In this chapter will be presented results and discussions for each set of the samples separately.

4.1. GP serial

In the scope of this part of research, properties of SL, BK7 and KF9 glasses upon GP were studied. Samples was $n(d)$ obtained from ellipsometric measurements. Polarizability profiles of poled samples were then obtained from $n(d)$. Poled samples were measured with SIMS, and atomic percent (at%) profiles of atomic species were obtained from the SIMS data. Numerical simulations of ionic composition in glass during GP were performed. The polarizability profiles obtained from $n(d)$ and the polarizability profiles proportional to SIMS concentrations of ionic species were correlated. At% derived from SIMS data and numerical simulation results were also compared to verify theoretical model.

Results

Current measurements of the poled samples are presented in *Figure 4. 1*. All the samples present sharp jump of $I(t)$ when potential is turned on. The intensity of current and its decrease can be related to the concentration of fast (Na^+, K^+) and slow (Ca^{2+}, Mg^{2+}) charge carriers. KF9 has high concentration of Na and no alkali earths that result in high current and fast decay (Figure 4. *1*. a) and b)). The process in vacuum is characterised by faster decay that can be associated to the lack of cations (H^+/H_3O^+) penetrating into the sample to compensate positive charge depletion. Both kinds of carriers, fast and slow, are present in SL glass. Moderate concentration of fast carriers results in lower current compared with KF9 and presence of slow carriers in longer decay tail (Figure 4. *1* c)). Low current BK7 glass indicates weaker contact with electrodes (Figure 4. *1* d)).
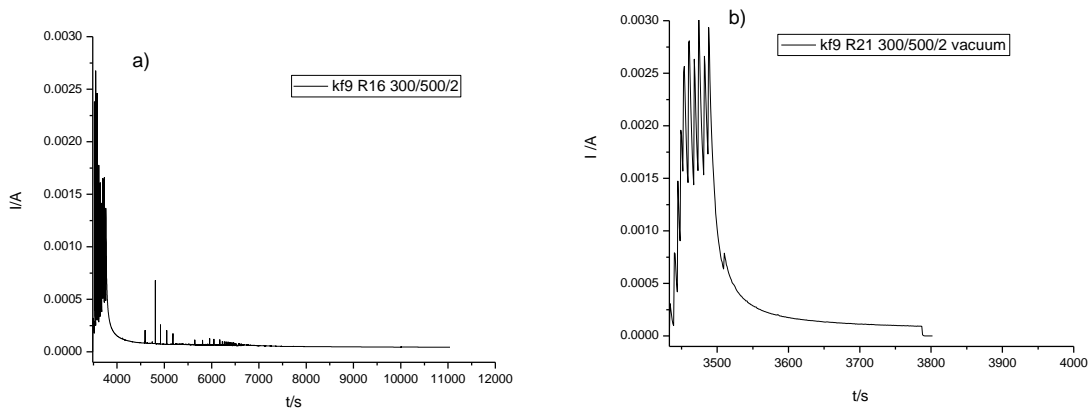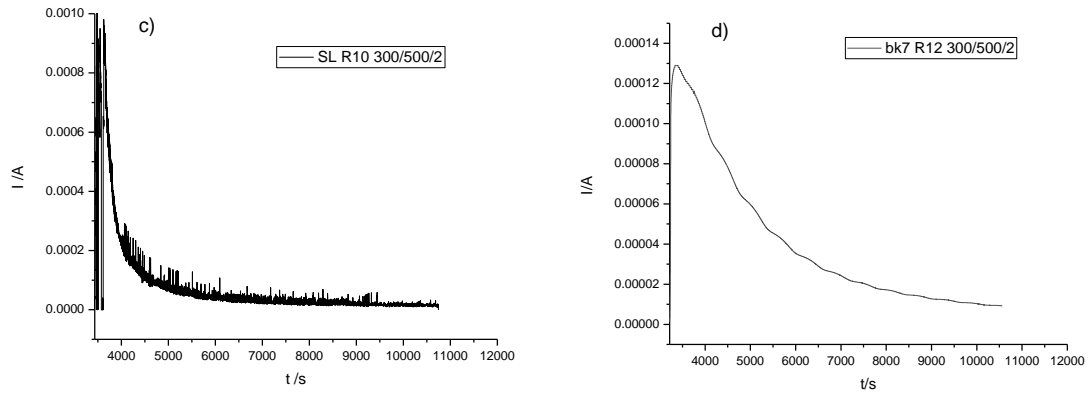
Figure 4. 1. Current (*I(t)*) measurements in the course of GP.

Figure 4. *2*. shows Ψ (a, c and e) and Δ (b, d and f) ellipsometric functions experimental data and fits for virgin and poled glasses. There is visible change (fringes) in Ψ of poled samples in comparison to Ψ of the virgin glass, which leads to conclusion that GP changed *n* of the glass.
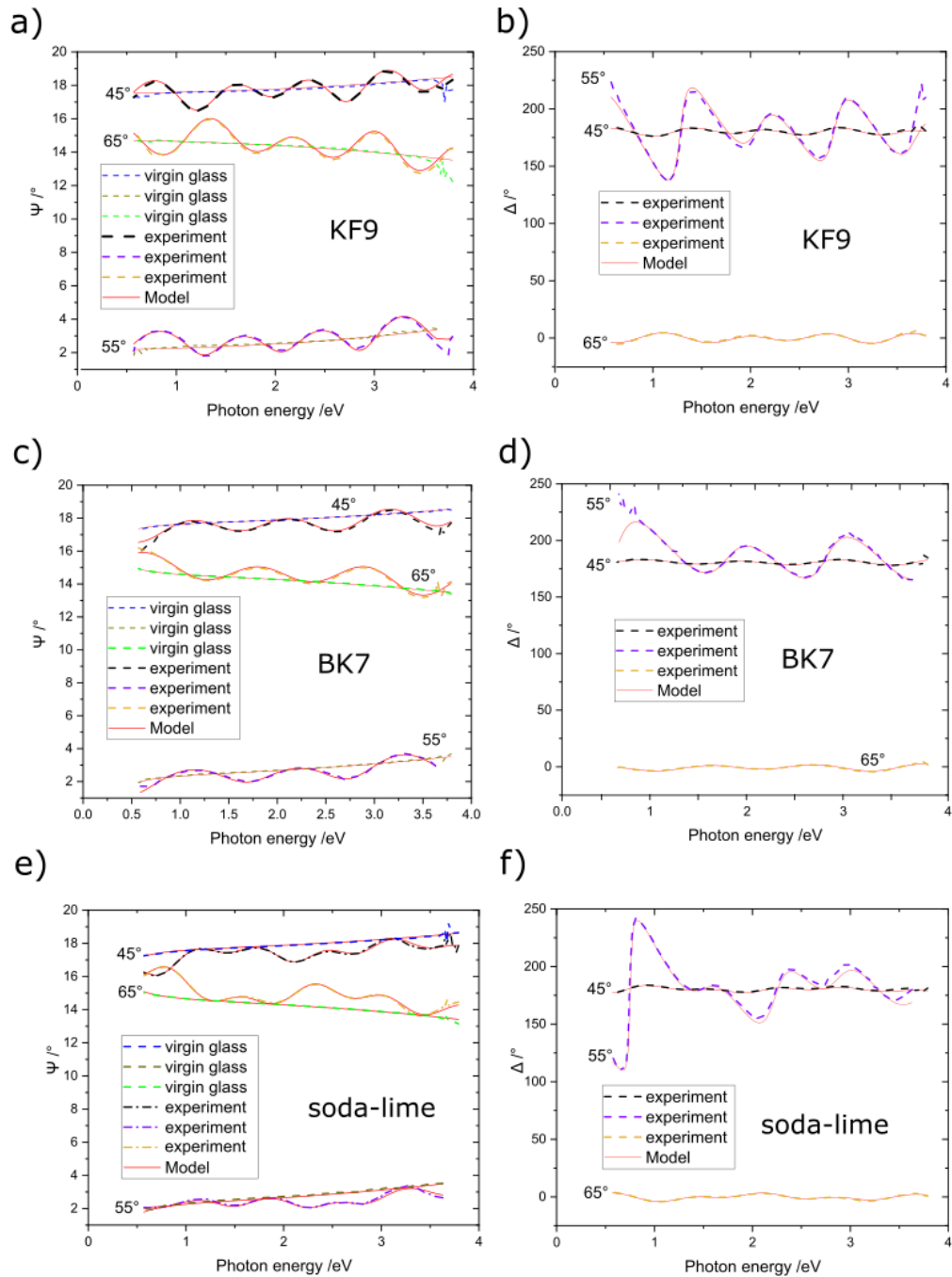
Figure 4. 2. Measured and fitted ellipsometric Ψ (left) and Δ (right) functions of virgin and poled KF9, BK7 and SL glasses at three incidence angles.

Figure 4. *3*. presents *n(d)* of KF9, BK7 and SL samples poled in air, and KF9 sample poled in vacuum. SL glass *n(d)* presents *n* peak in front of bulk region, that is in accordance with [80] where is suggested it may be a consequence of Ca and Mg ion accumulation in this region. KF9 and BK7 glass are free from Ca and Mg, so no pile up of alkali earth ions concentration and resulting peak in *n* should be expected. Therefore *n(d)* be simply step-like. However, it decreases until minimum at the depth of approximately 300-500 nm. Poling of

67

KF9 was made in vacuum as well and the resulting profile shows the same trend as in the case of poling in air. In the case of BK7, *n* increases a bit before it reaches the bulk value.
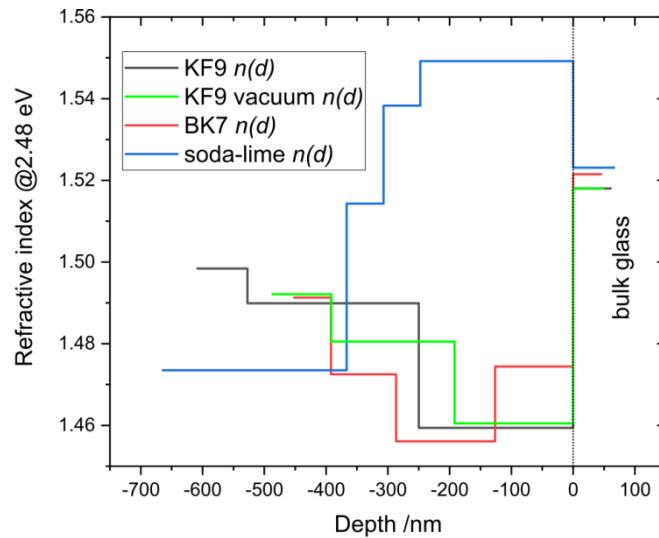
Figure 4. 3. *n(d)* of KF9 poled in air and vacuum, BK7 and SL glass in air. Interface between zones is at 0 nm: positive values present bulk and negative depletion zone.

Figure 4. *4*. presents intensities of Si, alkali and earth alkali ions in KF9, BK7 and SL glasses obtained by SIMS compared with *n(d)* obtained by ellipsometry. It should be noted that in all the cases Si signal decreases in near-surface volume of samples, which is depleted of alkali and earth alkali ions. In the case of KF9 glass, the decrease of Si signal is approx. 35% in approx. 520 nm of the depleted region. Comparing with KF9 *n(d)*, this corresponds well with the decrease of *n* (from 1.498 at the surface to 1.459, *Δn* = 0.039 in 608 nm). Thickness discrepancy between SIMS and ellipsometry based model here is 15%. For BK7 glass, the decrease of Si signal is approx. 30% in 300 nm before Ba accumulation (*Figure 4. 4.* (b)). Comparing with BK7 *n(d)*, this again corresponds well with *n* decrease (from 1.491 at the surface to 1.456, *Δn* = 0.039 in 326 nm). Thickness discrepancy between SIMS and ellipsometry based model for this sample is 12%.
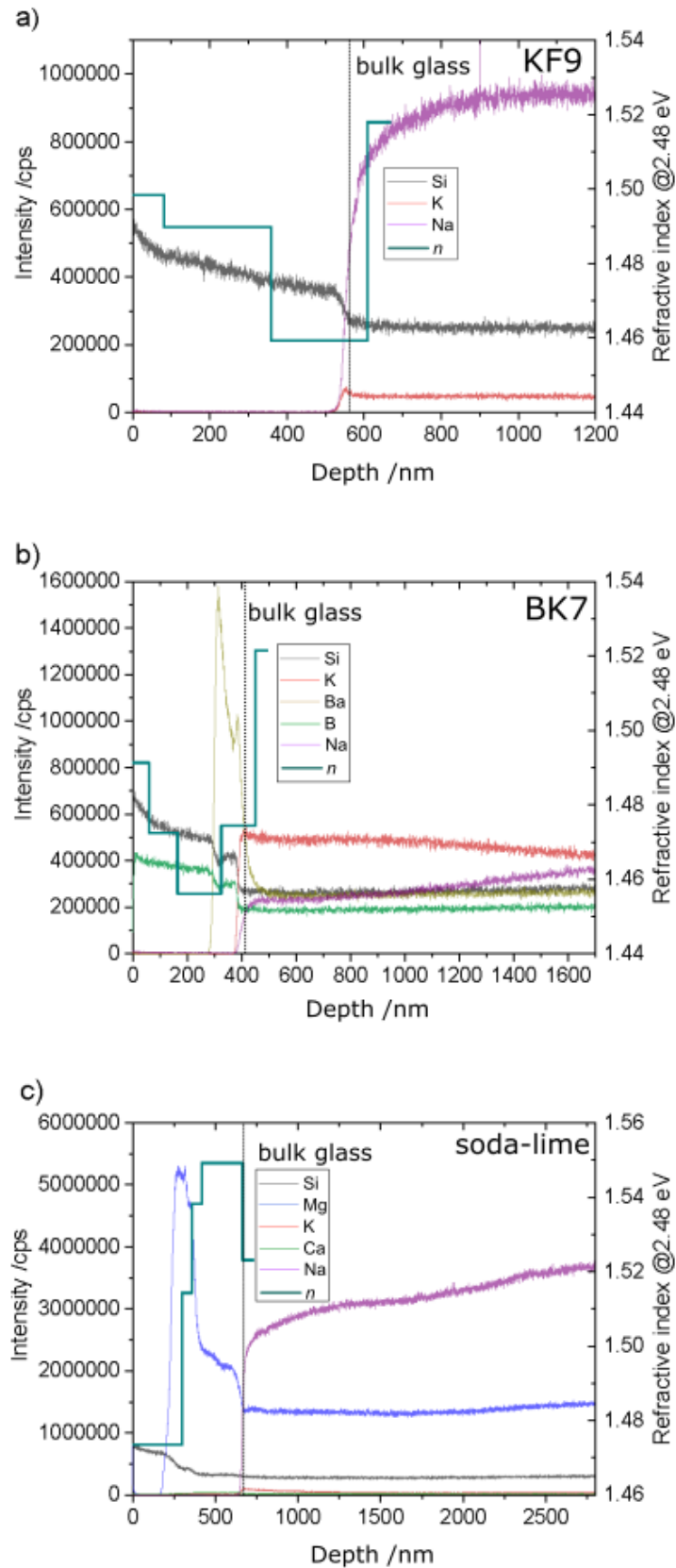
Figure 4. 4. SIMS intensity vs. *n(d)* for poled KF9 (a), BK7 (b) and SL (c) glass. Air/glass interface is at 0 nm, and bulk is at positive values.

Figure 4. 5. presents the polarizability profiles of KF9, BK7 and SL. obtained as a sum of individual contributions of ionic species, assumed to be proportional to the SIMS concentration, fitted to *n(d)* profiles obtained from ellipsometric measurements. The following equation was used:

Eq. 4. 1 $$\frac{n^2-1}{n^2+2} = \sum_{i=1}^{N} A_i I_i,$$

where A_i is a proportionality constant and I_i is calculated from SIMS concentration for *i*-th species contributing to polarizability. Figure 4. 5. (b), (d) and (f) show the individual contributions from Na^+, K^+, Ca^{2+}, Mg^{2+} and Ba^{2+}. A_i was obtained by fitting the polarizability profiles found from SIMS concentrations to the polarizability found by ellipsometry according to the *Eq. 4. 1*. Only, instead of Si SIMS data, a linear variation of Si concentration due to possible matrix densification was used. A re-scaling parameter was optimized to account for possible differences in depth of SIMS and ellipsometry. The depletion zone depths used for atomic contribution simulations are 550, 390 and 380 nm for KF9, BK7 and SL glass, respectively. Thickness discrepancy between SIMS and ellipsometry based model for SL sample is 3%.
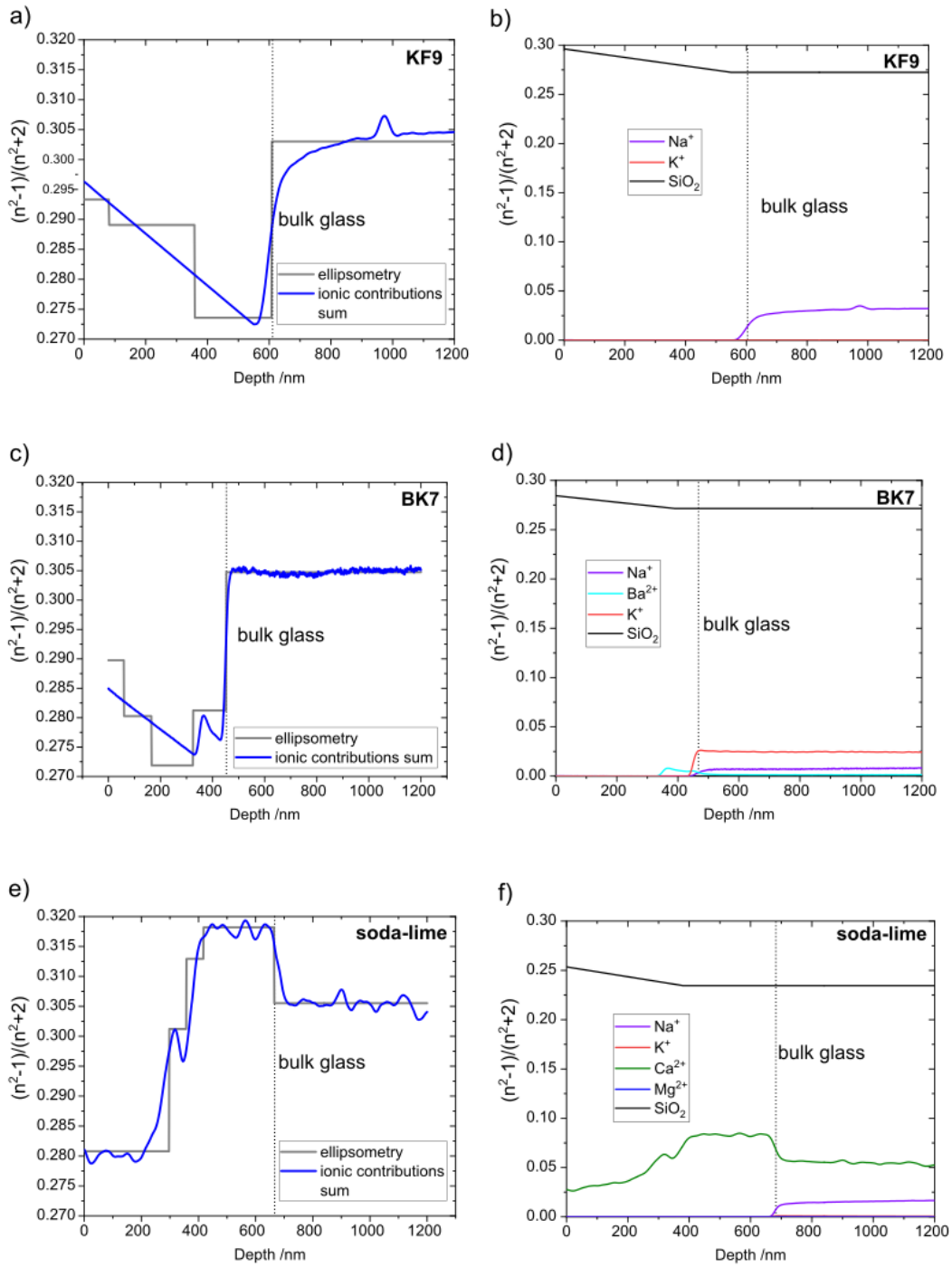
Figure 4. 5. Polarizability profiles of KF9 (a), BK7(c) and SL (e) glasses obtained from optical characterization and SIMS measurement. Polarizability contribution from individual atomic species contained in KF9 (b), BK7 (d) and S (f) obtained from simulations. Air/glass interface is at 0 nm, and bulk is at positive values.

In the case of KF9, polarizability has the lowest value at the edge of the depletion zone, while in bulk and near-surface it has higher values. In the case of BK7 the increase in polarizability in front of the bulk region coincides well with accumulation of Ba from SIMS measurements. Results for SL sample show polarizability peak in front of bulk region corresponding to accumulated Ca^{2+} ions presenting high contribution to polarizability. Na^+ contribution is significant, while K^+ and Mg^{2+} polarizability influence seems to be nearly negligible. One has to keep in mind that the influence of each individual specie to the total polarizability depend on at% of the specie in glass. For example, Na^+ influence on polarizability is the highest in KF9, lower in SL and the lowest in BK7 and K^+ influence is very low in KF9 and SL (less than 1 at% of K^+), while in BK7 (4.3% of K^+) it is considerable. This is in agreement with virgin glass composition (Table 3. *2*) and graphs of at% calculated from SIMS data (Figure 4. *6.*).
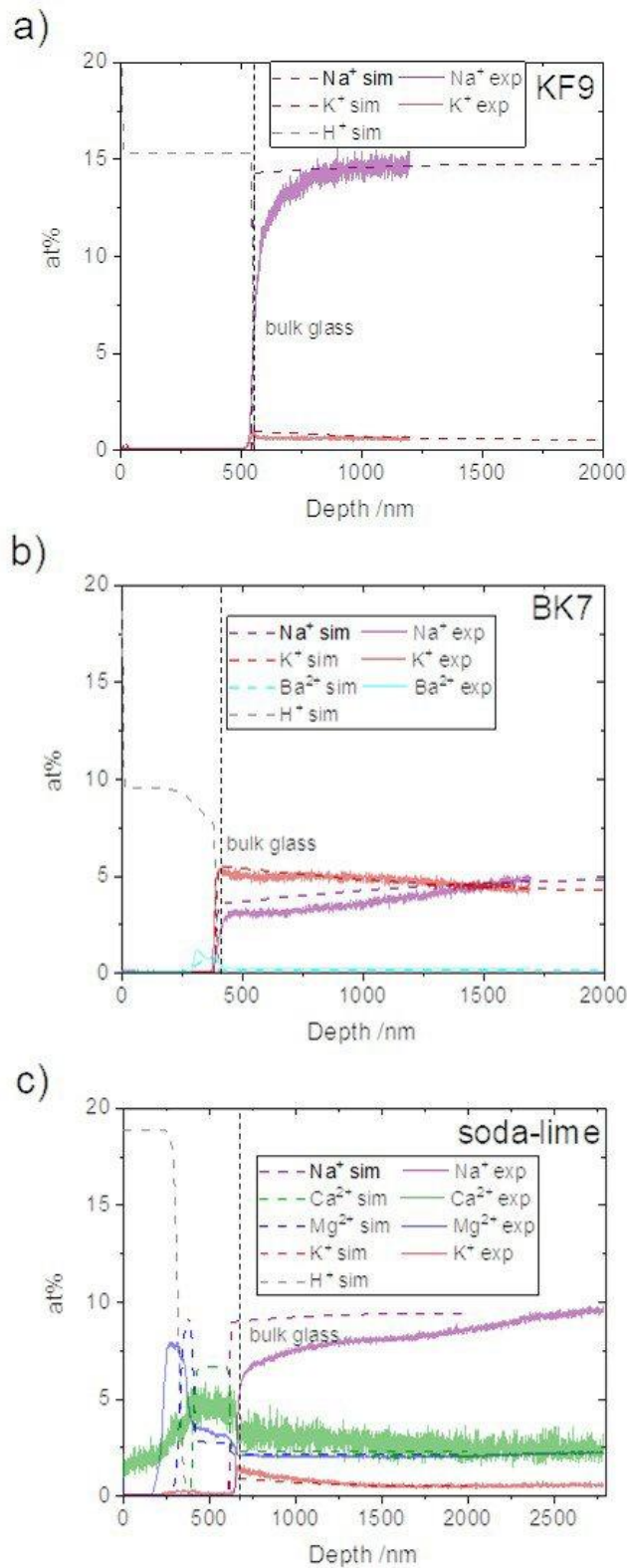
Figure 4. 6. Comparison of at% profiles of a) KF9, b) BK7 and c) SL glass obtained from simulations and SIMS measurements. Air/glass interface is at 0 nm, and bulk is at positive value.

Comparison of at% profiles of the poled samples calculated from experimental SIMS data and from numerical simulations of the KF9, BK7 and SL samples are given in Figure 4. 6. The figure shows good agreement of experimental and simulated at% for these types of glasses. High concentration of H^+ ions in simulation is a consequence of assumed abundance of H^+ at the air/glass interface. The final mobilities used in simulations are given in Table 4. 1.

Table 4. 1. Ionic mobilites of SL, BK7 and KF9 glasses.

	$\mu(Na)/$ $m^2(Vs)^{-1}$	$\mu(Ca)/$ $m^2(Vs)^{-1}$	$\mu(H)/$ $m^2(Vs)^{-1}$	$\mu(K)/$ $m^2(Vs)^{-1}$	$\mu(Mg)/$ $m^2(Vs)^{-1}$	$\mu(Ba)/$ $m^2(Vs)^{-1}$
SL	$5.4 \cdot 10^{-15}$	$= 9 \cdot 10^{-20}$	$2 \cdot 10^{-20}$	$2 \cdot 10^{-15}$	$3 \cdot 10^{-20}$	-
BK7	$5.4 \cdot 10^{-15}$	-	$2 \cdot 10^{-20}$	$2 \cdot 10^{-15}$	-	$1.6 \cdot 10^{-20}$
KF9	$5.4 \cdot 10^{-15}$	-	$4.2 \cdot 10^{-20}$	$2 \cdot 10^{-15}$	-	-

Discussion

The optical properties of final models obtained from optical characterization are in very good accordance with the measured data. The models are not complex as they contain low number of parameters (3-4 layers, each layer 3-5 parameters). Therefore, the obtained $n(d)$ may be taken as reliable results.

While $n(d)$ profile for SL is consistent with [80], the profiles for KF9 and BK7 present minimum value in front of bulk region. The result is consistent also for KF9 poled in vacuum. The question is: what is the origin of the n decrease towards bulk in KF9 and BK7 glasses. SIMS data do not suggest mobile species concentration profile that could give explanation to the obtained $n(d)$. At the other hand, one can notice nearly linear decrease of Si signal towards bulk region for both samples (Figure 4. 4). Comparing SIMS data and $n(d)$ it is possible to conclude that the origin of the $n(d)$ decrease and appearance of refractive index minimum in depleted region is the change in silica matrix density.

As mentioned previously, GP in this work was done with pressed electrodes, that present semi-open (semi-blocking) poling setup [141]. This means that the supply of H^+/H_3O^+ ions is not sufficient to compensate the lack of positive charge, so it is expected that NBO transforms to BO by the release of O^- and formation of Si-O-Si bonds. This is accompanied by the increased number of members in SiO_4 tetrahedra rings, altogether increasing the matrix density towards the silica-like one [86, 85 , 142] .Transformation rate of NBO to BO and/or

increase of tetrahedra ring members is not uniform throughout depleted layer but is higher closer to the anode due to the lack of positive species to compensate alkali drift. Increased matrix density leads to the increase in n (and polarizability) that is in accordance with presented profiles. Similar fingerprint of silica matrix restructuring, although indicated by Si SIMS data, was overlooked and not included in previous study of poled SL glass $n(d)$ [80]. The reason for this was presence of Ca^{2+} pile up next to the bulk region, which meant modelling demanded significant number of parameters. Also, Ca^{2+} pile up influence on $n(d)$ partially masks the contribution of matrix restructuring in a relatively thin sub-anodic layer of 200 nm or less. Therefore, glasses without earth alkalis represent simpler systems where it is easier to distinguish matrix densification contribution to $n(d)$.

It is possible to roughly estimate the expected values of n due to silica matrix restructuring and compare them with the obtained results. The most compact type of SiO_2 matrix is its crystalline form, i.e. quartz, with $n=1.55$ at 500 nm (2.48 eV) (Table 4. 2). The amount of impurities, NBO and SiO_4 tetrahedra rings with less than four members should be negligible. Its glassy form (significant concentration of less than four member SiO_4 tetrahedra rings), fused silica, has less dense structure with n equal to 1.462-1.466 at 500 nm (2.48 eV) (depending of grade, content of Si-OH bonds may be from couple of tens to couple of hundreds ppm, not influencing n in visible range significantly) [143]. Densities and n of KF9 and BK7 are between values for quartz and fused silica. Besides silica, as the main matrix former, these glasses contain 10.9 wt% B_2O_3 (BK7) and 6.4 wt% TiO_2 (KF9) and significant amount of NBO bonds neutralized by alkali and earth alkalis. Minimal n obtained upon GP is around 1.46 that is somewhat lower than the value for fused silica. The obtained minimal value corresponds to the structure depleted of alkalis and not filled with other species, with matrix density lower than fused silica one. At the same time, maximal n is significantly higher in the near-surface depth, around 1.49-1.5, but still lower than virgin glass or quartz. The structure in this region is also alkali depleted, but density (and n) is more silica-like due to matrix restructuring by NBO transforming to BO and SiO_4 tetrahedra rings gaining more members in sub-anodic region. Using EMA, simulation of the mixture of fused silica with 3.6 vol% of TiO_2 (corresponding to 6.4 wt% TiO_2 in KF9) results in effective n value 1.485 (at 500 nm), that is in good accordance with the obtained n_{max} of KF9 sample. This mixture should roughly correspond to alkali depleted KF9 glass with fused silica matrix structure. It can be concluded that the obtained refractive index values are realistic according to the expected glass structure and composition.

Table 4. 2. Density and refractive index of quartz, fused silica KF9 and BK7 glasses.

	density (g/cm^3)	n (at 500 nm or 2.48 eV)	
		n_{min}	n_{max}
air poled KF9	-	1.4594	1.4984
vacuum poled KF9	-	1.4605	1.4921
air poled BK7	-	1.4561	1.4913
quartz	2.649 [144]	1.55	
fused silica	2.20 [143]	1.462-1.466 [143]	
KF9	2.50 [65]	1.5177	
BK7	2.51 [63]	1.5215	

KF9 contains only highly mobile Na^+ and K^+, while BK7 in addition contains low amount of Ba^{2+}. Although Ba^{2+} concentration is low, its ion diameter is large and therefore it can be expected it has large dipole moment and may significantly influence polarizability, resulting in the increase of poled KF9 n in front of bulk, where it accumulated (Figure 4. *4*. (b). Polarizability contribution of Na^+ is probably masked by the Ca^{2+} to some degree, since simulated polarizability peak (*Figure 4. 5* (f)) is fitted only with Ca^{2+}. Polarizability of Ca^{2+} in bulk region is determined by the polarizability of Ca^{2+} in the peak region. The difference in at% at peak and in bulk for Ca^{2+} is approximately 2:1, so this also sets the bulk value of Ca^{2+}. Polarizability of Ca^{2+} in bulk is therefore probably overestimated and the one of Na^+ underestimated by the fit. The obtained low Mg^{2+} polarizability may be ascribed to its small radius, compared to Ca^{2+}, but also to the concentration peak overlapping with the one of Ca^{2+} and possible underestimation of its contribution by overestimation of Ca contribution in the course of numerical optimization. The linear model of glass matrix (Si) contribution to polarizability provided results consistent with ellipsometric models of *n(d)*.

Numerical simulations of ionic mobilities used Haven ratio equal to H = 0.3, a value within range of experimental results by Fitzgerald and others. As can be seen in Figure 4. *6*, SIMS obtained at% profiles show greater diffusion than simulation profiles. However, using

higher H value in simulations deteriorates the at% profiles obtained from SIMS in comparison with at% obtained from simulations. It was previously stated that a simplified model was used, which could explain almost step-like profile of simulated at%.

Initial $\mu(Na)$, $\mu(Ca)$, $\mu(H)$ and $\mu(K)$ used in numerical simulations were taken from [83]. Different authors provide different values of μ, depending on the type of glass and poling conditions, but here ionic mobilities are consistent for all types of glass. $\mu(K)$ was altered to get a good fit to SIMS data, while $\mu(Na)$, $\mu(Ca)$ and $\mu(H)$ remained the same, or only slightly modified. Since the models of BK7 and SL glass were more complex than in previous works, $\mu(Mg)$ and $\mu(Ba)$ were found through iterating simulations and fitting the obtained profiles to SIMS experimental data.

Mobility of hydrogen ions, $\mu(H)$, in KF9 is higher than in SL and BK7 glasses. The reason for this could be explained by the mixed ion effect, as follows. Since Na^+ and K^+ have mobilities considerably higher than other ions, and of the same order of magnitude, these two ionic species drift into the glass and leave vacancies in which other ions can jump. In KF9 there is no additional ionic species to reduce drift of H^+ into glass matrix, while in both SL and BK7 there are: Ca^{2+} and Mg^{2+} in SL, and Ba^{2+} in BK7. This is why KF9 will allow higher effective mobility of hydrogen ions than SL and BK7.

It should be noted that non-blocking anode configuration was assumed in the numerical simulations, while the experiments were performed in a semi-blocking anode configuration. Yet, the model is able to provide a good correspondence with the experimentally determined concentration profiles. The fact that NBO to BO rearrangement and some other effects, such as drift of negative oxygen ions toward the anode, is neglected in the model can be partially compensated by unlimited H^+ ions abundance at the air/surface interface considered in the simulations.

Finally, the dips of n in depleted region of poled BK7 and KF9 glass require more parameters in optical characterization than expected. The additional modification of n due to doping with metal ions would make their modelling equally, if not more, complex as for SL glass. Therefore, the later was chosen as the most appropriate for filters substrate.

4.2. Simultaneous EFAD serial

Bimetal samples of Ag with Al, Cu and Au embedded in SiO$_2$ layers were treated with EFAD using plain electrode. Besides this, set of samples combining Ag and Au was annealed. The samples were first inspected visually and then those containing Ag and Au were chosen to be further studied by ellipsometry followed with optical characterization and SIMS analysis. Additionally, numerical simulations of EFAD dynamics were performed.

4.2.1. Combinations of Ag with Al and Cu

It can be seen (Figure 4. *7*) that EFAD of Ag with Al systems is able to completely dissolute both metals in the case of Al/Ag sample applying conditions 200/500/12 min (E7). At the other hand, application of the same conditions to Ag/Al sample could not achieve the same result (E8). However, shorter time (2.5 min E20 or 5 min E2) or lower voltage (400V F2) results in gradation of dissolution, indicating possibility to well control the process.

EFAD of Cu/Ag combination did not show visible changes in reflectance or transmittance even after process with strong conditions (200/500/30 min E18 or 200/700/5 min G6). At the other hand, for Ag/Cu combination mild conditions (200/500/5 min E4 or 200/400/12 min F3) were enough to obtain semi-transparent samples. Complete dissolution was not obtained at stronger conditions (200/700/2.5 min G7). This interesting result suggests that Cu layer is making a kind of barrier for dissolution of Ag and might be a topic of future research.
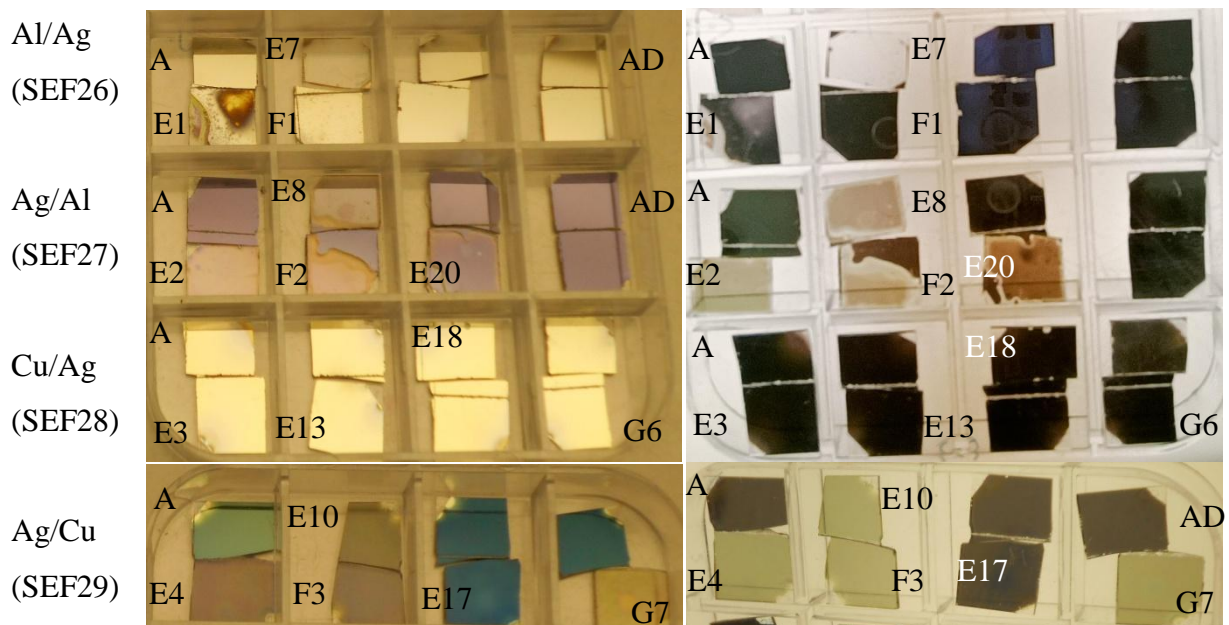
Figure 4. 7. Photo of Ag with Al and Cu samples: in reflectance (left) and transmittance (right).

These observations can be related with *I(t)* presented in Figure 4. 8. (and Figure 4. 9): the curves generally have complex appearance with shoulders indicating changes in process dynamics due to the drift of carriers with different mobilities. However, Cu/Ag *I(t)* (Figure 4. 8. c)) looks simpler resembling dynamics of GP process, confirming absence of contribution from some carriers or their very low mobility.
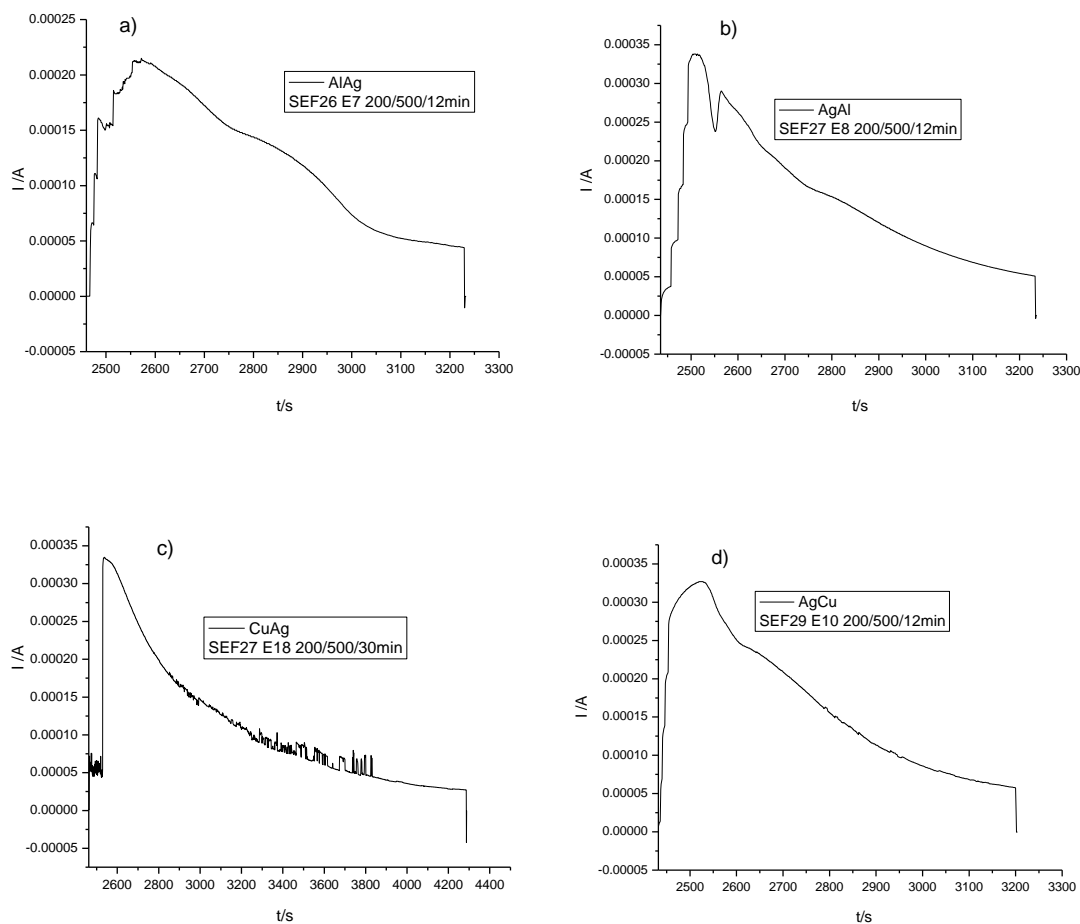
Figure 4. 8. Current curves of EFAD of Ag with Al, and Cu bimetal systems.

Samples of Ag with Al, and Cu combinations were inspected only visually. Although Ag/Al samples indicate possibility of good control of optical properties, plasmonic properties of Al MIF are weak and broad and if compact layer would be applied in the filter, its optical properties are very similar as those of Ag. For these reasons it would be very difficult to design optical filter with visibly different colours depending on the presence of the metals.

Therefore, this combination was not explored further. In the case of Ag/Cu sample, the changes in sample are too fast to control them by EFAD: it would be very difficult to make repeatable process with time lower than 5 min or voltage lower than 400 V. Finally, although the results are interesting from the fundamental point of wiev, Ag in combination with Al or Cu was rejected as bimetal system candidates for the micro-structured filter.

4.2.2. Combinations of Ag with Au

4.2.2.1. Effects of thermal annealing

The *I(t)* curves of Ag with Au bimetal systems witness the complexity of EFAD process (Figure 4. 9) pointing at the contribution of different ions.
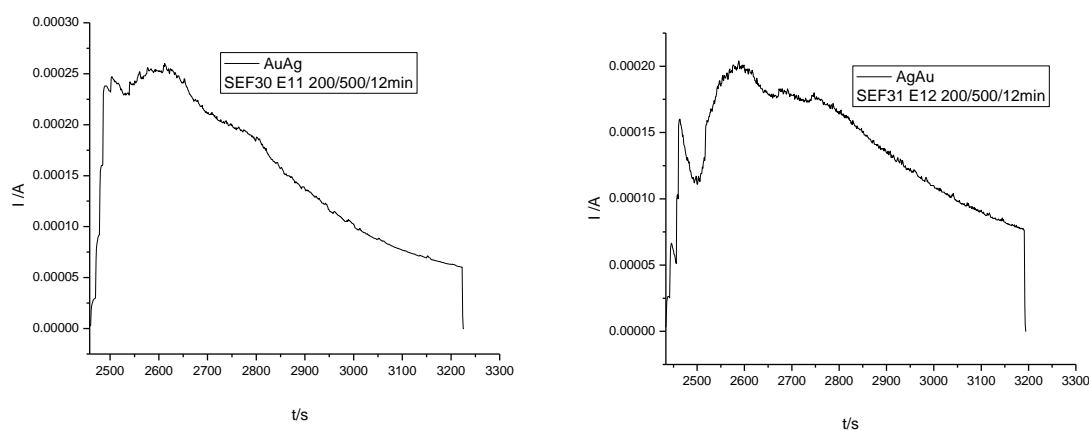
Figure 4. 9. Current curves of EFAD of Ag with Au bimetal systems.

Figure 4. *10* shows the composition of the distribution of annealed thicker Ag/Au and Au/Ag samples. In both samples, there is a significant redistribution of Ag and alkali ions (Na^+ and Ca^{2+}) while Au appears to remain at the position in which it was deposited. It turns out that Ag piles up in the Au layer. The quantity of material in MIF can be related with the intensity curve. The ratio of the Ag quantity in the Au layer to the Ag quantity in the Ag layer ([Ag@Au]/[Ag@Ag]) is approximately 0.26 in the Ag/Au sample and 0.39 in the Au/Ag sample. Sodium piles up approximately the same in both MIF layers and can be found also in all SiO_2 layers. The ratio of the Na quantity in the Au layer to the Na quantity in the Ag layer ([Na@Au]/[Na@Ag]) is 0.83 in Ag/Au sample and 0.7 in Au/Ag sample. These observations suggest that the redistribution of Ag and Na is dominated by ion exchange and a preferential tendency of Ag to diffuse into the Au layer. The nearly constant profile of Ca and its lack of correlation with the Ag concentration profile points out a simple diffusion process [145]. Au, due to its low diffusivity and large ionic charge (3+) is less prone to participate in the ion

80

exchange process [146]. It has also been reported that Ag diffusion in Au is faster than Au diffusion in Ag [147], in accordance with the asymmetric behaviour of Ag and Au observed in the samples.
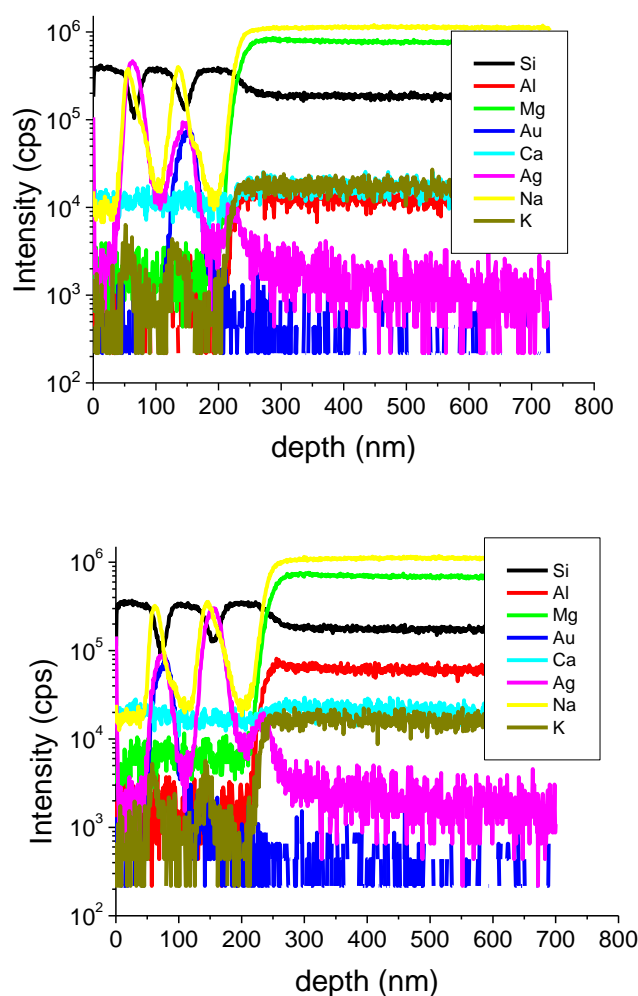
Figure 4. 10. SIMS compositional profile of the annealed thicker Au/Ag (top) and Ag/Au (bottom) samples. The interface between the coating and glass is revealed by the steep growth of Al intensity.

Figure 4. *11* shows the imaginary parts of the effective dielectric function of Au (top) and Ag (bottom) in as-deposited and annealed Ag MIF, Au MIF and thicker and thinner bimetal samples. In both cases, the LSPR peak becomes more intense and shifts to lower energies with the quantity of the deposited metal. This behaviour is associated with a growth of metal fraction in the MIF layer as well as an increase in the aspect ratio of particles with

the amount of deposited metal [40]. The contributions to the imaginary part of the dielectric function in Au at high photon energies (>2.5 eV) are related to the interband transitions [39]. Upon annealing, a slight shift of the plasmon resonance towards lower energies is observed in the case of Ag, which suggests a mild Ag surface oxidization. There is also a small shift in the Au sample in the opposite direction. This shift is more pronounced in the case of bimetal samples: metal nanoparticles become more spherical and isolated from each other by annealing and the plasmon peak shifts towards higher energies [148].

The most remarkable effect of annealing in bimetal samples is the appearance of a secondary shoulder/peak at lower photon energies than the main plasmon peak. This peak is a signature of interaction among the particles that is stronger as the inter-particle distance decreases [149, 150]. In the case of Ag, the main peak grows and narrows with the annealing indicating the reshaping of MIF. This is the reason why the Ag shoulder of the thicker sample becomes more visible: although nanoparticles have become more spherical and distant, there is still a large fraction of them close enough to display this absorption feature. The thinner samples have less Ag, so the shoulders, even if present, are not so much pronounced. Au shoulder of the thinner sample grew much higher upon annealing although there is no significant change in the main peak position or shape. Such an increase in the shoulder intensity can be understood by the presence of more metal in MIF in comparison to the as-deposited sample, which can be connected with the diffusion of Ag into the Au layer revealed by SIMS. The change is less remarkable in the case of thicker layers. The mass thickness ratio of Ag to Au in the thicker samples is 5:3 and in the thinner ones 8:3, meaning that there is even less Au in comparison with Ag in the latter (thinner) one. Consequently, additional Ag impacts more optical properties of the thinner than the thicker MIF samples.
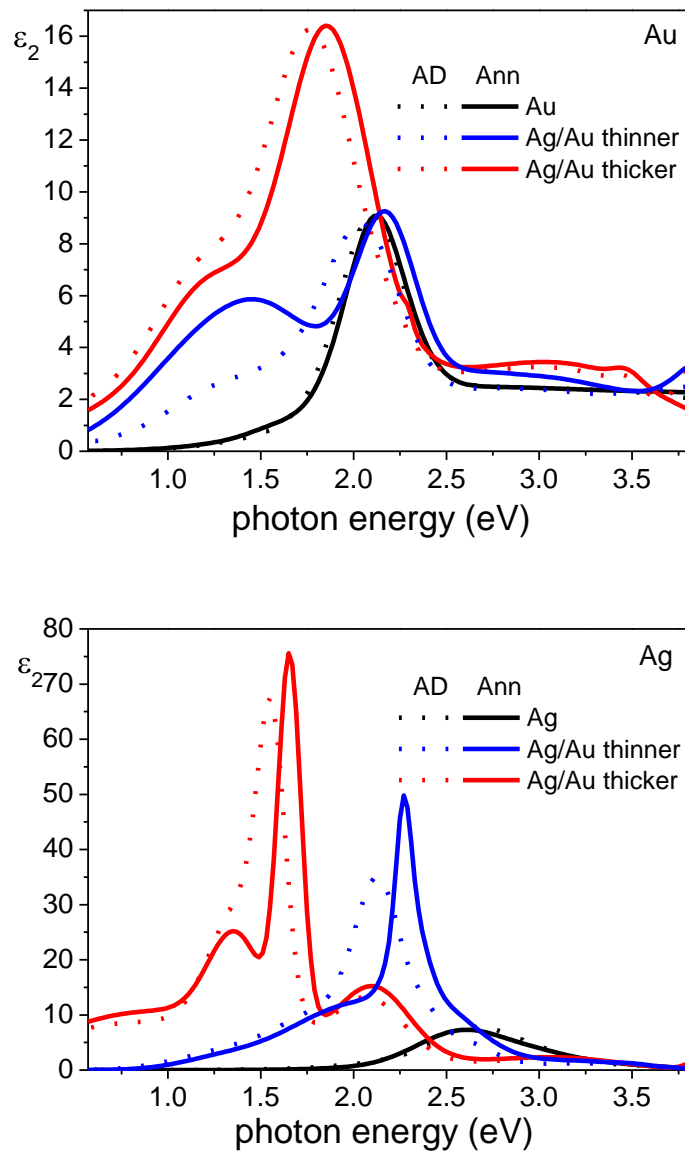
Figure 4. 11. Imaginary part of Ag and Au effective dielectric functions for single MIFs and bimetal samples as deposited (dashed) and after annealing (solid lines).

4.2.2.2. Electric field-assisted dissolution

Figure 4. *12* shows the compositional profile of the thicker samples treated with 2.5 min EFAD time there is no clear evidence of depleted region formation in glass: most alkali ions show an abrupt change in concentration at the same position as Al. However, a significant amount of Ag is incorporated in the glass matrix, while the distribution of Na in the MIF and SiO_2 layers is reduced. The ratio of Ag and Na quantity in the Au layer with respect to the

quantity in the Ag MIF is larger than in the annealed samples: ([Ag@Au]/[Ag@Ag] is cca. 0.3 in Ag/Au sample and 0.5 in Au/Ag, while [Na@Au]/[Na@Ag]is cca. 1.11 in Ag/Au sample and 1.62 in Au/Ag sample. This increase suggests that once incorporated in Au layer, Na and Ag ion drift is quenched. Indeed, Na and Ag tend to form alloys with Au, improving chemical stability [151, 152]. Regarding the dissolution process, this results in Ag layers losing Ag and Na faster than Au layers.
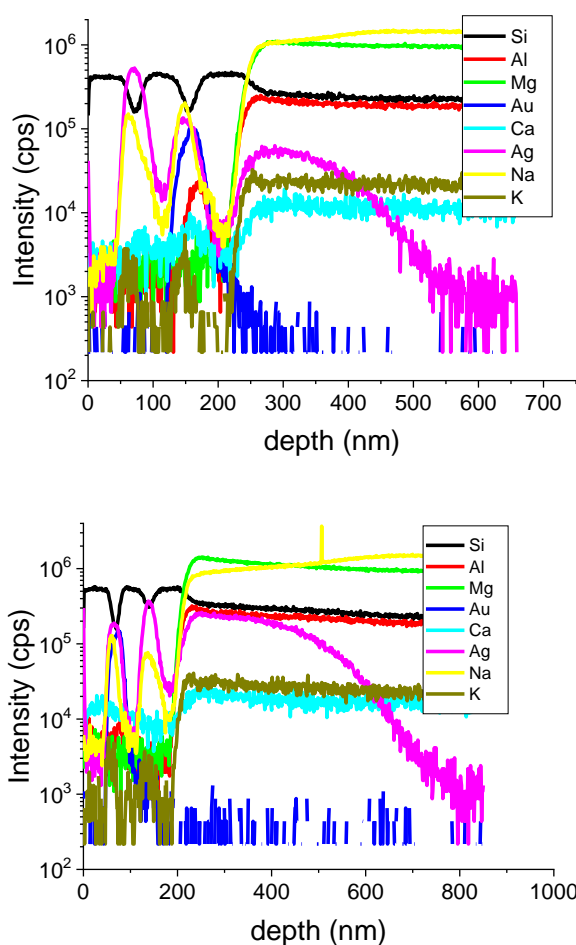
Figure 4. 12. SIMS compositional profile of the thicker bimetal samples (top Au/Ag, bottom Ag/Au) after short EFAD treatment (2.5 min). The interface between the coating and glass is indicated by the steep growth of Al intensity.

Compositional profiles of thicker samples corresponding to longer treatment times are shown in Figure 4. *13*. In both samples, Ag has penetrated deeper into the glass compared to the short treatment times and a region with sequentially piled up Ca, Mg and Au is formed, indicating that Au has mobility comparable to or a bit lower than Mg. Ag penetration and

depth of the pile-up region are larger for the thicker Ag/Au (EFAD time 12 min) than for the thicker Au/Ag sample (EFAD time 5 min). For both samples Na signal reduced to the noise level indicating it has returned back into glass. The Ag layer is completely dissolved, but some quantity of Ag is still present in Au layers confirming that Ag is hardly released once it diffused into Au. In both samples, a plateau of Si and Al at the glass surface is present, while the other samples have a ramp there. The plateau is wider for thicker Ag/Au sample with a longer EFAD time. It indicates densification of the glass matrix occurring due to the transition of non-bridging oxygen bonds of glass formers to bridging, in lack of cations [86, 84, 142]. One should keep in mind that Al is a glass former in soda-lime glass, the same as Si.
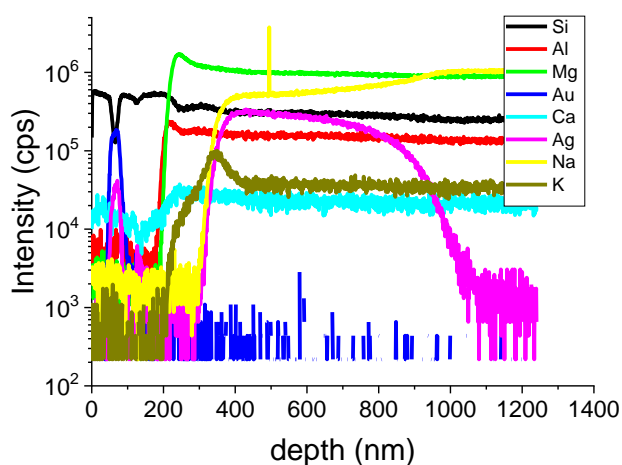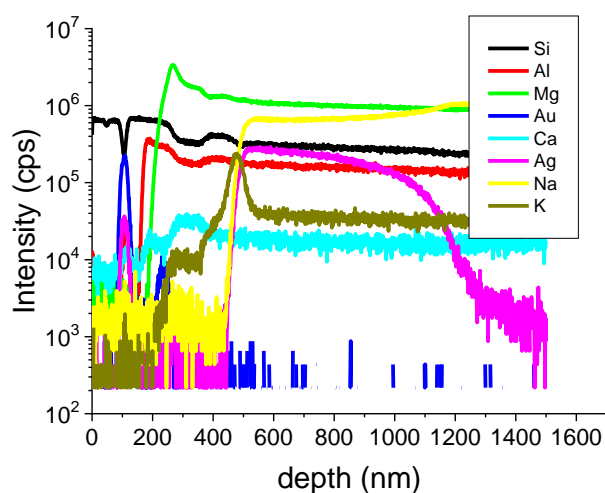
Figure 4. 13. SIMS compositional profile of the thicker Au/Ag sample (top) and thicker Ag/Au sample (bottom) after long EFAD treatment (EFAD time 12 and 5 min, respectively). The interface between the coating and glass is indicated by the steep growth of Al intensity.

To support the evolution of the samples subjected to the EFAD treatment, numerical simulations of the ion drift and diffusion process for multiple ions [83,127] were performed. The system of coupled differential equations describing the concentration depth-profile for each ion species is solved numerically as described in chapter 3. Literature values for ionic mobilities ($\mu_{Na} = \mu_{Ag} = 7 \times 10^{-16}$ m^{2}V/s, $\mu_H = 2 \times 10^{-20}$ m^{2}V/s) and Haven ratio (H = 0.3), initial ion concentration estimated from sample composition ($C_{Na} = 5 \times 10^{27}$ m^{-3}, $C_{Ag} = = 1 \times 10^{28}$ m^{-3} and voltage and temperature values applied in the experiments are used in the simulations. For the sake of simplicity, we consider Na as the only alkali species and that only Ag participates in the drift and diffusion process. Figure 4. *14* (a) shows the initial ion distribution assumed in the simulation, inspired by the SIMS profile of the annealed sample (Figure 4. *10*). It is assumed that Na has diffused into the SiO$_2$ and MIF layers and Ag has diffused into the Au layer and into the SiO$_2$ layer next to the interface with the glass. If blocking conditions are simulated (no injection from H$^+$ ions to compensate spatial charge formation upon drift of Ag and Na ions), the ion distribution displays no appreciable change from the initial composition. Under the same assumption in non-blocking conditions, the final compositional distribution after 15 minutes (Figure 4. *14* b)) shows the incorporation of Ag into the glass matrix and decreased concentration in metal layers. However, the changes are small in comparison to the experimental observation. A suitable explanation is that the ionic mobility in the SiO$_2$ and MIF layers is larger than in glass due to the larger number of defects in thin films than in a glass matrix. Thus, if 5 times larger mobility is assumed for all ions travelling in SiO$_2$ and Ag layers compared to the mobility values in the glass matrix, the obtained distribution (Figure 4. *14* c)) shows a much larger decrease of Ag in the MIFs and Ag incorporation into the glass matrix. Finally, it should be noted that if no ions are assumed to be present in the SiO$_2$ layers (neither Ag nor Na), i.e., if the composition redistribution that takes place due to thermal annealing is ignored, the simulations indicate an almost negligible incorporation of Ag into the glass matrix (Figure 4. *14* d)). Hence, the ion redistribution that occurs during the pre-heating period prior to the application of the electric field is essential to induce the complete dissolution of layers within the considered duration of the EFAD treatments.
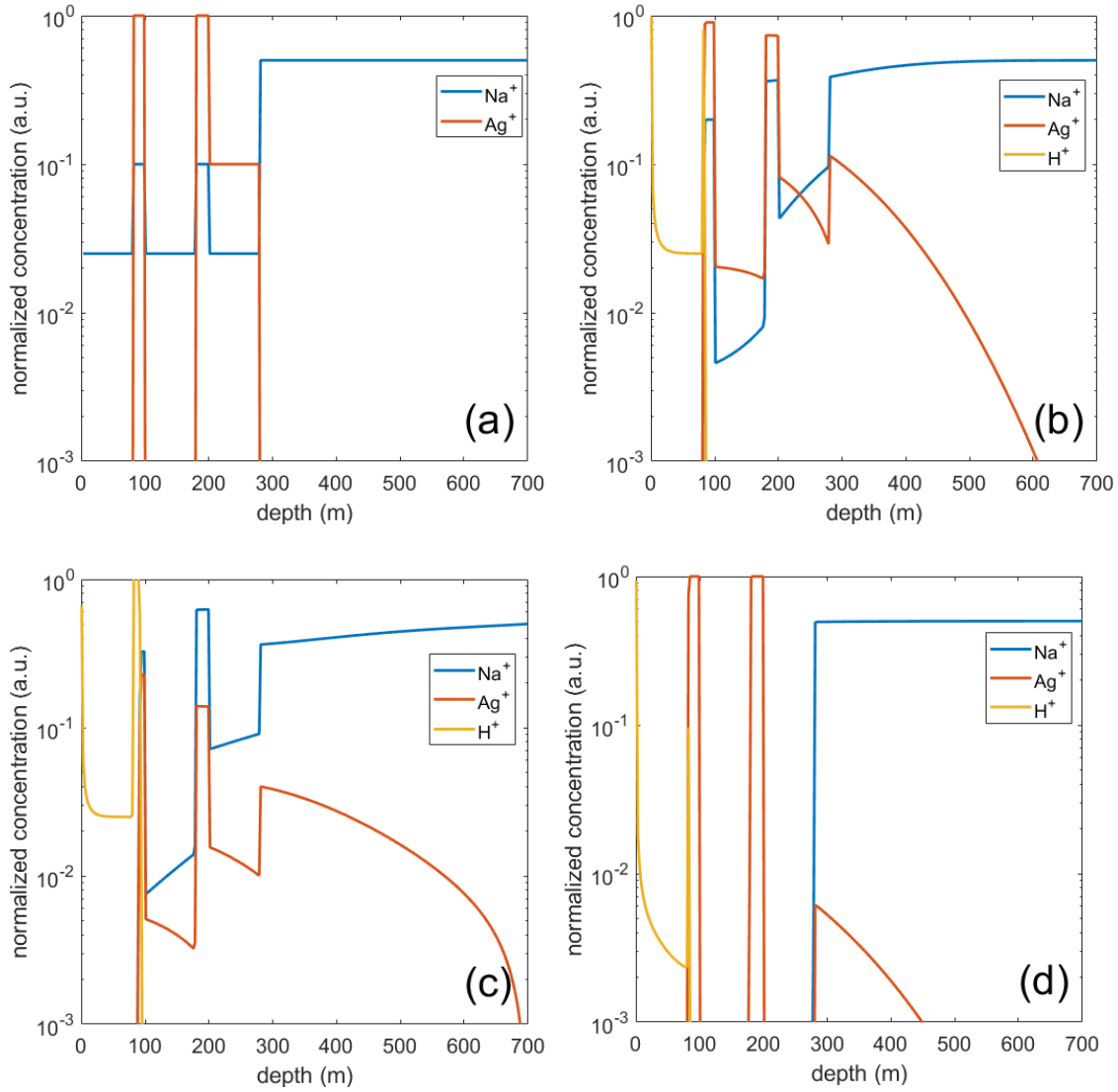
Figure 4. 14.   Numerical simulations of ion drift and diffusion process in non-blocking conditions. Initial concentration assumed for Ag and Na ions (a). Final distribution after 900 s assuming: (b) the same ionic mobility in the glass and in the multilayer structure, (c) 5 times higher ionic mobility in the multilayer structure than in glass and (d) assuming no ions are present in the SiO_2 layers.

It should be noted that the total thickness of the multilayers, as determined by the position of the Al concentration step in SIMS measurements is 30-45% smaller than obtained by optical characterization (Figure 4. *15*). This indicates a higher etching rate in the layers than in glass, especially for the samples with longer EFAD which can be expected because Ag is completely dissolved and instead Ag NPs remain pores [153, 154]. The refractive index profile also reveals a refractive index increase in the glass regions close to the multilayer structure that can be connected to the pile-up of ionic species [155].
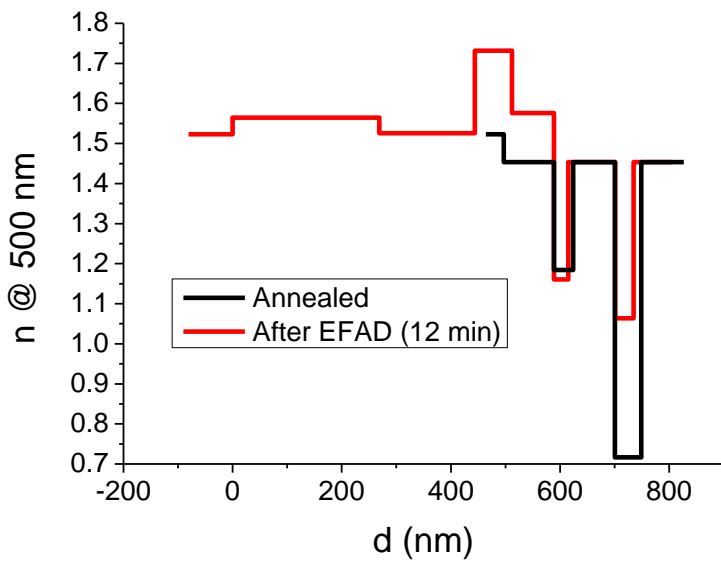
Figure 4. 15. Refractive index profile for thicker Au/Ag sample after annealing and after EFAD with longer treatment time.

Indeed, when refractive index profiles are compared with SIMS measurements, it is possible to see that the increase of refractive index in glass corresponds well with the high signal of Ag that has drifted into glass (Figure 4. *16*, top). Also, in the case of the sample with the longest EFAD, refractive index peak (Figure 4. 16 middle and bottom) is in accordance with the position of alkali ions pile-up.
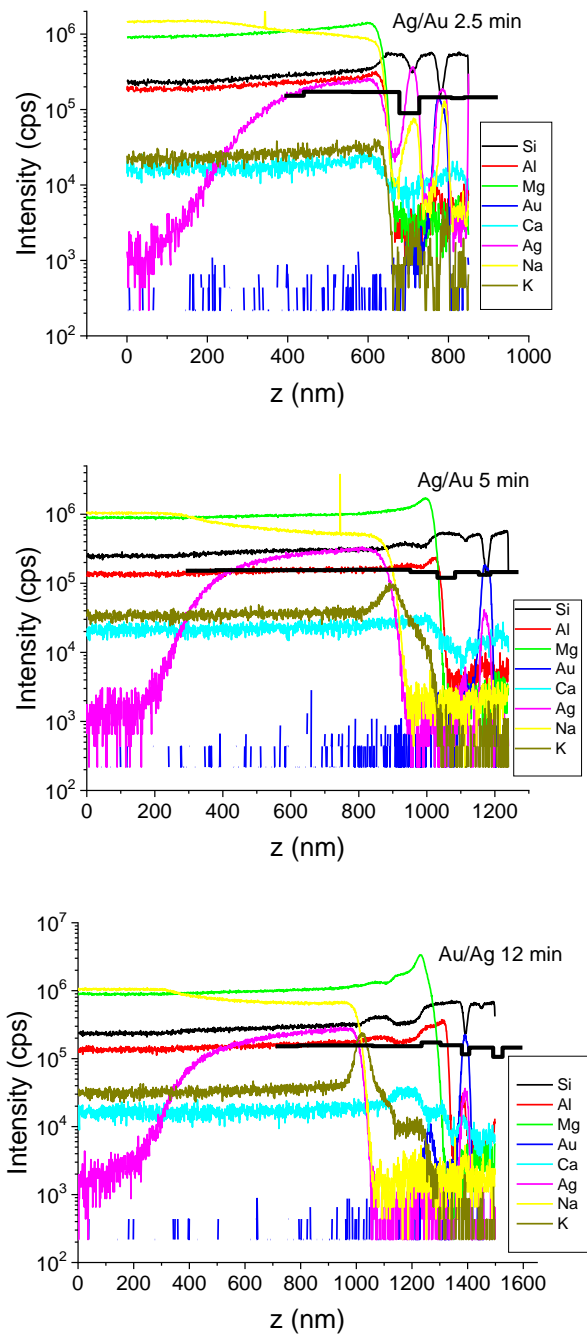
Figure 4. 16. Comparison of SIMS measurements and refractive index profiles obtained from optical characterization. The glass/multilayers interfaces of the two have been adjusted to the same position as the reference point. This is done to compensate for the higher etching rate through the layers. Top: thicker Ag/Au sample treated for 2.5 min. Middle: thicker Ag/Au sample treated for 5 minutes. Bottom: thicker Au/Ag sample treated for 12 minutes.

Finally, it was analyzed the effect on the optical properties of the MIFs upon EFAD (Figure 4. *17*). A short EFAD time results in a blue shift and reduction of the LSPR. This can

be explained by the reduction of Ag fraction into the MIF layer upon partial dissolution of the film. Longer EFAD times lead to the complete dissolution of Ag and the total quenching of Ag-related absorption. In the case of Au MIFs, the plasmon resonance is still present even after a long annealing time, displaying only a slight red-shift and intensity decrease that is in agreement with the fact that Au remains essentially undissolved.
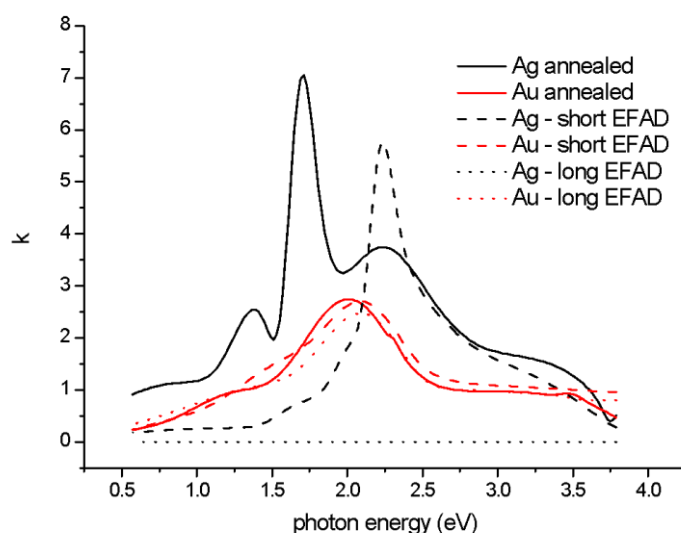
Figure 4. 17. Extinction coefficient for the Ag and Au MIF layers of the thicker Ag/Au sample after annealing and EFAD.

4.3. Filter serial

The aim of the final part of the research is to demonstrate if it is possible to make microarray consisting of three different optical filters using EFAD.

In the first part it was studied poling induced change of refractive index for three types of glass, affecting their optical properties. This part of research was important in order to decide which glass would be the most appropriate as filters substrate. Finally, it was chosen SL glass as the least demanding for optical characterization upon EFAD and with the most predictable refractive index profile.

In the second part simultaneous EFAD of Ag in combination with Au, Al and Cu was studied because the filter will contain MIFs of two metals. It turned out that the most appropriate combination would be Ag with Au. The important findings for this last part of

research are that i) Ag drifts into glass and Au MIF due to IE with Na from glass and that this happens already during deposition, ii) Ag MIF dissolves faster than Au MIF by applied conditions and iii) Ag in Au MIF is not dissolving so easily as Ag from Ag MIF. Also is found that iv) conditions for complete Ag MIF dissolution are not high enough for complete Au MIF dissolution.

Ellipsometric measurements of reflectance are made for R_p at angle of incidence 17.5°. This will not be specified at reflectance figure axes in the next chapters. Also, all simulated reflectance spectra presented there for comparisons with experimentally measured reflectances will be for R_p (17.5°).

As mentioned before, two samples were subjected to both EFAD steps. One of them with micro-structured electrode (just to remind that this electrode has also macroscopic Cr coated and uncoated area as well) - sample H21, and the other one with macro-structured electrode that has a 4 mm wide stripe of bare glass - sample H22. Sample H21, besides microstructure, has 4 macroscopic different areas: not treated with EFAD, treated with EFAD1 and treated with both EFAD1 and EFAD2. The area treated with EFAD2 was not possible to measure because it was too small.

4.3.1.   TFC simulations how EFAD influences filters performance

Upon both EFAD there is no absorption of light in MIF, so in this case the highest intensity of the light beam is reaching the substrate and its influence is the highest. Also, GP induced refractive index changes are the highest in this case. Simulation was made according to [80]. Depleted region thickness was taken 300 nm, its refractive index 1.472 at 550 nm and alkali pile up region thickness 400 nm with refractive index 1.55 at 550 nm. Simulation of GP influence on filters performance is presented on Figure 4. *18*. It can be seen that the difference is negligible.
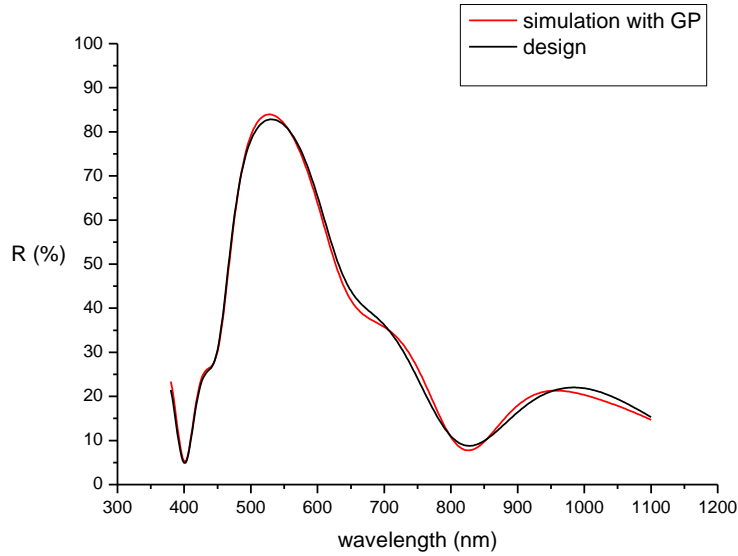
Figure 4. 18. GP influence on filter performance (no MIFs in the layers).

Another check was simulation how Ag ions in glass and SiO_2 layer next to the glass changes optical properties of design: upon EFAD1 there is no Ag MIF anymore, but Ag ions are present in glass. The parameters for simulation were taken according to [19], assuming the same refractive index for doped glass region and the SiO_2 layer: doped region thickness 150 nm with refractive index 1.8. Simulations of Ag ions in glass and SiO_2 layer next to the substrate show lower shoulder of R in red part of spectrum. Discrepancy between two reflectances is higher in infrared part that is not important since the filter is designed for visible part of spectrum (Figure 4. *19*).
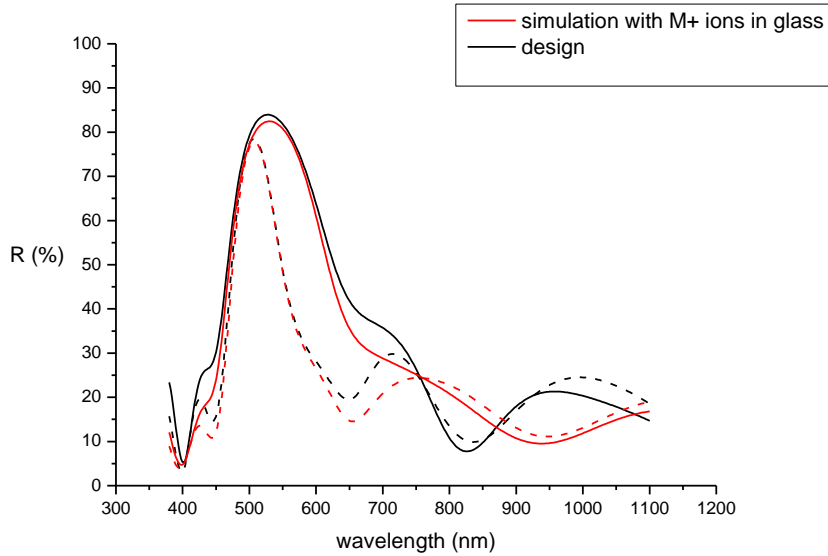
Figure 4. 19. Influence of Ag ions doped into glass and the first SiO_2 layer. Dotted lines present the case upon dissolution of Ag MIF and full lines upon dissolution of both MIFs.

Finally, it is assumed in the design that upon EFAD MIF collapses, i.e. that the thickness of the layer becomes zero. However, due to some previous studies [156], dissolved NPs leave pores in dielectric matrix after dissolution. Simulation of the influence of pores instead metal NPs changing optical properties of the design were done according to [40]: 70 Å Ag at hot corresponds to 4.7 nm mass thicknes that gives 27% filling volume of Ag. Therefore, porous layers are simulated using EMA material with refractive index 1.38 at 550 nm, corresponding to 27% voids in SiO2 assuming that half of the pores are filled with water due to humidity of air). Simulations of MIF layers replaced by porous layers show that reflectance maximum is slightly shifted towards red and again is obtained lower shoulder in red part.
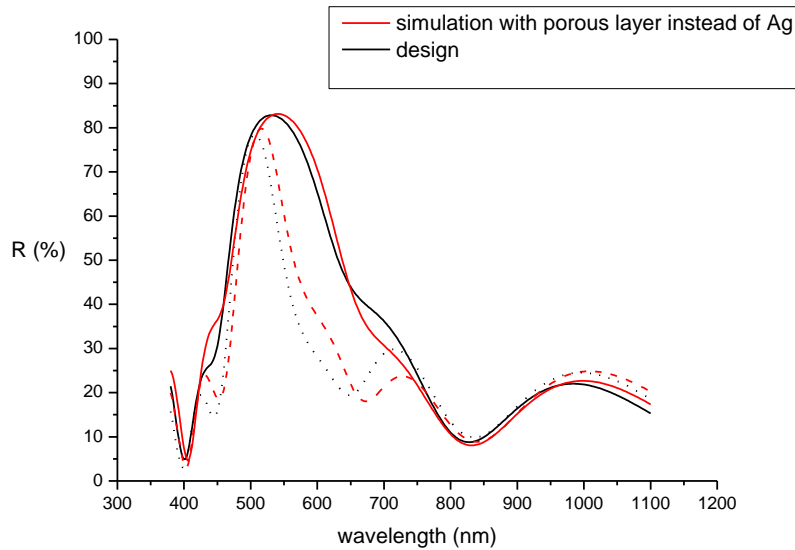
Figure 4. 20. Influence of porous layers replacing MIF upon EFAD. Dotted lines present the case upon dissolution of Ag MIF and full lines upon dissolution of both MIFs.

From this analysis is concluded that changes of refractive index in glass caused by depletion or pile up of alkalies upon GP, or by Ag ions upon EFAD, same as possible porosity in MIF layers upon EFAD, are not affecting optical properties in the visible part of the chosen design significantly. This means that the designed filter is not sensitive to the mentioned effects of GP and EFAD and there is no need to refine it, but the design could be deposited as it is.

4.3.2.   Analysis of as deposited samples

Figure 4. 21. presents photos of as deposited samples as follows: MIF part with SiO_2 underlayer (C) on soda-lime (m) and Si wafer (w), HL part (B) and the complete filter (A). Photos are taken at nearly normal incidence.

94
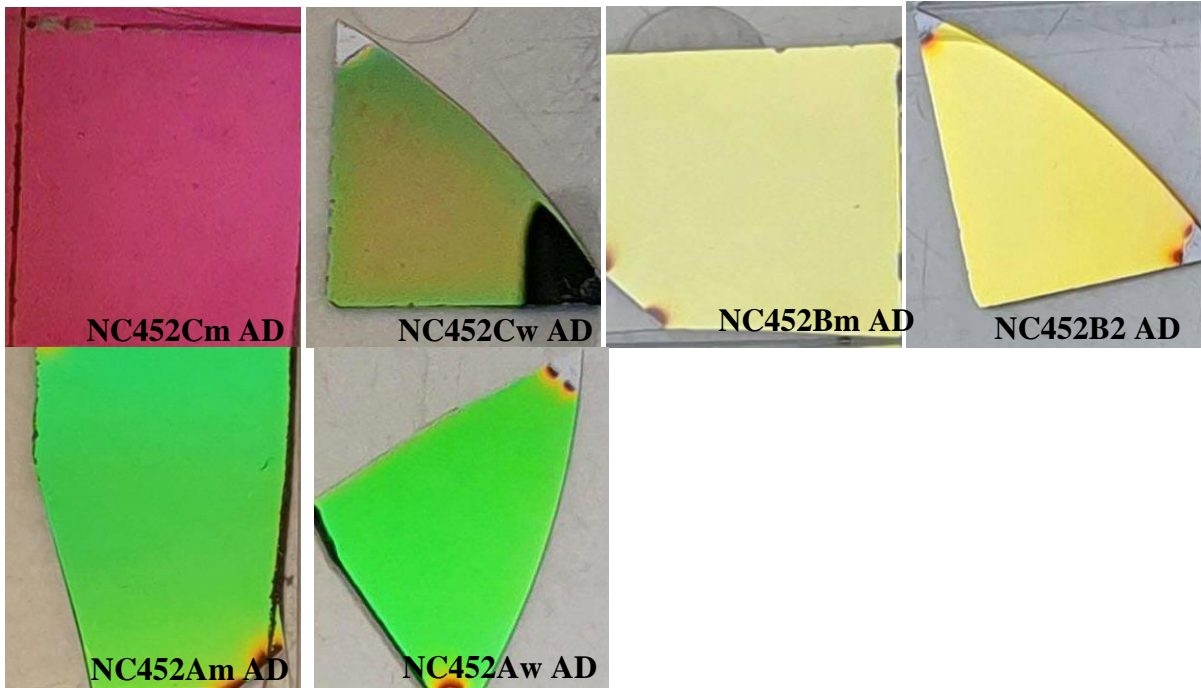
Figure 4. 21. Photos of AD samples: MIF part (C samples), HL part (B samples), complete filter (A samples) on SL (m samples) and Si (w samples).

According to the design, the simulated reflectance of Cm should be blue, Cw pink (not shown), HL part yellow and of the complete filter orange. There are obvious discrepancies of the deposited samples from the expected colours. For this reason is necessary to make analysis of the deposited samples and find the origins of the difference with the design.

HL sample on SL substrate (Bm)

Optical characterization of B sample on SL showed that the deposited thicknesses of dielectric layers are up to 13% higher than in design. Thicker layers result in shift of the spectra towards longer wavelengths (Figure 4. *22*, right). The origin of discrepancy is the difference of the thickness value read out at quartz monitor and the real deposited thickness (in other words, tooling factor was not well determined). Since the errors in deposition are out of the scope of this study, as reference optical properties will be taken those of the refined design, i.e. design with thicknesses obtained from optical characterization of samples B and C on glass.

The spectra of the refined design are shifted towards longer wavelengths and reflectance maximum is somewhat lower than the initial one. However, there is still clear difference in spectra of the system with both MIF layers, without Ag MIF and without MIF layers (Figure 4. *22*). Therefore, the deposited samples can be used for demonstration of micro-structuring with EFAD.

complete filter			no Ag MIF			no Ag, Au MIF		
	Refl	Trans		Refl	Trans		Refl	Trans
x Coordinate:	0.357	0.310	x Coordinate:	0.191	0.232	x Coordinate:	0.393	0.284
y Coordinate:	0.302	0.201	y Coordinate:	0.499	0.186	y Coordinate:	0.478	0.211
Luminosity (%):	12.60	10.50	Luminosity (%):	24.34	18.88	Luminosity (%):	66.05	30.97
Dominant (nm):	N/A	N/A	Dominant (nm):	511	462	Dominant (nm):	569	N/A
Complementary (nm):	495	551	Complementary (nm):	N/A	571	Complementary (nm):	449	562
Excitation Purity:	0.144	0.465	Excitation Purity:	0.410	0.460	Excitation Purity:	0.656	0.375

Figure 4. 22. Comparison of design and sample reflectance (up, left), reflectance of the initial (dash) and refined design (full line) depending on MIFs presence (up, right) together with corresponding colours of the refined design (bottom).

Complete filter (Am, Aw)

Visual inspection showed colour non-uniformity among Am samples. The sample that looked the most non-uniform was chosen to test the effect of the layers thickness uniformity of the samples. Figure 4. 23. presents reflectance measurements at three positions along the surface of the same sample. The minimum around 674 nm shifts within 8 nm while its reflectance shifts 2%. At the same time the maximum around 754 nm shifts within 12 nm while its reflectance shifts 2% as well. Non-uniformity was not detected on other samples. This indicates that its origin might be too short time of substrates pre-heating: SL substrates are thicker and somewhat bigger than Si chunks and might not have been uniformly heated. Growth and optical properties of MIF strongly depend on substrate temperature. Also, IE process depends on the temperature. Am samples contain MIFs so in both cases non-uniform temperature of the substrate could result in non-uniform MIF properties and colour.

For the purpose of EFAD, i.e. to be able to fit the sample into the EFAD holder, AD samples were cut into two halves, so the maximum or minimum shift across the cut sample that can be ascribed to thickness non-uniformity over the same chunk should be not higher than 4-6 nm.
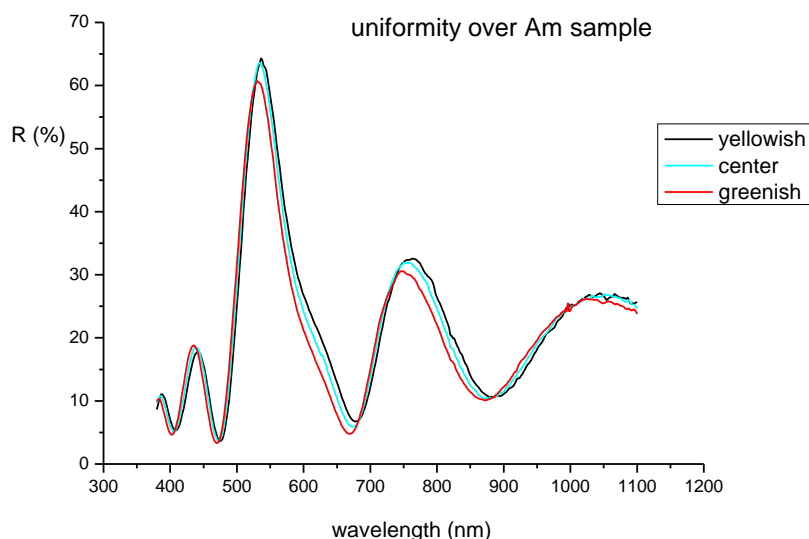
Figure 4. 23. Reflectance spectra measured at three points over the surface of non-uniform Am sample.

There is still clear difference between the colour of the refined design (pinkish) and A samples at both substrates (green) and reflectances (SL substrate Figure 4. 24). The samples reflectance resembles to the one of the design without Ag MIF in the system. Indeed, as a result of optical characterization of Aw (samples on Si wafer - to exclude the possible influence of IE with glass), it is obtained that Ag SPR is much weaker in A sample than C (Figure 4. 25). As C sample does not contain TiO_2 layers, but samples A do, lower Ag SPR in A samples than in C samples may indicate migration of Ag ions into TiO_2 layers in A samples already during deposition.
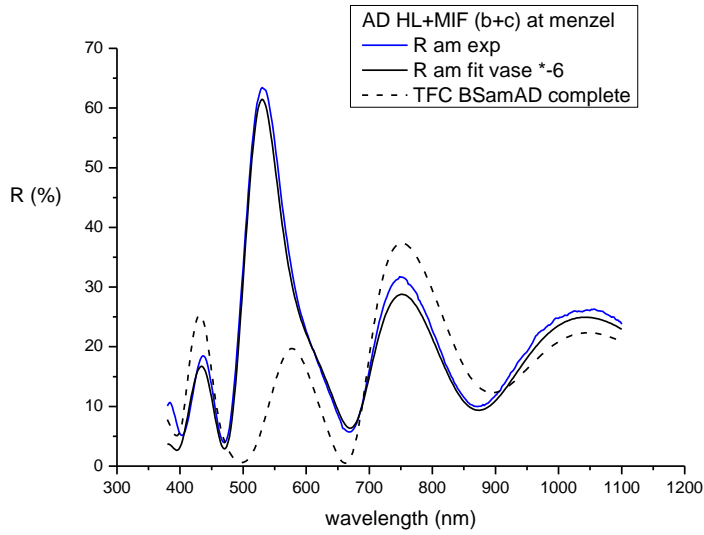
Figure 4. 24. Measured, fitted and refined design (taking into account the thicknesses of deposited dielectric layers) reflectance.
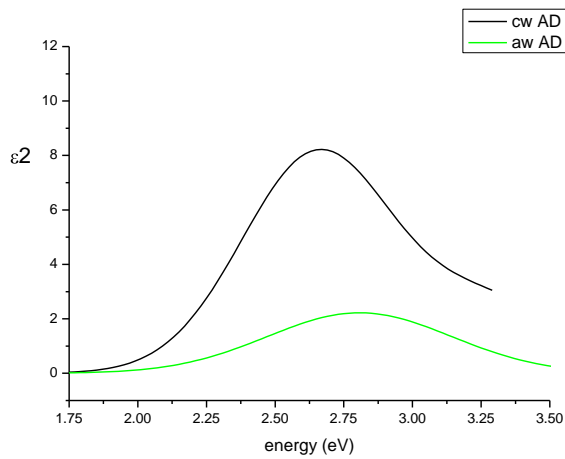
Figure 4. 25. Comparison of Ag MIF LSPR in Aw and Cw sample.

Au SPR is also slightly weaker in A samples than in C, regardless of substrate, suggesting possibility of low migration of Au ions into TiO_2 as well (Figure 4. 26.).
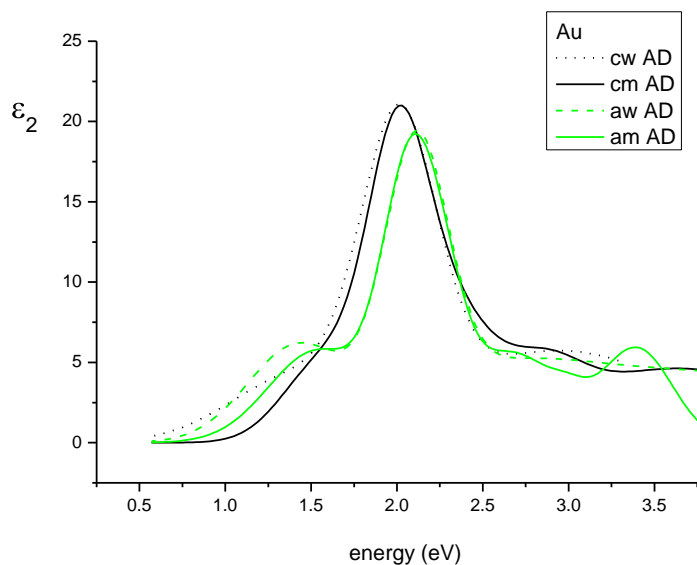
Figure 4. 26. Comparison of Au MIF LSPR in A and C samples.

4.3.3.   Analysis of Am samples upon EFAD (H20, H21) - EFAD repeatability and additional annealing

Repeatability of optical properties obtained upon EFAD1 (the shorter one) is very good, that is confirmed by comparison of reflectance spectra of two Am samples, both treated with 200/500/15 min (Figure 4. 27). It is possible to see that with these conditions spectrum changes mainly in the range 650-750 nm. The change is a consequence of Ag dissolution: the applied conditions are too weak for significant dissolution of Au and, as mentioned before, due to diffusion of Ag into TiO_2 layers, the initial quantity of Ag in MIF is already too low to change the spectrum drastically upon Ag dissolution.

99
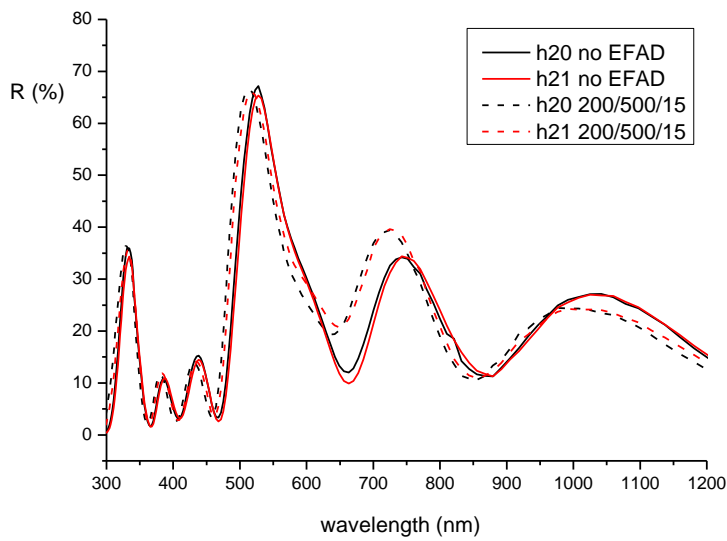
Figure 4. 27. Repeatability of optical properties upon EFAD1.

The effect of the annealing upon EFAD2 (stronger conditions: 300/500/1) was tested by reflectance measurements of the areas with and without Ag MIF that were not treated during the second step (samples H21 - treated by EFAD1 and H21-2 - treated by EFAD 1 and EFAD2). The spectrum changes more in the first than in the second step. The spectra shift slightly towards shorter wavelengths upon annealing during EFAD1 (Figure 4. 28). This shift does not have to be crucial for the filters performance.
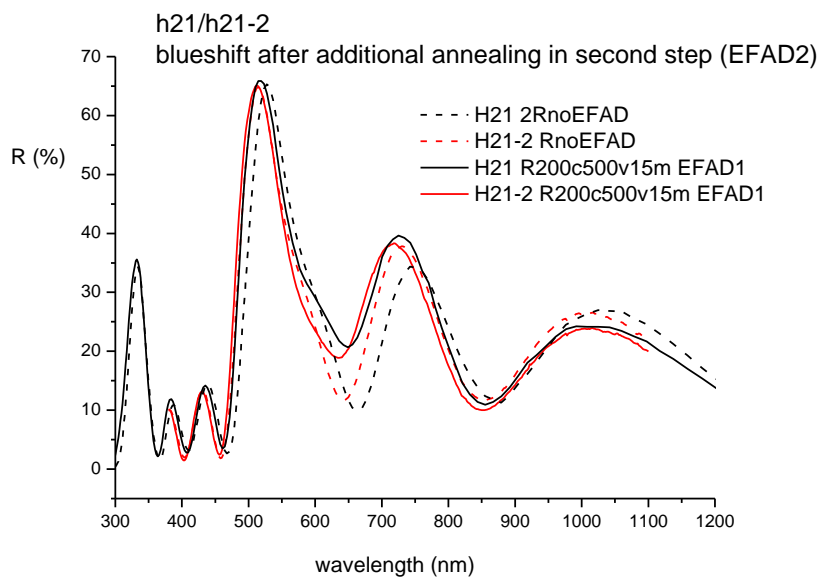
Figure 4. 28. Effect of annealing during EFAD process. Dash lines present reflectance of samples area that was not treated in any EFAD step, but only annealed: black line is

measurement after EFAD1 and red line after both EFAD (EFAD12). They present effect of annealing to the not treated area. Full lines present reflectance of samples area that was treated in EFAD1 (black line) and only annealed in EFAD2 (red line). They present the effect of annealing to the area without Ag MIF.

4.3.4.   Macro-structured filter (H22-2)

Experimental results

After two EFAD steps the sample has four areas: i) not treated, 2) treated only in first step (EFAD1), iii) treated only in the second step (EFAD2), iv) treated in both steps (EFAD12). All 4 areas have distinct reflectance spectra, but none of them corresponds to the one without metal. This means that Au was not completely dissolved. However, from the design reflectances, it is expected that the main peak widens as Au quantity in the system is reducing. Indeed, this is visible in the presented spectra in Figure 4. *29*.
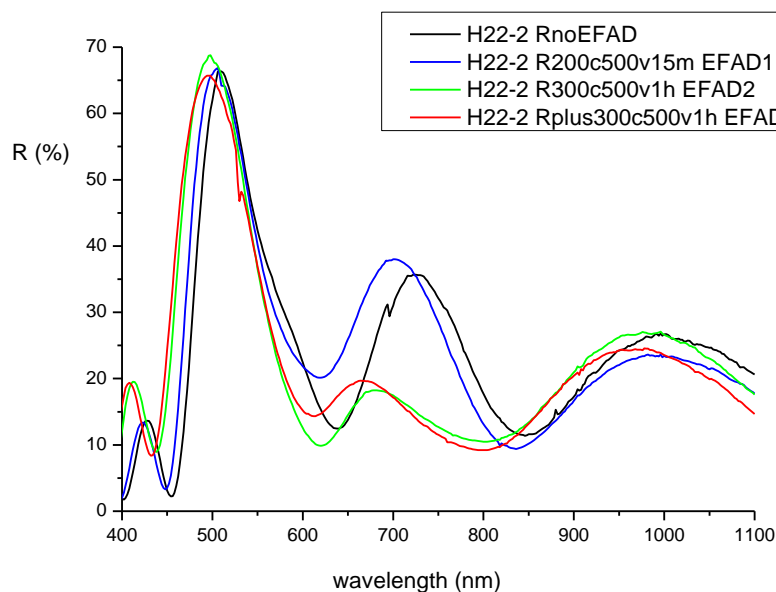
Figure 4. 29. Reflectance spectra of four areas of the filter: not treated (black), treated with EFAD1 that dissolved Ag MIF (blue), treated with EFAD2 that has partially dissolved Au MIF (green) and treated with EFAD1 and EFAD2 that dissolved Au MIF more (red).

Besides widening, the peak around 530 nm is 8-9 nm shifted towards blue after EFAD1 and after EFAD2 the shift is 25 nm in the same direction. This shift is not expected as the

corresponding reflectance peak of design is not shifting with decrease of metal quantity in MIFs. It only gets wider with its left side remaining aligned at the same position.

Results of optical characterization

In Figure 4. *30* is possible to see the fits for the most treated and therefore the most demanding sample area: H22-2 EFAD12. The fits are in very good accordance with the experimental results. Corresponding refractive index profile is presented in Figure 4. *31*, and refractive index profile of the AD sample on glass is in Figure 4. 32 for comparison. It is seen that upon EFAD12 Ag MIF layer is replaced in the model with the layer of the same thickness but with a refractive index lower than the one of SiO_2, suggesting pores in the layer. EFAD12 conditions result in refractive index peak in glass that is characteristic of alkali ion pile-up. Extinction coefficient (k) of Au MIF have reduced, but not vanished upon EFAD12.
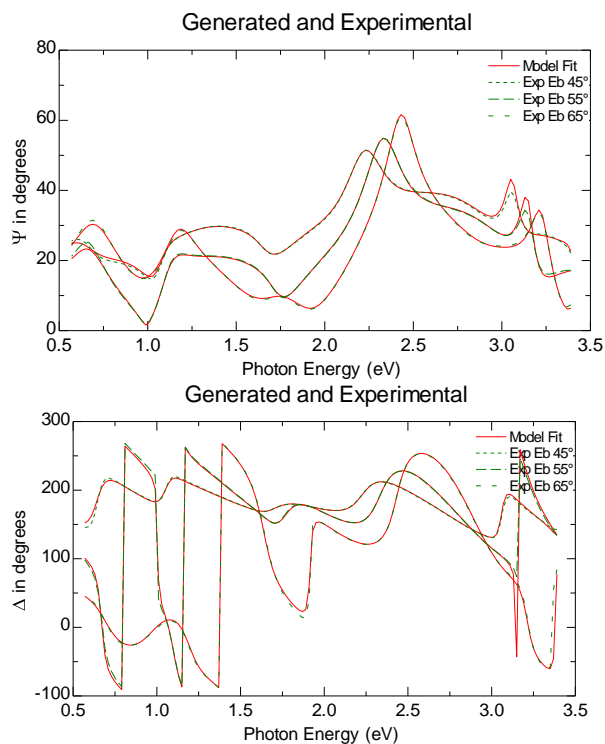
Figure 4. 30. Fits to the measurements of H22 area that was treated in both EFAD steps (H22-2 EFAD12)
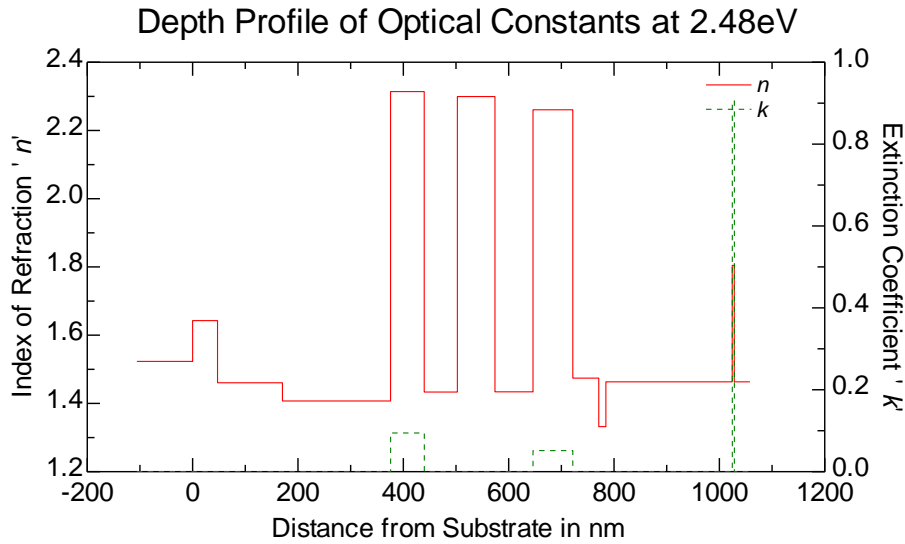
Figure 4. 31 Refractive index profile of H22 area that was treated in both EFAD steps (H22-2 EFAD12). The profile is obtained from optical characterization.
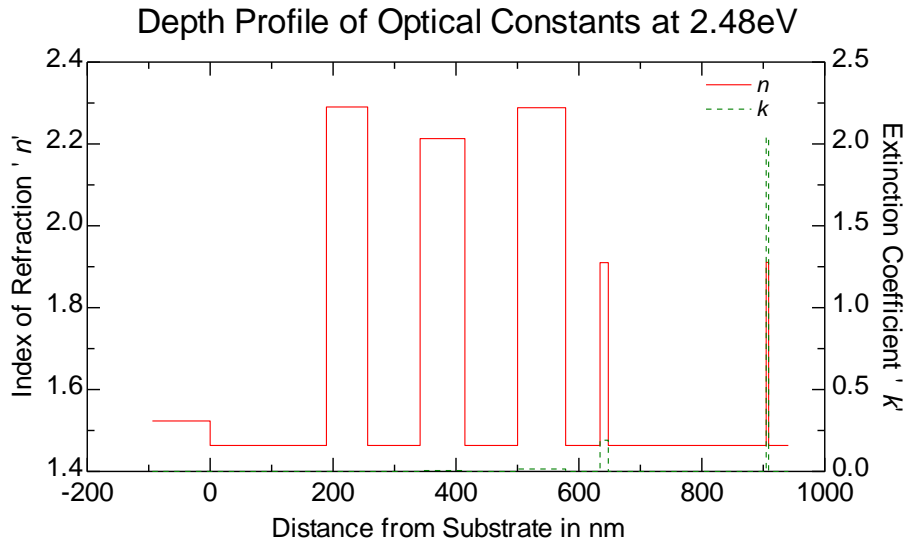
Figure 4. 32. Refractive index profile of the AD sample on glass (Am sample). The profile is obtained from optical characterization.

The next graph (Figure 4. 33) presents evolution of Au MIF ε_2 with EFAD obtained from oc. It is visible that plasmon intensity is reducing with EFAD, as expected. Effect of annealing for Au SPR is also interesting. In AD sample shoulder that was in simultaneous EFAD serial ascribed to diffusion of Ag into Au is formed already after deposition. After annealing in the first step, and more in the second, it grows as more Ag that is still left in the Ag MIF layer drifts into Au. The shoulder is decreasing with EFAD, same as the main peak indicating that although all Ag from Ag MIF has dissolved in the first step, there is still

enough of it in Au MIF to make difference in LSPR. It is interesting that the shoulder is not so efficiently decreased solely by EFAD2, as by combination of EFAD1 followed by EFAD2. It turns out that Ag in Au, or Ag/Au alloy MIF, can be used for tailoring optical properties of the devices operating in IR, as it is easier to control dissolution of Ag in Ag/Au alloy than in pure Ag MIF.

In the case of Ag MIF, Ag vanishes from its layer already after the first step. (Figure 4. *34*) It is possible to see strong influence of annealing in the first and second step decreasing the plasmon intensity. This is in accordance with the growth of shoulder in Au SPR presented before.
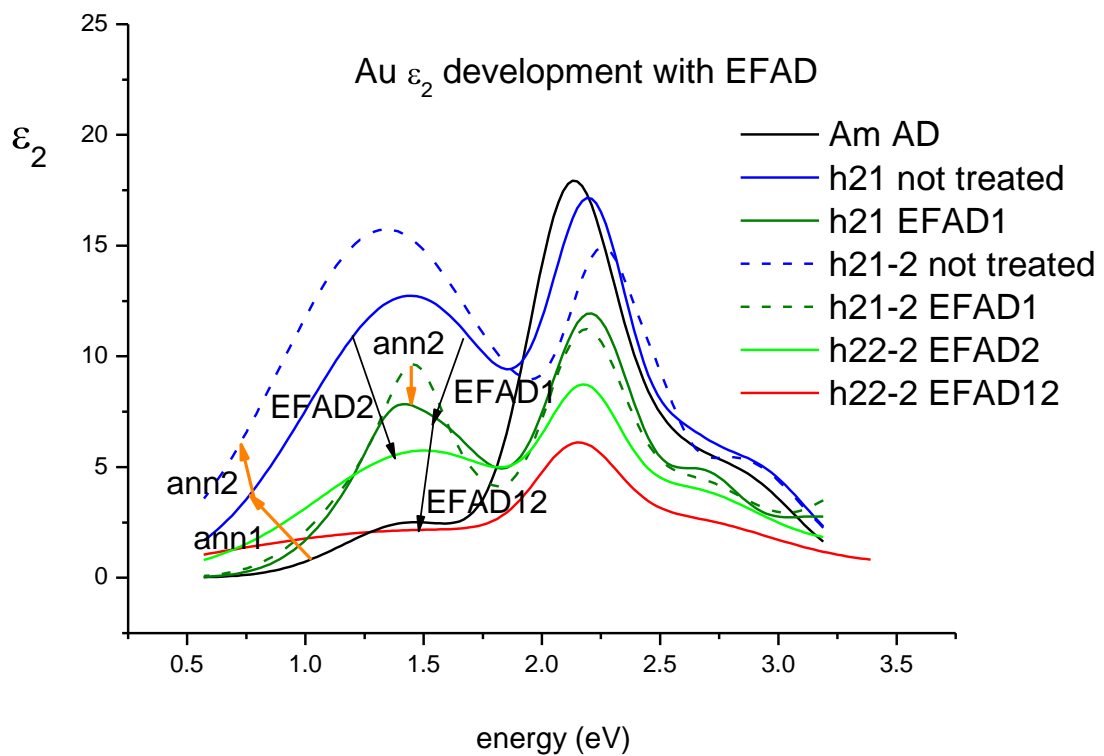
Figure 4. 33. Evolution of Au MIF ε_2 with EFAD (black arrows) and annealing (ann, orange arrows) obtained from oc.
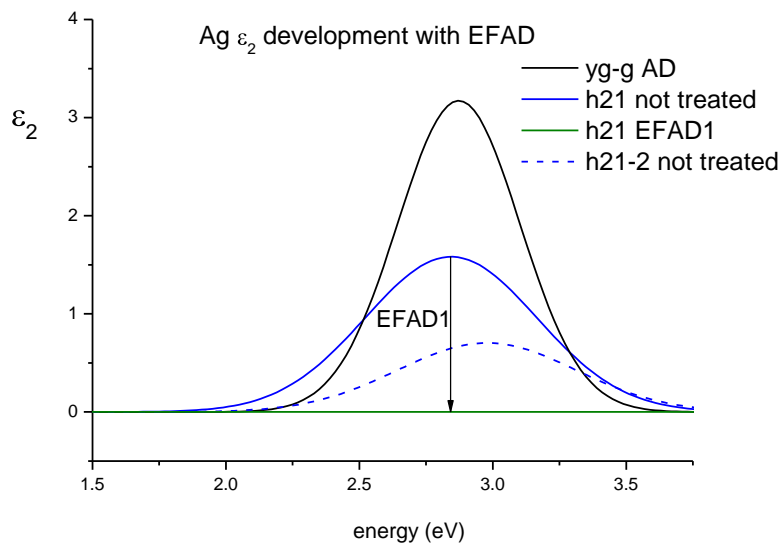
Figure 4. 34. Evolution of Ag MIF ε_2 with EFAD obtained from oc.

What is the origin of the unexpected blue shift of the peak around 530 nm? EFAD reduced Au LSPR is responsible for the changes in reflectance intensity, and colour shift from green to yellow, but not for the main peak shift, as is shown in Figure 4. 35.
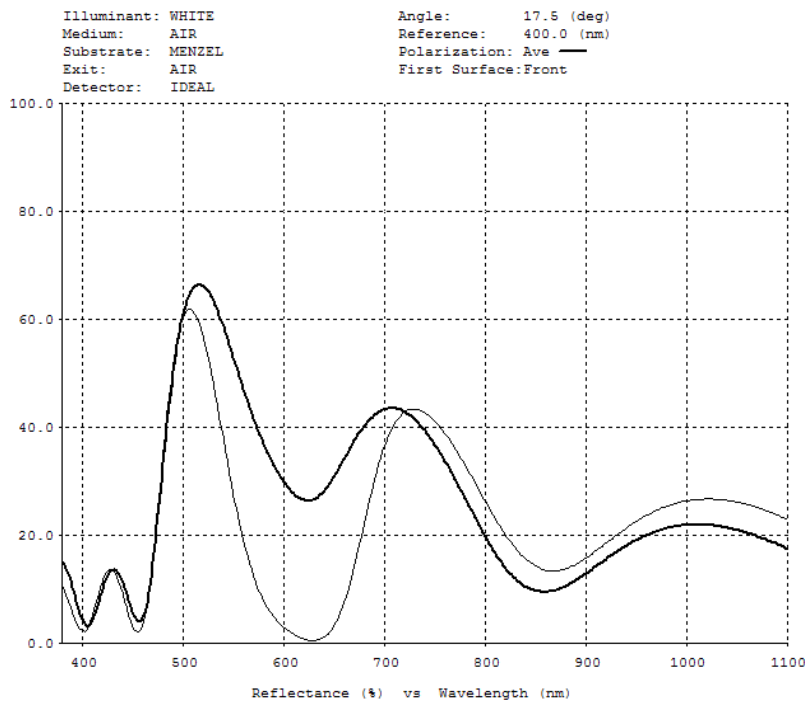
```
                    Refl   Trans                            Refl   Trans
x Coordinate:       0.191  0.232       x Coordinate:        0.338  0.267
y Coordinate:       0.499  0.186       y Coordinate:        0.489  0.198
Luminosity (%):     24.34  18.88       Luminosity (%):      45.59  24.91
Dominant (nm):        511    462       Dominant (nm):         559    N/A
Complementary (nm):   N/A    571       Complementary (nm):    N/A    565
Excitation Purity:  0.410  0.460       Excitation Purity:   0.543  0.400
```

Figure 4. 35. The effect of reduced Au LSPR: thin line is reflectance of design without Ag MIF and with Au LSPR from AD sample on glass, and thick line is design with Au LSPR obtained from oc of H22-2 EFAD12 sample, with corresponding colours (left and right, respectively).

The shift cannot be explained by annealing either, because the whole sample has passed the same annealing cycles. Also, it is not a consequence of formation of the depleted region in glass, or slight increase of n in glass due to doping with metal ions as these effects do not change reflectance spectra significantly (this was checked by simulations, but also after oc. by including the found values of refractive indices and thicknesses into the design). Also, replacing Ag MIF with the low refractive index layer obtained from optical characterization is not contributing to this shift (in fact, it is almost not changing the reflectance of the design at all). Higher TiO2 refractive index obtained in optical characterization reduces peak intensity for 3%, but also does not explain the shift.

Therefore, the shift should be related to the changes that EFAD is making in dielectric layers. It could be expected that EFAD changes the structure of the layers in different ways. This issue should be studied separately. Optical characterization results show reduced thickness of SiO_2 layers situated between TiO_2 layers: the reduction of thickness is 16 and 26%. Indeed, when these layers thicknesses are included in the design only (so nothing else is changed compared with the original design), the main peak shifts to the proper position. However, due to the high number of parameters in the numerical optimization, it is possible that thickness of these SiO_2 layers have reduced trying to compensate some other dielectric layer parameter. Therefore, analysis based only on ellipsometry data cannot give a unique answer that could ascribe the change in reflectance to one of the mentioned options.

Figure 4. *36*. presents the effect of two main contributions to the spectral change upon EFAD12: the first is the effect of "thinner" dielectric layers keeping in mind that thinner layers are the result of optical characterization, but some other modifications of dielectric

layer properties cannot be ruled out merely from optical characterization). So, the change in dielectric layers results in blue shift, in accordance to the experimental results. An indeed, the filter colour shifts from green to blue. The other is the effect of Au dissolution, i.e. weaker Au SPR: the main peak is wider and the minimum to its right is higher.

the main contributions to the spectral change upon EFAD

Legend:
— H22-2 Rplus300c500v1h EFAD12
···· Am filter no Ag
— Am filter with "thinner" layers
— Am filter with "thinner" layers and AuSPR upon EFAD12
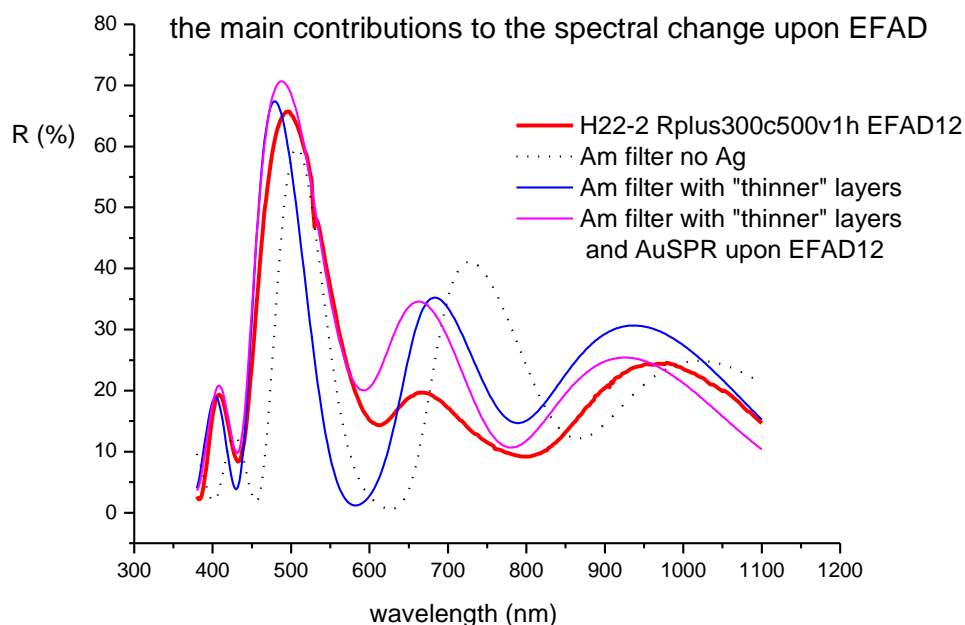
	Refl	Trans			Refl	Trans
x Coordinate:	0.185	0.304		x Coordinate:	0.268	0.340
y Coordinate:	0.254	0.213		y Coordinate:	0.352	0.237
Luminosity (%):	16.65	19.89		Luminosity (%):	37.20	28.92
Dominant (nm):	485	N/A		Dominant (nm):	501	N/A
Complementary (nm):	587	554		Complementary (nm):	N/A	525
Excitation Purity:	0.521	0.405		Excitation Purity:	0.140	0.375

d   d and Au LSPR

Figure 4. 36. The effect of two main contributions (dielectric layers modification and Au LSPR quenching) to the spectral change upon EFAD12.

4.3.5.   Micro-structured filter (H21)

The patterned anodic electrode surface has different parts: (i) a 500 nm thick chromium layer (ii) a part of Cr layer etched into a pattern with 25 μm wide chromium stripes separated by 10 μm wide and 500 nm deep grooves having bare glass bottoms and (iii) an uncoated part - bare BK7 substrate.

Sample H21 is treated using microstructured chromium electrode. The sample was treated twice: first with 200/500/15min (weaker conditions of EFAD) in one orientation of the electrode grating, and second time with 300/700/1h (stronger conditions of EFAD) with the grating oriented perpendicularly to the initial orientation. As the electrode has three parts, the sample has different macroscopic areas besides the microstructure: not treated, treated with weaker conditions, treated with stronger conditions and treated with both conditions. The obtained micro-structure is presented in Figure 4. 37 and Figure 4. 38.
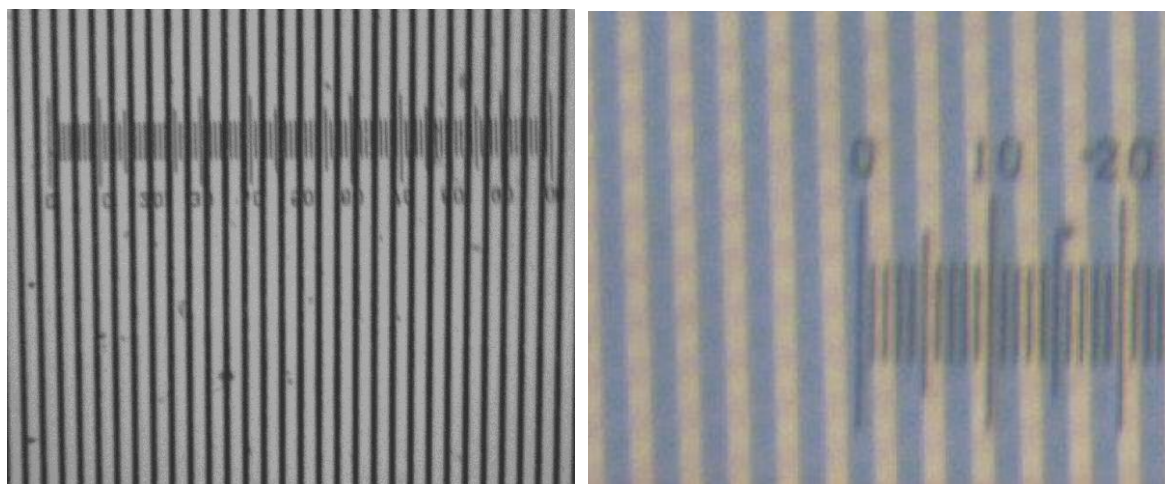
Figure 4. 37. Optical microscope image of micro-patterned anode (left) and micro-structure obtained after two EFAD steps (right). Both micrographs are made in transparency mode. The distance between the lines on the rule is 10 μm.

The next microscope image presents the obtained microstructure in reflectance mode (Figure 4. *38*). One has to keep in mind that colour appearance depends on the camera gains for each RGB channel and therefore do not necessarily have to correspond to the real colours. However, they illustrate well the areas with different reflectance. Stripes with yellow and green areas correspond to dark stripes in transmittance mode, indicating the highest content of metal in MIFs (non-treated and treated with EFAD1, respectively). Pale bluish squares correspond to areas with highest transmittance (EFAD12), where dissolution should have been the strongest. From geometry and orientation of the anode, the green areas correspond to dissolution in weaker conditions (EFAD1), and blue in stronger (EFAD2). This area colours are in accordance with simulated spectra: green square corresponds with the designed filter without Ag (the last fig of first section), yellow square with colour of filter with reduced Au plasmon, as indicated in Fig.4 that in this case colour shifts towards yellow, blue square with colour of the design with changed dielectric layers (Fig. 10 d) and finally pale blue with

design where also Au LSPR is weakened (Figure 4. *36*, thinner *d* and Au LSPR quenching). The reflectances obtained at different areas of microarray are thus related with optical properties of the analyzed macro-structured sample, same as with simulations of the EFAD caused changes that have the highest influence to the obtained spectra (Figure 4. *39*).
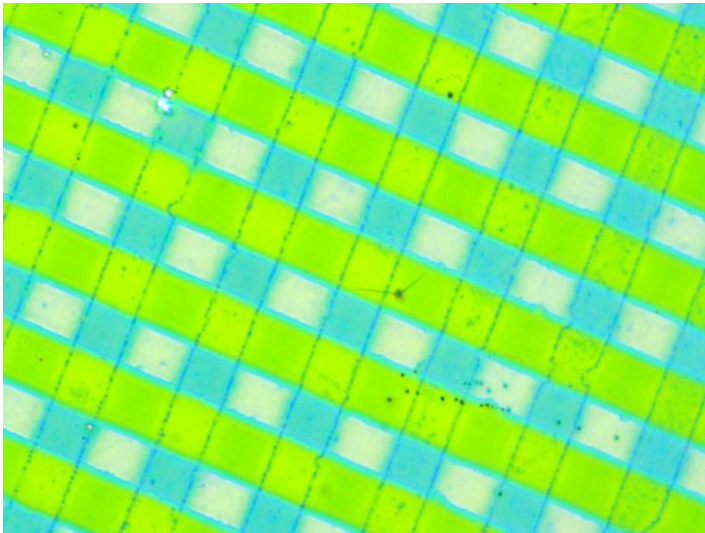
Figure 4. 38. Optical microscope image in reflectance mode of micro-structure obtained after two EFAD steps (right).

EFAD12	EFAD2	EFAD12	EFAD2	EFAD12
EFAD1	noEFAD	EFAD1	noEFAD	EFAD1
EFAD12	EFAD2	EFAD12	EFAD2	EFAD12
EFAD1	noEFAD	EFAD1	noEFAD	EFAD1
EFAD12	EFAD2	EFAD12	EFAD2	EFAD12

Figure 4. 39. Schematic presentation of the obtained micro-structure and the treatments at specific fields.

Spectra of the fields taken by microspectrophotometer are presented in *Figure 4. 40*. It is possible to see four different types of spectra, corresponding to different fields at the

microstructure. Within each group, there are discrepancies among spectra, which can be explained by the difficulty in positioning the sample in order to avoid contribution from neighbouring fields that were subjected to different EFAD. There are evident differences between the spectra of the macro-structure (measured with the ellipsometer) and the microstructure (measured with the microspectrophotometry). In the second case, a Si wafer was used as a reference and therefore the relative reflectance values can surpass 100%. In addition, since the absolute reflectance of Si wafer increases with reducing wavelength, it can be expected that the relative reflectance spectra of the microstructure are shifted with respect to the absolute reflectance measurements of the macro-structure. Additionally, it should be noted that an objective with 60x (NA equal to 0.85) was used for measurements of the microstructure, meaning that some contribution from light reflected at large angles of incidence can occur. In this sense, it cannot be expected a full agreement between the peak positions of both types of reflectance measurements.

However, comparing positions of the measurements at microstructure and spectra from macro-structure (Figure 4. *29*), it can be identified that spectra with peaks around 500 and 700 nm correspond to the fields that were not treated (measured at yellow field), 500 nm and 670 nm treated with EFAD1 (measured at green), 490 nm and 660 nm treated with EFAD2 (measured at blue) and 490 nm and 650 nm treated with both EFAD (measured at pale blue). This is in accordance with the optical microscope image of the sample (Figure 4. *38*) and previous identification of the treatments for specific field of micro-structure.
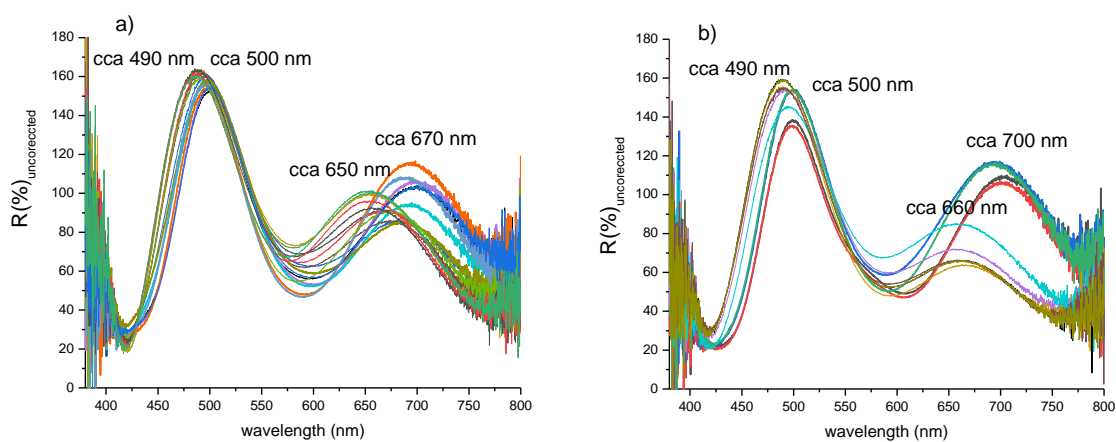
Figure 4. 40. Spectra taken at different fields of microstructure (uncorrected to reflectance of the reference Si wafer).

The initial assumption was that only three different areas would be obtained as it was planned that only one metal will remain after EFAD1 and it would be completely dissolved upon EFAD2. In this case, dissolution in blue and green areas would be the same, resulting in the same colour. However, since Au MIF properties depend on the number of EFAD steps and not only on the strongest applied, four different areas are obtained. This result makes the final performance of the filter array more complex to predict. However, it opens the door for finer control of the fabricated micro-structure properties.

4.3.6. Profilometry results

The surface profile of sample H21 was measured in two perpendicular directions: direction of microelectrode lines during EFAD1 and direction during EFAD2. In both cases profiles were taken in two parallel adjacent stripes, altogether resulting in 4 profiles. Profiles for direction of microelectrode lines during EFAD1 (contact in EFAD1 dark-dark line and no contact in EFAD1 dark-white line) are presented in *Figure 4. 41* and during EFAD2 (no contact in EFAD2 dark-dark line and contact in EFAD2 dark-white line) in Figure 4. *42*.

EFAD1 (contact) dark-white line
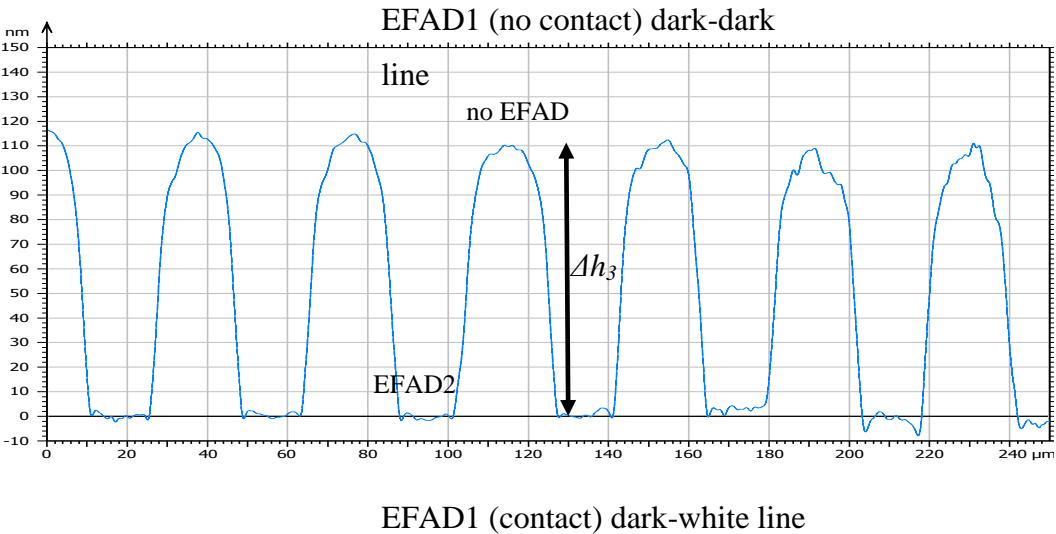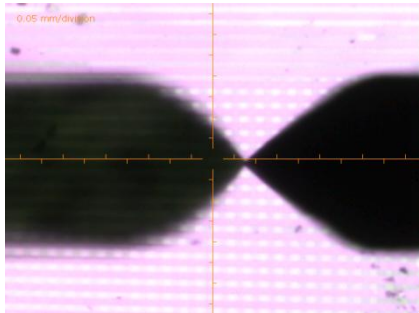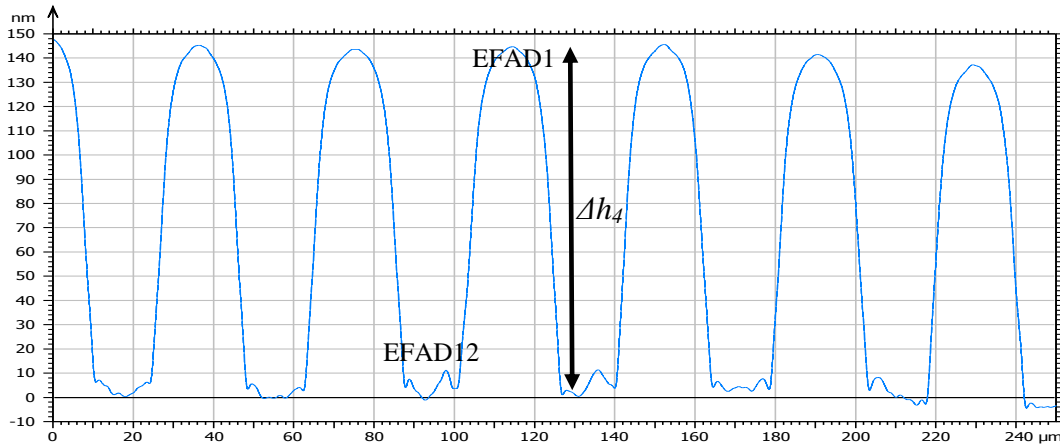
Figure 4. 41. Profiles for direction of microelectrode lines during EFAD1. Top: micrograph of the tip at the microstructure. Profile corresponding to dark-dark line is in middle and to dark-white line at bottom.
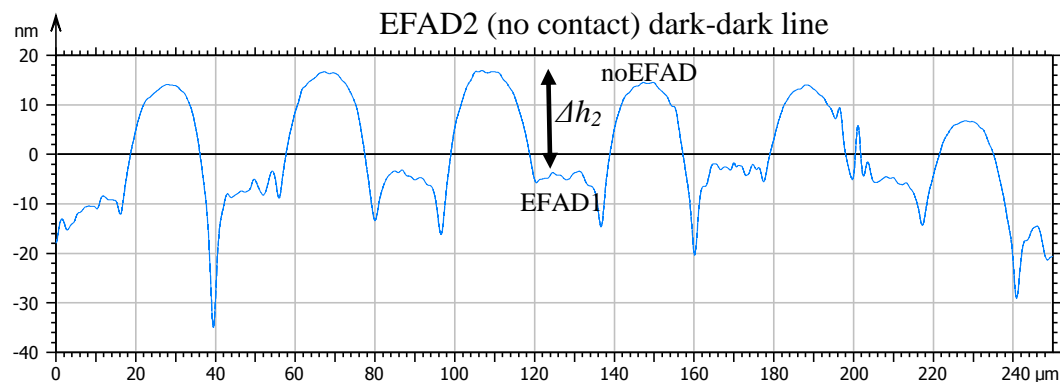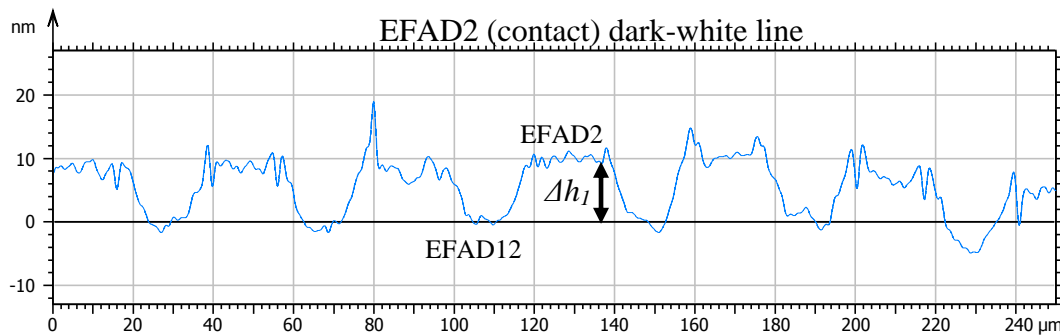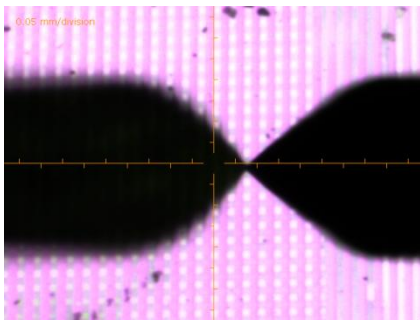
Figure 4. 42 Profiles for direction of microelectrode lines during EFAD2. Top: micrograph of the tip at the microstructure. Profile corresponding to dark-dark line is in middle and to dark-white line at bottom.

Stronger EFAD conditions result in bigger step height. When applied to the treatments to the sample H21, it can be seen that EFAD2 results in higher steps: $\Delta h_3 \approx 115$ nm and $\Delta h_4 \approx 140$ nm, and EFAD1 in lower: $\Delta h_1 \approx 10$ nm, $\Delta h_2 \approx 20$ nm. Based on the samples geometry (*Figure 4. 38*) it is possible to relate steps and dips of the profiles with the treatments (Figure 4. *41* and Figure 4. *42*).

5. CONCLUSIONS

GP serial: In this study it was investigated GP in glasses with different compositions combining several techniques that enabled obtaining novel insights in this process. Depletion zone depths and at% differ in all the samples which results in different $n(d)$. Thus, it is confirmed that $n(d)$ (and polarizability) of different glasses containing alkali and earth alkali ions after poling at the same conditions is influenced by their composition.

Restructuring of silica matrix in the course of GP results in changes of polarizability and refractive index, which can be resolved from analysis of optical measurements, i.e. spectroscopic ellipsometry data. The obtained polarizability profiles of Ca^{2+} and Mg^{2+} free glasses (KF9 and BK7) depleted region are in accordance with SIMS data obtained for Si. These findings support that for the studied samples silica matrix restructuring is not uniform throughout the whole depleted region, but the changes are more pronounced in the region close to the anode surface. In the case of soda-lime glass, Ca^{2+} accumulation masks the contribution of silica matrix densification to the increase of polarizability.

The polarizability profile of KF9, BK7 and SL (Menzel) is consistent with SIMS data. High polarizability near the surface of KF9 and BK7 can be attributed to denser glass matrix due to structural changes of glass matrix from NBO to BO bonds close to surface of glass. The polarizability profiles obtained from ellipsometry derived $n(d)$ corresponds well to modelled contribution of individual atomic species to polarizability obtained by numerical simulations. In this way it was possible to quantitatively correlate the results from optical measurements with those of compositional characterization. Ca^{2+}, Na^+ and Ba^{2+} contribute to the n the most, while K^+ and Mg^{2+} have lower influence.

At% in numerical simulations were normalized to at% calculated from SIMS. The model provided good agreement of simulated and experimental depth profile composition. Numerical simulations resulted in values of previously unknown parameters, such as effective ionic mobilities $\mu(Mg)$ and $\mu(Ba)$ as well as $\mu(H)$ of KF9 glass. In addition, $\mu(K)$ value is two orders of magnitude higher than the one obtained in previous work [126, 127]. The mobilities should be considered as effective mobilities due to the complex interplay of ionic species mobilities in the glass matrix with more than one intrinsic ionic species known as mixed ion effect. Haven ratios (and diffusivities) of ions in studied glasses at applied poling conditions were found to be in the range of experimentally confirmed intervals.

114

The research presented here brings new insights in correlation of compositional and structural changes with optical properties. Better understanding of GP process will help to extend the application of this technique for optical device design and photonics.

Simultaneous EFAD serial: Simultaneous EFAD of Ag/Al bimetal systems has presented gradual dissolution of metal layer that can be controlled with reasonable EFAD conditions, opening possibility for fine tailoring of the systems optical properties. EFAD of Cu/Ag systems suggest that Cu layer is making a kind of barrier for dissolution of Ag. This finding deserves attention and should be studied in some future research.

The influence of thermal annealing and electric field-assisted dissolution on the compositional and optical properties of multilayer structures containing Ag and Au metal island films has been investigated. Annealing of the studied bimetal systems induces optical properties changes due to MIF reshaping, but also to the interaction between metals by ion exchange. EFAD takes place differently for Ag and Au, affecting the evolution of the sample optical properties depending on its structure.

We have determined EFAD conditions that are strong enough for the dissolution of relatively thick Ag MIF (less than 12 min) and yet too weak for considerable dissolution of Au. During annealing, Ag and Na distribute throughout the layers due to ion exchange and Ag accumulates in Au MIF. Na is found in each layer and follows Ag accumulating in Au MIF as well. While Ag and Na are removed from Ag MIF and SiO_2 layers during EFAD, some quantity of Ag remains in Au MIF. Simulations show that the ion exchange happening prior to voltage application facilitates MIF dissolution. They also show that ionic mobility should be higher in dielectric layers than in glass matrix, which is explained by defects in layers that are supporting diffusivity. Results of optical characterization are consistent with SIMS profiles, confirming it can be used for analysis of such complex systems in future research. In summary, the study provides insights that help to understand the potential application of EFAD in systems containing several metals.

Generalization of the ion drift and diffusion equations to an arbitrary number of ionic species has enabled to obtain very good agreement with composition profiles obtained by GP in different types of glass as well as obtain qualitative insights in the relevant parameters that dominate the dissolution process in EFAD experiments of embedded layers. Therefore the developed numerical approach turns out to be a helpful tool to interpret and correlate results from experimental characterization techniques.

Filter serial: It was obtained micro-structured array with 4 colours that human eye can easily distinguish, using 2 EFAD steps with different conditions. Thus is proven that EFAD can be used for this purpose.

The obtained spectra of different areas are not in accordance with the design. However, it was done detailed analysis of the error sources and realistic proposals how to avoid them are given. There are two main reasons why the desired spectra were not realised. The first one is migration of Ag from Ag MIF into TiO_2 layer. This can be avoided simply by replacement of TiO_2 with another high refractive index dielectric layer, such as Nb_2O_5, that is also standard material used for thin films deposition by electron beam evaporation. The second reason is that not all Au was dissolved. This is not necessarily problem, as it is shown that it dissolves so slowly so it would be possible to control its quantity in MIF (and in this way optical properties) by EFAD conditions and use only Au in the ML system. However, in a test sample containing only Au MIF embedded in SiO_2, all Au was successfully dissolved completely with EFAD2 conditions. Due to poor control of low quantity of Au in deposition process, it was deposited more Au in the filter. This problem can be avoided by paying attention to control quantity of Au during evaporation better. There is an opened question if Ag could make dissolution of Au more difficult in simultaneous EFAD of both, that should be a subject of a future work. The blue shift of the main peak, possibly to dielectric layers modification, is not crucial for the performance of the microarray. Also, it does not have to be necessarily a drawback. It just has to be taken into account during design of the filter.

Migration of Ag into Au does not have crucial impact to the filters performance in the visible range, where the filter operates. Much more Ag is lost by migration in TiO_2. The solution would be to deposit a bit higher quantity of Ag in the layer.

Ag in Au MIF is significantly influencing SPR in IR range and is not being dissolved so easily as in pure Ag layer. This finding might be very useful for filters operating in IR range as it allows fine control of optical properties with EFAD, similar like with Au only, as was shown in this research, it is easier to dissolve Ag from Au MIF than Au itself.

Detailed optical characterization based on spectroscopic ellipsometry has been shown to be a valuable non-destructive resource for obtaining insights into the structure and compositional modifications of the samples, such as glass matrix densification upon GP or evolution of LSPR properties during MIF dissolution.

General conclusions

Significant progress is made in understanding relation of reflective index profile of poled glasses with their composition. It is demonstrated that simultaneous EFAD of Ag and Au metal-dielectric systems is a complex process and deserves more attention for the possibilities it offers in tailoring optical properties of such systems. It is demonstrated that it is possible to make microarray filter using EFAD. The origins of the discrepancies to the desired optical properties are analyzed and realistic solutions proposed.

List of figures

120

List of Tables

References

[1] D. Pallarola, A. Bochen, V. Guglielmotti, T. A. Oswald, H. Kessler, J. P. Spatz, *Highly ordered gold nanopatterned indium tin oxide electrodes for simultaneous optical and electrochemical probing cell interactions*, Anal. Chem. **89** 10054–10062 (2017) doi: 10.1021/acs.analchem.7b02743

[2] T. A. Oswald, H. Kessler, J. P. Spatz, Highly ordered gold nanopatterned indium tin oxide electrodes for simultaneous optical and electrochemical probing cell interactions, Anal. Chem. **89** 10054–10062 (2017) doi: 10.1021/acs.analchem.7b02743

[3] V. Janicki, T. V. Amotchkina, J. Sancho-Parramon, H. Zorc, M. K. Trubetskov and A. V. Tikhonravov, *Design and production of bicolour reflecting coatings with Au metal island films*, Opt. Express **19** 25521-25527 (2011) doi: 10.1364/OE.19.025521

[4] V. Janicki, J. Sancho-Parramon, H. Zorc, Gradient silver nanoparticle layers in absorbing coatings—experimental study, Appl. Opt. **50** C228-C231 (2010) doi: 10.1364/AO.50.00C228

[5] Z. Li, S. Butun, K. Aydin, *Large-area, lithography-free super absorbers and color filters at visible frequencies using ultrathin metallic films,* ACS Photonics **2** 183-188 (2015) doi: 10.1021/ph500410u

[6] Z. Liu, X. Liu, S. Huang, P. Pan, J. Chen, G. Liu, G. Gu, *Automatically acquired broadband plasmonic-metamaterial black absorber during the metallic film-formation,* ACS Appl. Matt. Interf. **7** 4962-4968 (2015) doi: 10.1021/acsami.5b00056

[7] P. Mao, C. Liu, F. Song, M. Han, S.A. Maier, S. Zhang, *Manipulating disordered plasmonic systems by external cavity with transition from broadband absorption to reconfigurable reflection,* Nat. Commun. **11** 1538 (2020) doi: 10.1038/s41467-020-15349-y

[8] D. Franklin, Z. He, P. Mastranzo Ortega, A. Safaei, P. Cencillo-Abad, S.T. Wu, D. Chanda, *Self-assembled plasmonics for angle-independent structural color displays with actively addressed black states*, Proc. Natl. Acad. Sci. USA **117** 13350-13358 (2020) doi: 10.1073/pnas.200143511

[9] J. Nath, E. Smith, D. Maukonen, R.E. Peale, *Optical Salisbury screen with design-tunable resonant absorption bands*, J. Appl. Phys. **115** 193103 (2014) doi: 10.1063/1.4876117

[10] S.A. Maier, *Plasmonics: fundamentals and applications*, Springer, New York (2007)

[11] T. Xu, Y.-K. Wu, X. Luo, L. J. Guo, *Plasmonic nanoresonators for high-resolution colour filtering and spectral imaging*, Nat. Commun. 1:59 (2010) doi: 10.1038/ncomms1058

[12] C. G. Wilson, R. A. Dammel, A. Reiser, *Photoresist Materials: A Historical Perspective*, Proc. SPIE **3049** (1997) doi: 10.1117/12.275826

[13] A.A. Lipovskii, V.G. Melehin, M.I. Petrov, Y.P. Svirko, V.V. Zhurikhina, *Bleaching versus poling: Comparison of electric field induced phenomena in glasses and glass-metal nanocomposites,* J. Appl. Phys. **109** 011101 (2011) doi: 10.1063/1.3511746

[14] A. Redkov, S. Chervinskii, A. Baklanov, V. Zhurikhina, A. Lipovskii, *Plasmonic molecules via glass annealing in hydrogen*, Nanoscale Res. Lett. **9** 606 (2014) doi: 10.1186/1556-276X-9-606

[15] T. S. Selvam, I. Fabijanić, J. Sancho-Parramon, P. Pervan, and V. Janicki, *Optical microstructures based on surface-selective growth of Ag nanoparticles on thermally poled soda-lime glass*, Opt. Lett. **47** 1367-1370 (2022) doi: 10.1364/OL.443106

[16] V. Janicki, I. Fabijanić, B. Okorn, P. Dubček, J. Sancho-Parramon, *Selective electric field assisted dissolution as a technique for micro and nano structuring of metal thin films*, Appl. Phys. Lett. **113** 183508 (2018) doi: 10.1063/1.5042037

[17] I. Fabijanić, B. Okorn, P. Dubček, J. Sancho-Parramon, V. Janicki, *A versatile technique for micro and nano structuring of conductive thin metal layers using electric field assisted dissolution,* Mater. Sci. Semicond. Process. **141** 106591 (2022) doi: 10.1016/j.mssp.2022.106591

[18] V. Janicki, J. Sancho-Parramon, F. Peiró, J. Arbiol, *Three-dimensional photonic microstructures produced by electric field assisted dissolution of metal nanoclusters in multilayer stacks*, Appl. Phys B **98** 93-98 (2010) doi: 10.1007/s00340-009-3705-7

[19] B. Okorn, J. Sancho-Parramon, M. Oljača, V. Janicki, *Metal doping of dielectric thin layers by electric field assisted film dissolution*, J. Non-Cryst. Solids **554** 120584 (2021) doi: 10.1016/j.jnoncrysol.2020.120584

[20] B. Okorn, J. Sancho-Parramon, P. Pervan, V. Janicki, "Electric field assisted dissolution of metal films on coated soda-lime glass", J. Non. Cryst. Solids **591** 121715 (2022) 10.1016/j.jnoncrysol.2022.121715

[21] X. Prieto-Blanco, C. Montero-Orille, *Theoretical Modelling of Ion Exchange Processes in Glass: Advances and Challenges*, Appl. Sci. **11** 5070 (2021) doi: 10.3390/app11115070

[22] G. Haas, *Struktur und optik auf gedampfter metall schichten*, Ann.Phys. **31** 245–260 (1938) doi: 10.1002/andp.19384230304

[23] N. Kaiser, *Review of the fundamentals of thin-film growth*, Appl. Opt. **41** 3053–3060 (2002) doi: 10.1364/AO.41.003053

[24] J. W. Evans, Y. Han, B. Unal, M. Lig, K. J. Caspersen, D. Jing, A. R. Layson, C. R. Stoldt, T. Duguet, P. A. Thiel, *From initial to late stages of epitaxial thin film growth: STM analysis and atomistic or Coarse – Grained modeling*, AIP Conf. Proc. **1270** 26-44 doi: 10.1063/1.3476231

[25] P.B. Barna and M. Adamik, *Growth mechanisms of polycrystalline thin films*, Science and Technology of Thin Films, 1–28, (1995) doi: 10.1142/9789814261425_0001

[26] D. E. Aspnes, *Optical properties of thin films*, Thin Solid Films **89** 249-262 (1982) doi: 10.1016/0040-6090(82)90590-9

[27] A. Duparre, *Light scattering of thin dielectric films, in Thin Films for OpticalCoatings*, R. E. Hummel and K. H. Guenther, editors, Handbook of Optical Properties, CRC Press, Boca Raton (1995)

[28] D.M. Mattox, *Handbook of physical vapour deposition (PVD) processing*, William Andrew (2010)

[29] C. Lu, *Mass determination with piezoelectric quartz crystal resonators*, J. Vac. Sci. Technol. **12** 578 (1975) doi: 10.1116/1.568614

[30] S. M. Rossnagel, *Thin film deposition with physical vapour deposition and related technologies*, J. Vac. Sci. Technol. A **21** S74–S87 (2003) doi: 10.1116/1.1600450

[31] J. D. Jackson, *Classical electrodynamics*, Wiley, New York, (1999)

[32] J. A.Woollam, *Guide to Using WVASE: Spectroscopic Ellipsometry Data Acquisition and Anallysis Software*, (2012)

[33] M. Fox, *Optical properties of solids*. Oxford University Press, New York (2001)

[34] J. Jung, J. Bork, T. Holmgaard, and N. A. Kortbek, *Ellipsometry. Detection of nanostructures*, Technical report, Aalborg University, Institute of Physics and Nanotechnology, Aalborg (2004)

[35] G. G. Stokes, *On the composition and resolution of streams of polarized light from different sources*, Transactions of the Cambridge Philosophical Society, Cambridge (1852)

[36] S. N. Savenkov, *Jones and mueller matrices: Structure, symmetry relations and information content*, Light Scattering Reviews **4** 71–119 (2009) doi: 10.1007/978-3-540-74276-0_3

[37] T. Wagner, *Transparent films*, J. A. Woollam Co., (2008)
https://www.utwente.nl/en/tnw/pin/attachments/wagner.pdf

[38] T. Wagner, *Substrates*, J. A. Woollam Co., (2008)
https://www.utwente.nl/en/tnw/pin/attachments/wagner.pdf

[39] E.D. Palik, ed., *Handbook of optical constants of solids*, Academic press (1998)

[40] J. Sancho-Parramon, V. Janicki, H. Zorc, *On the dielectric function tuning of random metal-dielectric nanocomposites for metamaterial applications*, Opt. express **18** 26915-26928 (2010) doi: 10.1364/OE.18.026915

[41] C.F. Bohren and D.R. Huffman, *Absorption and scattering of light by small particles*. John Wiley & Sons (2008)

[42] H. Tompkins, *A user's guide to ellipsometry*, Dover Publications (2006)

[43] F.L. McCrackin, E. Passaglia, R. R. Stromberg, H. L. Steinberg, *Measurement of the thickness and refractive index of very thin films and the optical properties of surfaces by ellipsometry*, J. Res. Nat. Inst. Stand. Technol. **67A** 363–377 (1963) doi: 10.6028/jres.067A.040

[44] R. M. A. Azzam and N. M. Bashara, *Ellipsometry and Polarized Light*, North-Holland, Amsterdam, (1977)

[45] J. Sancho Parramon, *Caracteritzacio optica de materials en estructures multicapa per a filtres interferencials*, PhD dissertation, Universitat de Barcelona (2004)

[46] M. Born and E. Wolf, *Principles of Optics*, Pergamon Press, Oxford (1964)

[47] I. Ohlidal, D. Franta, *Matrix formalism for imperfect thin films,* Acta Phys. Slovaca **50** 489-500 (2000)

[48] A. V. Tikhonravov, M. K. Trubetskov, A. A. Tikhonravov, A. Duparré, *Effects of interface roughness on the spectral properties of thin films and multilayers*, Appl. Opt. **42** 5140-5148 (2003) doi: 10.1364/AO.42.005140

[49] H. Tompkins and E. A. Irene, *Handbook of ellipsometry*, William Andrew, NewYork (2005)

[50] H. Tompkins and J. N. Hilfiker, *Spectroscopic ellipsometry: Practical application to thin film characterization*, Momentum Press (2016)

[51] H. Fujiwara, *Spectroscopic Ellipsometry Principles and Applications*, John Wiley & Sons, Chichester (2007)

[52] D. K. Singh, M. Pradhan, A. Materny, *Modern Techniques of Spectroscopy: Basics, Instrumentation, and Applications*, Springer, Singapore (2021)

[53] G. Parjadis de Lariviere, J. M. Frigerio, J. Rivory, F. Abeles, *Estimate of the degree of inhomogeneity of the refractive index of dielectric films from spectroscopic ellipsometry*, Appl. Opt. **31** 6056-6061 (1992) doi: 10.1364/AO.31.006056

[54] C. K. Carniglia, *Ellipsometric calculations for nonabsorbing thin films with linear refractive index gradients*, J. Opt. Soc. Am. A **7** 848-856 (1990) doi: 10.1364/JOSAA.7.000848

[55] A. V. Tikhonravov, M. K. Trubetskov, A. V. Krasilnikova, *Spectroscopic ellipsometry of slightly inhomogeneous nonabsorbing thin films with arbitrary refractive-index profiles: theoretical study*, Appl. Opt. **37**, 5902-5911 (1998) doi: 10.1364/ao.37.005902

[56] A. V. Tikhonravov, M. K. Trubetskov, A. V. Krasilnikova, E. Masetti, A. Duparre, E. Quesnel, D. Ristau, *Investigation of the surface micro-roughness of fluoride films by spectroscopic ellipsometry*, Thin Solid Films **397** 229-237 (2001) doi: 10.1016/S0040-6090(01)01421-3

[57] A. Macleod, *Optical coatings from design through manufacture*, Thin Film Center Inc., Tucson (2004)

[58] R. R. Willey, *Practical design and production of thin films*, Marcel Dekker, New York, Basel, (2002)

[59] Z. Knittl, *Optics of thin films*, pp. 41-68, John Willey & Sons (1976)

[60] J.E. Shelby, *Introduction to Glass Science and Technology*, The Royal Society of Chemistry, Cambridge (2005)

[61] http://www.jb-electronics.de/downloads/elektronik/nixies/eigenbau/schott_technical_glasses_en.pdf

[62] https://www.schott.com/shop/medias/N-BK7-SDS-EN-V5-201505.pdf?context=bWFzdGVyfHJvb3R8OTQ2MDV8YXBwbGljYXRpb24vcGRmfGhm Ny9oYzEvODgyMzM1Mzc3MDAxNC5wZGZ8YTIxZjdjNzIyOGUyNGI3MzljNmVkZjY4 ZDliY2UzNDMwYTdlMTUxNmZjMWFmZTZiM2M1ZmY0ZmZmZDRmMWYwMw

[63] https://www.schott.com/shop/medias/schott-datasheet-n-bk7-eng.pdf?context=bWFzdGVyfHJvb3R8NjkxODAwfGFwcGxpY2F0aW9uL3BkZnxoZTUva DM4Lzg4MTAzMTYxMDM3MTAucGRmGJjNmI4ZjFmY2Q1NjMxMTE0MjkzMTUwO GRmMTUzOTg2NWJjZTgzMjA0OTc2NTNiMThjN2RhMjI4NGZmMWM4MWU

[64]   https://www.schott.com/shop/medias/N-KF9-SDS-EN-V5-201505.pdf?context=bWFzdGVyfHJvb3R8OTQxMDd8YXBwbGljYXRpb24vcGRmfGhjYS9oNzEvODgyMzM1NDEzMDQ2Mi5wZGZ8ZmRjYjEyYjFkN2MzY2UxMzgyZWNjNjZkZmI1NWE1ZTYzYmY4N2U5Mzg1NGZkMGI1OWVhOGZkNjFhZDgzMmMwNQ

[65]   https://www.schott.com/shop/medias/SCHOTT-datasheet-N-KF9.pdf?context=bWFzdGVyfHJvb3R8NDM2MDI4fGFwcGxpY2F0aW9uL3BkZnxoYjMvaGViLzg4MjI1NjEzNzQyMzgucGRmfGNhNTI4MDc0YTY2NWNhNzI4MDAyNDQxN2JkMWZiMjNlZTI3MWExYThjNzI3Mzcx OTFiODM5MWU4MWM4YzY3MGY

[66] M. Lončarić, J. Sancho-Parramon, M. Pavlović, H. Zorc, P. Dubček, A. Turković, S. Bernstorff, G. Jakopic, A. Haase, *Optical and structural characterization of silver islands films on glass substrates,* Vacuum **84** 188-192 (2009) doi: 10.1016/j.vacuum.2009.04.014

[67] M. Lončarić, J. Sancho-Parramon, H. Zorc, S. Šegota, P. Dubček, S. Bernstorff, S. *Optical and structural characterization of gold island films on glass substrates,* Thin Solid Films **591** 204-209 (2015) doi: 10.1016/j.tsf.2015.04.031

[68] M. Lončarić, J. Sancho-Parramon, H. Zorc, *Optical properties of gold island films—a spectroscopic ellipsometry study,* Thin Solid Films **519** 2946-2950 (2011) doi: 10.1016/j.tsf.2010.12.068

[69] V. Janicki, J. Sancho-Parramon, B. Okorn, H. Zorc, *The influence of annealing on Au films deposited on Ge seed layers,* Proc. SPIE **9547,** Plasmonics: Metallic Nanostructures and Their Optical Properties XIII, 95472M (2015) doi: 10.1117/12.2186776

[70] D. Gérard, S.K. Gray, *Aluminium plasmonics*, J. Phys. D **48** 184001 (2014) doi: 10.1088/0022-3727/48/18/184001

[71] M.W. Knight, N.S. King, L. Liu, H.O. Everitt, P. Nordlander, N.J. Halas, *Aluminum for plasmonics,* ACS Nano **28** 834-40 (2014) doi: /10.1021/nn405495q

[72] J. Martin, J. Plain, *Fabrication of aluminium nanostructures for plasmonics,* J. Phys. **48** 184002 (2014.) doi: 10.1088/0022-3727/48/18/184002

[73] J. Sancho-Parramon, T. Amochkina, S. Wilbrandt, H. Kamble, V. Janicki, K. Salamon, O. Stenzel, M. Trubetskov, *Optical Characterization of Al Island Films: A Round Robin Test*, Coatings **13** 1073 (2023) doi: 10.3390/coatings13061073

[74] T. Ghodselahi, M. Vesaghi, A. Shafiekhani, A. Baghizadeh, M. Lameii, *XPS study of the Cu@Cu2O core-shell nanoparticles*, Appl. Surf. Sci. **255** 2730–2734 (2008) doi: https://doi.org/10.1016/j.apsusc.2008.08.110

[75] G. H. Chan, J. Zhao, E. M. Hicks, G. C. Schatz, R. P. Van Duyne, *Plasmonic properties of copper nanoparticles fabricated by nanosphere lithography*, Nano Lett. **7** 1947–1952 (2007) doi: 10.1021/nl070648a

[76] Q.-C. Sun, Y. Ding, S. M. Goodman, H. H. Funke, P. Nagpal, *Copper plasmonics and catalysis: role of electron–phonon interactions in dephasing localized surface plasmons*, Nanoscale **6** 12450–12457 (2014) doi: 10.1039/C4NR04719B

[77] J. Sancho-Parramon, B. Okorn, K. Salamon, V. Janicki, *Plasmonic resonances in copper island films,* Appl. Surf. Sci. **463** 847-53 (2019) doi: 10.1016/j.apsusc.2018.08.124

[78] K.M. McPeak, S.V. Jayanti, S.J. Kress, S. Meyer, S. Iotti, A. Rossinelli, D.J. Norris, *Plasmonic films can easily be better: rules and recipe,* ACS photonics, **2**.326-333 (2015) doi: 10.1021/ph5004237

[79] D. E. Carlson, K. W. Hang, G. F. Stockdale, *Electrode "Polarization" in Alkali-Containing Glasses*, J. Am Ceram. Soc. **55** 337-341 (1972) doi: https://doi.org/10.1111/j.1151-2916.1972.tb11305.x

[80] I. Fabijanić, P. Pervan, B. Okorn, J. Sancho-Parramon, V. Janicki, *Ellipsometry-based study of glass refractive index depth profiles obtained by applying different poling conditions*, Appl. Opt. **59** A69-A74 (2020) doi: 10.1364/AO.59.000A69

[81] A. V. Redkov, V. G. Melehin, D. V. Raskhodchikov, I. V. Reshetov, D. K. Taganatsev, V. V. Zhurikhina, A. A. Lipovski, *Modifications of poled silicate glass under heat treatment*, J. Non-Cryst. Solids **503–504**, 279–283 (2019) doi: 10.1016/j.jnoncrysol.2018.10.011

[82] C.M. Lepienski, J.A. Giacometti, G.F. Leal Ferreira, F.L. Freire Jr., C.A. Achete, *Electric field distribution and near-surface modifications in soda-lime glass submitted to a dc potential*, J. Non-Cryst. Solids **159** 204-212 (1993) doi: https://doi.org/10.1016/0022-3093(93)90224-L

[83] M. I. Petrov, Y. A. Lepen'kin, A. A. Lipovskii, *Polarization of glass containing fast and slow ions*, J. Appl. Phys. **112** 043101 (2012) doi: 10.1063/1.4742975

[84] A. Dergachev, V. Kaasik, A. Lipovskii, V. Melehin, A. Redkov, I. Reshetov, D. Tagantsev, *Control of soda-lime glass surface crystallization with thermal poling*, J. Non-Cryst. Solids **533** 119899 (2020) doi: 10.1016/j.jnoncrysol.2020.119899

[85] M. Chazot, M. Paraillous, S. Jouannigot, L. Teulé-Gay, J.-P. Salvetat, F. Adamietz, R. Alvarado-Meza, L. Karam, A. Poulon, T. Cardinal, E. Fargin, M. Dussauze, *Enhancement of mechanical properties and chemical durability of Soda-lime silicate glasses treated by DC gas discharges,* J. Am. Ceram. Soc. **104** 157-166 (2020) doi: 10.1111/jace.17438

[86] M. Dussauze, V. Rodriguez, A. Lipovskii, M. Petrov, C. Smith, K. Richardson, T. Cardinal, E. Fargin, E. I. Kamitsos, *How Does Thermal Poling Affect the Structure of Soda-Lime Glass?*, J. Phyis. Chem. C **114** 12754–12759 (2010) doi: 10.1021/jp1033905

[87] A.V. Redkov, V.G. Melehin, A.A. Lipovskii, *How does thermal poling produce interstitial molecular oxygen in silicate glasses?*, J. Phys. Chem. C **119** 17298−17307 (2015) doi: 10.1021/acs.jpcc.5b04513

[88] J. Luo, S. Bae, M. Yuan, E. Schneider, M.T. Lanagan, C.G. Pantano, S.H. Kim, *Chemical structure and mechanical properties of soda lime silica glass surfaces treated by thermal poling in inert and reactive ambient gases,* J. Am. Ceram. Soc. **101** 2951-2964 (2018) doi: 10.1111/jace.15476

[89] I. Reduto, A. Kamenskii, P. Brunkov, V. Zhurikhina, Y. Svirko, A. Lipovskii, *Relief micro- and nanostructures by the reactive ion and chemical etching of poled glasses,* Opt. Mat. Express **9** 3059-3068 (2019) doi: 10.1364/OME.9.003059

131

[90] R. Oven, *Measurement of planar refractive index profiles with rapid variations in glass using interferometry and total variation regularized differentiation,* J. Mod. Opt. **62** S53-S60 (2015) doi: 10.1080/09500340.2015.1083130

[91] E. Babich, D. Raskhodchikov, E. Lubyankina, A. Lipovskii, *Depth of glass poling-via optical transmission spectra,* Optik **244** 167600 (2021) doi: 10.1016/j.ijleo.2021.167600

[92] J. Luo, H. He, N.J. Podraza, L. Qian, C.G. Pantano, S.H. Kim, *Thermal poling of soda-lime silica glass with nonblocking electrodes—part 1: Effects of sodium ion migration and water ingress on glass surface structure,* J. Am. Ceram. Soc. **99** 1221–1230 (2016) doi: 10.1111/jace.14081

[93] R.A. Myers, N. Mukherjee, S.R. Brueck, *Large second-order nonlinearity in poled fused silica,* Opt. Lett.**16** 1732-1734 (1991) doi: 10.1364/OL.16.001732

[94] M. Dussauze, E. Fargin, M. Lahaye, V. Rodriguez, F. Adamietz, *Large second-harmonic generation of thermally poled sodium borophosphate glasses,* Opt. Express **13** 4064-4069 (2005) doi: 10.1364/OPEX.13.004064

[95] P.G. Kazansky, P.S.J. Russell, L. Dong, C.N. Pannell, *Pockels effect in thermally poled silica optical fibres,* Electron. Lett. **31** 62-63 (1995) doi: 10.1049/el:19950036

[96] P.G. Kazansky, L. Dong, P.S.J. Russell, *High second-order nonlinearities in poled silicate fibers,* Opt. Lett.**19** 701-703 (1994) doi: 10.1364/OL.19.000701

[97] A.L.R. Brennand, J. S. Wilkinson, *Planar waveguides in multicomponent glasses fabricated by field-driven differential drift of cations*, Optics letters **27** 906-908 (2002) doi: 10.1364/OL.27.000906

[98] L.A. Fleming, D.M. Goldie, A. Abdolvand, *Imprinting of glass,* Opt. Mat. Express, **5** 1674-1681 (2015) doi: 10.1364/OME.5.001674

[99] L.A. Fleming, S. Wackerow, A.C. Hourd, W.A. Gillespie, G. Seifert, A. Abdolvand, *Diffractive optical element embedded in silver-doped nanocomposite glass*, Opt. Express **20** 22579-22584 (2012) doi: 10.1364/OE.20.022579

[100] A. Lipovskii, V., Zhurikhina, D. Tagantsev, *2D-structuring of glasses via thermal poling: a short review,* Intl. J. Appl. Glass Sci. **9** 24-28 (2018) doi: 10.1111/ijag.12273

[101] G. Yang, M. Dussauze, V. Rodriguez, F. Adamietz, N. Marquestaut, K.L.N. Deepak, D. Grojo, O. Uteza, P. Delaporte, T. Cardinal, E. Fargin, *Large scale micro-structured optical second harmonic generation response imprinted on glass surface by thermal poling,* J. Appl. Phys.**118** 043105 (2015) doi: 10.1063/1.4926866

[102] S.E. Alexandrov, A. A. Lipovskii, A. A. Osipov, I. V. Reduto, D. K. Tagantsev, *Plasma-etching of 2D-poled glasses: A route to dry lithography*, Appl. Phys. Lett. **111** 11 (2017) doi: 10.1063/1.4994082

[103] I. Reduto, A. Kamenskii, A. Redkov, A. Lipovskii, A. *Mechanisms and peculiarities of electric field imprinting in glasses,* J. Electrochem. Soc.**164** E385 (2017) doi: 10.1149/2.0621713jes

[104] E. Cattaruzza, G. Battaglin, F. Gonella, A. Quaranta, G. Mariotto, C. Sada, S. Ali, *Chromium doping of silicate glasses by field-assisted solid-state ion exchange*, J. Non-Cryst. Solids **357** 1846–1850 (2011) doi: 10.1016/j.jnoncrysol.2010.12.050

[105] E. Cattaruzza, F. Gonella, S. Ali, C. Sada, A. Quaranta, *Silver and gold doping of SiO2 glass by solid-state field-assisted diffusion*, J. Non-Cryst. Solids **355** 1136–1139 (2009) doi: 10.1016/j.jnoncrysol.2009.02.012

[106] B. Okorn, I. Fabijanić, J. Sancho-Parramon, F. Zupanič, T. Bončina, V. Janicki, *Surface morphology evolution during electric field assisted dissolution of thin metal films*, Thin Solid Films **685** 402-407 (2019) doi: 10.1016/j.tsf.2019.06.037

[107] M. I. Petrov, V. G. Melehin, V. V. Zhurikhina, Y. P. Svirko, A. A. Lipovskii, *Dissolution of metal nanoparticles in glass under a dc electric field*, J. Phys. D: Appl. Phys. **46** 045302 (2013) doi: 10.1088/0022-3727/46/4/045302

[108] J. Sancho-Parramon, V. Janicki, P. Dubček, M. Karlušić, D. Gracin, M. Jakšić, S. Bernstorff, D. Meljanac, K. Juraić, *Optical and structural properties of silver nanoparticles in glass matrix formed by thermal annealing of field assisted film dissolution*, Opt. Mater. **32** 510–514 (2010) doi: 10.1016/j.optmat.2009.11.004

[109] B. Okorn, J. Sancho-Parramon, P. Pervan, I. Fabijanić, V. Janicki, *Evolution of electric field assisted dissolution of nanoparticles investigated by spectroscopic ellipsometry*, Opt. Mater. **101** 109752 (2020) doi: 10.1016/j.optmat.2020.109752

[110] R.V. Ramaswamy, H. Cheng, R. Srivastava, *Process optimization of buried Ag+–Na+ ion-exchanged waveguides: theory and experiment,* Appl. Opt. **27** 1814-1819 (1988) doi: 10.1364/AO.27.001814

[111] D. G. Ashworth, R. Oven, M. C. Page, *The influence of the pseudo-mixed-alkali effect on the field-assisted diffusion of silver ions into glass for optical waveguides*, J. Phys. D **28** 657 (1995) doi: 1088/0022-3727/28/4/006

[112] E. Cattaruzza, G. Battaglin, F. Gonella, S. Ali, C. Sada, A. Quaranta, *Characterization of silicate glasses doped with gold by solid-state field-assisted ion exchange,* Mat, Sci. Eng. B, **149** 195-199 (2008) doi: 10.1016/j.mseb.2007.11.025

[113] F. Gonella, P. Canton, E. Cattaruzza, A. Quaranta, C. Sada, A. Vomiero, *Field-assisted ion diffusion of transition metals for the synthesis of nanocomposite silicate glasses,* Mat. Sci.and Eng. C, **26** 1087-1091 (2006) doi:10.1016/j.msec.2005.09.019

[114] A. Quaranta, E. Cattaruzza, F. Gonella, G. Peruzzo, M. Giarola, G. Mariotto, *Field-assisted solid state doping of glasses for optical materials,* Opt. Mat. **32** 1352-1355 (2010) doi: 10.1016/j.optmat.2010.04.012

[115] E. Cattaruzza, G. Battaglin, F. Gonella, C. Maurizio, S. Ali, E. Trave, *Doping of silicate glasses with erbium by a field-assisted solid-state ion exchange technique,* J. Phys. D **42** 045301 (2009) doi: 10.1088/0022-3727/42/4/045301

[116] S.S. Gevorgyan, *Single-step buried waveguides in glass by field-assisted copper ion-exchange,* Electron. Lett. **1** 38-39 (1990) doi:10.1049/el:19900025

[117] H. Marquez, D. Salazar, A. Villalobos, G. Paez, J.M. Rincón, *Experimental study of Cu+–Na+ exchanged glass waveguides,* Appl. Opt. **34** 5817-5822 (1995) doi: 10.1364/AO.34.005817

[118] N. Valles-Villarreal, A., Villalobos, H. Marquez, *Stress in copper ion-exchanged glass waveguides,* J. Light. Technol.**17** 606 (1999) doi: 10.1109/50.754790

[119] R. Oven, M. Yin, P.A. Davies, *Characterization of planar optical waveguides formed by copper–sodium, electric field assisted, ion exchange in glass*, J. Phys. D **37** 2207 (2004) doi: 10.1088/0022-3727/37/16/001

[120] A.A. Lipovskii, V.G. Melehin, V.D. Petrikov, *Electric-field-induced bleaching of ion-exchanged glasses containing copper nanoparticles,* Tech. Phys. Lett **32** 275-277 (2006) doi: 10.1134/S1063785006030308

[121] F. Gonella, E. Cattaruzza, A. Quaranta, S. Ali, N. Argiolas, C. Sada, *Diffusion behavior of transition metals in field-assisted ion-exchanged glasses,* Solid State Ion. **177** 3151-3155 (2006) doi: 10.1016/j.ssi.2006.07.047

[122] A. von Hippel, E. P. Gross, J. G. Jelatis, M. Geller, Photocurrent, *Space-Charge Buildup, and Field Emission in Alkali Halide Crystals*, Phys. Rev. J. **91** 568 (1953) doi: 10.1103/PhysRev.91.568

[123] D. E. Carlson, *Ion Depletion of Glass at a Blocking Anode: I, Theory and Experimental Results for Alkali Silicate Glasses*, J.Am. Ceram. Soc. **57**. 291-294 (1974) doi: 10.1111/j.1151-2916.1974.tb10903.x

[124] R. Oven, D.G. Ashworth, M.C. Page, *On the analysis of field-assisted ion diffusion into glass*, J. Phys.: Condens. Matter **4** 4089 (1992) doi:10.1088/0953-8984/4/16/009

[125] M.I. Petrov, A.V. Omelchenko, A.A. Lipovskii, *Electric field and spatial charge formation in glasses and glassy nanocomposites,* J. Appl. Phys. **109** 094108 (2011) doi: 10.1063/1.3582131

[126] R. Oven, *Calculation of the space charge distribution in poled soda-lime glass*, J. Phys. Condens. Matter **34** 055702 (2021) doi: 10.1088/1361-648X/ac3305

[127] R. Oven, *Analytical model of electric field assisted ion diffusion into glass containing two indigenous mobile species, with application to poling*, J.Non-Cryst. Solids **553** 120476 (2021) doi: 10.1016/j.jnoncrysol.2020.12047

[128] X. Prieto, X., J. Liñares, *Increasing resistivity effects in field-assisted ion exchange for planar optical waveguide fabrication,* Opt. Lett. **21** 1363-1365 (1996) doi: 10.1364/ol.21.001363

[129] R. Oven, *Modeling the sequential electric field assisted dissolution into glass of two ion species*, J. Appl. Phys. **101** 113113 (2007) doi: 10.1063/1.2744474

[130] P.C. Zalm, *Secondary ion mass spectrometry*, Surface science techniques, Loughborough University of Technology Loughborough (1994) doi: 10.1016/0042-207X(94)90113-9

[131] P. A. W. van der Heide, *Secondary Ion Mass Specrtoscopy: An Introduction to Principles and Practices,* John Willey and Sons (2014)

[132] V.P. Kaasik, A.A. Lipovskii, D.V. Raskhodchikov, I.V. Reshetov, D.K. Tagantsev, *How to reveal the correct elemental concentration profiles in poled multicomponent silicate glasses from the data of secondary ion mass spectrometry (SIMS),* J. Non-Cryst. Sol. **503** 397-399 (2019) doi: 10.1016/j.jnoncrysol.2018.10.032

[133] N.J. Smith, C.T. McLaren, A.J. Fahey, *Comments on "How to reveal the correct elemental concentration profiles in poled multicomponent silicate glasses from the data of secondary ion mass spectrometry (SIMS)"*, J. Non-Cryst. Sol., **522** 119547 (2019) doi: 10.1016/j.jnoncrysol.2019.119547(2019)

[134] R. Balasubramaniam, R.G.V. Sarepaka and S. Subbiah, *Diamond Turn Machining: Theory and Practice*, CRC Press, Boca Raton (2017)

[135] https://assets.thermofisher.com/TFS-Assets/APD/brochures/objekttraeger_uk_0715_0209.pdf

[136] R.A. Synowicki, *Suppression of backside reflections from transparent substrates*, Phys. Stat. Sol. C **5** 1085–1088 (2008) doi: 10.1002/pssc.200777873

[137] A. B. Lidiard, *Handbuch der Physik*, Springer-Verlag, Berlin (1957)

[138] G.K. Batchelor, *Brownian diffusion of particles with hydrodynamic interaction*, J. Fluid Mech. **74** 1-29 (1976) doi: 10.1017/S0022112076001663

[139] J. V. Fitzgerald, *Transference Numbers for Electrical Conduction in Glass*, J. Chem. Phys. **20** 922-922 (1952) doi: 10.1063/1.1700605

[140] A. D. LeClaire, *Physical Chemistry, Solid State*, Academic Press, New York (1970)

[141] T. Selvam, P. Pervan, J. Sancho-Parramon, M.C. Spadaro, J. Arbiol, V. Janicki, *Glass poling as a substrate surface pre-treatment for in situ metal nanoparticle formation by reduction of metal salt*, Surf. Interf. **33** 102158 (2022) doi: 10.1016/j.surfin.2022.102158

[142] M. Dussauze, T. Cremoux, F. Adamietz, V. Rodriguez, *Thermal Poling of Optical Glasses: Mechanisms and Second-Order Optical Properties*, Int. J. Appl. Glass Sci. **3** 309-320 (2012) doi: 10.1111/ijag.12001

[143]

https://www.corning.com/media/worldwide/csm/documents/HPFS_Product_Brochure_All_Grades_2015_07_21.pdf

[144] https://m.crystran.co.uk/optical-materials/quartz-crystal-sio2

[145] V.V Zhurikhina, M.I. Petrov, K.S. Sokolov, O.V. Shustova, Ion-exchange characteristics of sodium-calcium-silicate glass: Calculation from mode spectra, Tech. Phys. 55 1447-1452 (2010) doi: 10.1134/S1063784210100087

[146] F. Gonella, E. Cattaruzza, A. Quaranta, S. Ali, N. Argiolas, C. Sada, *Diffusion behavior of transition metals in field-assisted ion-exchanged glasses,* Solid State Ion. **177** 3151-3155 (2006) doi: 10.1016/j.ssi.2006.07.047

[147] M.A. Noah, D. Flötotto, Z. Wang, M. Reiner, C. Hugenschmidt, E.J. Mittemeijer, *Interdiffusion in epitaxial, single-crystalline Au/Ag thin films studied by Auger electron spectroscopy sputter-depth profiling and positron annihilation*, Acta Mater. **107** 133-143 (2016) doi: 10.1016/j.actamat.2016.01.061

[148] S.K. Ghosh, T. Pal, *Interparticle coupling effect on the surface plasmon resonance of gold nanoparticles: from theory to applications,* Chem. Rev. **107** 4797-4862 (2007) doi: 10.1021/cr0680282

[149] M. Hövel, B. Gompf, M. Dressel, *Dielectric properties of ultrathin metal films around the percolation threshold,* Phys. Rev. B **81** 035402 (2010) doi: 10.1103/PhysRevB.81.035402

[150] A.J. de Vries, E.S. Kooij, H. Wormeester, A.A. Mewe, B. Poelsema, *Ellipsometric study of percolation in electroless deposited silver films,* J. Appl. Phys **101** 053703 (2007) doi: 10.1063/1.2654234

[151] R. Sarmiento-Perez, T.F. Cerqueira, I. Valencia-Jaime, M. Amsler, S. Goedecker, S., Botti, M.A. Marques, A.H. Romero, *Sodium–gold binaries: novel structures for ionic compounds from an ab-initio structural search,* New J. Phys. **15** 115007 (2013) doi: 10.1088/1367-2630/15/11/115007

[152] M. Bubaš, I. Fabijanić, A. Kenđel, S. Miljanić, M.C. Spadaro, J. Arbiol, V. Janicki, J. Sancho-Parramon, *Unifying stability and plasmonic properties in hybrid nanoislands: Au-Ag synergistic effects and application in SERS,* Sens. Actuators B Chem. **380** 133326 (2023) doi: https://doi.org/10.1016/j.snb.2023.133326

[153] Z. Zou, Q. Wang, X. Chen, S. Qu, *Direct evidence for electric field assisted dissolution of Au nanoparticles on glass surface,* J. Appl. Phys. **105** 103114 (2009) doi: 10.1063/1.3133240

[154] M. Leitner, H. Peterlik, B. Sepiol, H. Graener, M. Beleites, G. Seifert, Uniformly oriented, ellipsoidal nanovoids in glass created by electric-field-assisted dissolution of metallic nanoparticles, Phys. Rev. B 79 153408 (2009) doi: 10.1103/PhysRevB.79.153408

[155] P. Pervan, J. Sancho-Parramon, B. Okorn, V. Janicki, *Modelling of concentration profiles in thermally poled glasses and correlation with refractive index profiles,* J. Non-Cryst. Sol **608** 122232 (2023) doi: 10.1016/j.jnoncrysol.2023.122232

[156] J. Sancho-Parramon, V. Janicki, J. Arbiol, H. Zorc, F. Peiro, *Electric field assisted dissolution of metal clusters in metal island films for photonic heterostructures,* Appl. Phys. Lett. **92**, 163108 (2008) doi: 10.1063/1.2892037